Application of charge-coupled devices for astronomical spectroscopy

Zainuddin, Mohd Zambri

APPLICATION OF CHARGE-COUPLED DEVICES FOR ASTRONOMICAL SPECTROSCOPY

by

MOHD ZAMBRI ZAINUDDIN

(B.Sc. University of Malaya)

A Thesis submitted for the Degree of Doctor of Philosophy in the Department of Physics, University of Durham

June 1983

This thesis is dedicated to my mother, uncle,

wife and son.

ABSTRACT

It has been found, using a charge coupled device detector and a novel on chip pre-binning technique, that qualitative high dispersion spectroscopy is possible with a small telescope and poor seeing. Using the 30 inch Coude telescope at the Royal Greenwich Observatory, an atlas of an M3 giant, HR 5490 has been obtained in a new region of the spectrum i.e. λ 9748Å - λ10153Å. However, more work is needed on the identification of the lines in order to verify this work and to extend the atlas. The readout noise of the charge coupled device camera system was found experimentally during the early stages of system development to be at most 55 electrons. Later work suggests the true figure to be closer to half this and although this is probably still greater than optimum for the device, the charge coupled device camera system has, nonetheless, demonstrated great potential as a detector for astronomical spectroscopic work particularly in the red and near infrared.

ACKNOWLEDGEMENTS

Firstly, I would like to express my gratitude to the University of Malaya for their sponsorship and to the Government of Malaysia for awarding a scholarship to make this work possible. I am also deeply indebted to my supervisor, Dr. J.M. Breare, for his invaluable guidance, encouragement and constant willingness to help in every possible way throughout the project. Equally, sincere thanks are due to my many colleagues for their various contributions and continued mental stimulation, in particular I would like to thank Mr. N.R. Waltham, Mr. G.P. Martin, Mr. R. King, and Mr. I. Parry.

Professors A.W. Wolfendale and B.H. Bransden are warmly thanked for their continued support and interest in this work and for allowing the use of the many technical resources and skills available within the Department of Physics at Durham University. Special thanks are reserved for Mr. J. Webster for his highly skilled technical assistance in almost every aspect of the project.

Additionally, I am indebted to the Director of the R.G.O., Professor A. Boksenberg and members of the staff of that institution for their help and guidance with the observational part of this work. I am very grateful to Dr. D.L. Harmer for her assistance in using the 30 inch Coude Telescope at the R.G.O. and for many useful discussions on the astronomical programme. Drs. S.P. Worswick (R.G.O.) and R.S. Clegg (U.C.L.) are also acknowledged for many useful discussions on the astronomical programme.

Concerning the production of this thesis, I would like to thank Mrs. Margaret Chipchase for her excellent typing, Mr. N.F. Thompson (Department of Applied Physics and Electronics) for drawing the diagrams and Dr. A.W. Campbell for his useful comments and help with the text.

Last, but not least, I am grateful to my wife, Noorul-Aini Ambak without whose patience and constant encouragement my part in this work could not have been possible.

CONTENTS

Page No.

CHAPTER 1

REVIEW OF THE PROPERTIES OF SOLID STATE DETECTOR AND ASTRONOMICAL CONSIDERATIONS

1. INTRODUCTION

Astronomical light detectors have the important job of converting the stellar photons into a recordable signal. To date there are a wide variety of light detectors available for astronomy, including photographic emulsions, photocathodes (e.g. electronography (1), image intensifiers (2), image photon counting system (3), etc.), integrating television camera tube (4), and solid state imaging devices. Among the above mentioned detectors, the solid state imaging devices are the most recently introduced for astronomical imaging and spectroscopic work. In recent years, most solid state imaging devices available for astronomy have been electronically scanned silicon devices such as photodiodes arrays e.g. Reticon (5), charge injection devices (6) and charge-coupled devices (7). The latter being the newest and most promising type of solid state imager to be employed for astronomical purposes.

Almost all the photometry of starlight done through the visible atmospheric window in the past has involved the photographic plate, or the photomultiplier tube. Since most solid state imaging devices are based on silicon as the photon detecting medium, they are particularly efficient in the red and near infra-red region of the electromagnetic spectrum, a region of interest where photographic plates are not at their most useful. In order to reveal the potential of charge coupled devices (CCDS) as an astronomical detector particularly suited to spectroscopic applications, a decision was taken to attempt to build a CCD camera system which would

allow the use of the array, under direct illumination, for looking at stellar spectra around the one-micron region. The development and construction of the CCD camera system will be described in chapters three and four of this thesis.

This chapter will begin with a qualitative description of photosensitive detector characteristics for astronomical applications, followed by discussions of the primary parameters (i.e. the noise equivalent power and detectivity, dark output, linearity, spectral response, etc.) of charge coupled devices favourable for astronomical applications as compared to the photographic plate. The operation and performance limits of the CCD as an astronomical detector are deferred to chapter two.

To show the capability of the CCD as an astronomical instrument, a program of compiling a spectral atlas of one bright, M3, giant star in the wavelength interval λ9748Å to λ10153Å with a CCD system has been conducted at the 30 inch reflector telescope, at the Royal Greenwich Observatory. The wavelength interval is chosen because there are very few atlases of stellar spectra at one-micron region made available for astronomy. This is probably due to lack of photosensitive detectors operating effectively in the one-micron region. A review of stellar spectra in the one-micron region obtained with various photodetectors available until the current date will be presented in this chapter. From this review, it is hoped that the idea of compilation of the spectral atlas of one bright M3 giant in the wavelength range λ9748Å - λ10153Å with the CCD shows its promise for astronomical spectroscopy applications and the results achieved may help to solve some of the problems found at wavelengths around one-micron in the past.

1.1 Photosensitive Detectors for Astronomical Imaging and Spectroscopy

It is universally known that light is the most familiar form of electromagnetic radiation. Electromagnetic radiation can appear itself as both waves and particles, or as either, and thus has a dual nature. So, light can be considered as streams of particles travelling at the speed of light c, and having zero mass; the particles are tiny packets of energy called photons. The energy of the photons is related to the frequency, ν of the radiation by Planck's constant h, as given by the equation

$$E_{ph} = h\nu \qquad (1.1)$$

The range of frequencies or wavelengths of electromagnetic radiation is known as the electromagnetic spectrum (Figure 1.1). The electromagnetic spectrum can be divided into various regions as depicted in the figure given. The characteristics of radiation from various regions of the electromagnetic spectrum may be investigated through using the appropriate photosensitive detectors for astronomical imaging and spectroscopy applications. As mentioned earlier, there are a wide variety of light detectors available for astronomy which cover various regions of the electromagnetic spectrum, however, the present discussion will confine itself to those applicable to the red and near infra-red region.

There are two broad classes of detectors being employed for infra-red observations; coherent and incoherent. Coherent detectors are those that preserve frequency and phase information during the recording process (e.g. photo-

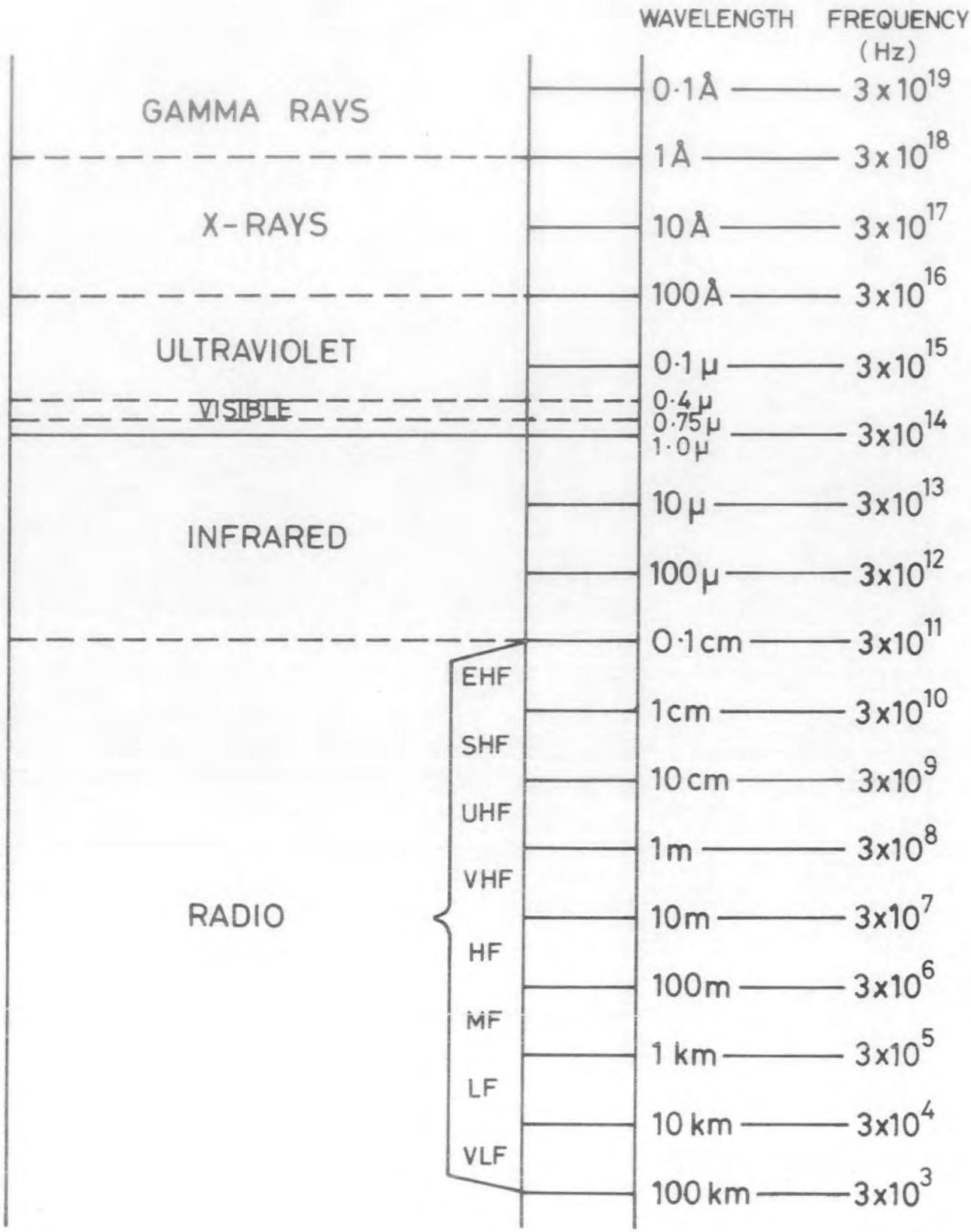

FIG. 1·1 ELECTROMAGNETIC SPECTRUM

graphic plate), whereas incoherent detectors are those in which a voltage or current is produced in direct proportion to the amount of incident electromagnetic radiation flux (e.g. charge-coupled device). The incoherent detectors can be divided into two main categories; thermal detectors and quantum detectors. In a thermal detector, the electromagnetic radiation is absorbed on a nearly black surface which in turn converts the radiation effectively into heat. This heat will cause a change in temperature of the crystals used in the detector (e.g. a cryogenic gallium-doped germanium bolometer (8)). This change in temperature of the crystal of germanium with added gallium impurity is measured by a change in resistance, which in turn causes a change in the voltage dropped across the devices under conditions of constant current bias. Quantum detectors are also known as photon detectors. There are two kinds of devices employed as photon detectors; the photoconductive devices and the photovoltaic devices. In photoconductive devices, the photons are absorbed in the crystal and excite electrons and holes to the conduction band, changing the electrical conductivity of the crystal. One example of such a device is lead sulphide, PbS. In a photovoltaic device, a large area p-n junction is first created which is then illuminated with radiation, electrons and holes are generated and subsequently separated by the junction. Finally, the electrons or holes are then detected as a photocurrent or photovoltage at the output of the detector which is proportional to the incident radiation. One important property of the photodetectors is that their response is not uniform at all wavelengths but a

threshold energy exists, determined by the semiconductor energy gap between bound and free carriers. Thus, only those incident photons with energy greater than Eg are detected. Such a property will enable longer wavelength measurements through the production of extrinsic photoconductive devices. These are devices where a carefully controlled amount of impurity has been added, such that a much smaller threshold energy exists and hence gives long wavelength response. Since the CCD is a member of the photodetector group which recently became available much interest has been shown in using this device as an astronomical detector.

1.2 Charge Coupled Device as a Photon Detector

CCDs are mainly fabricated from silicon as the photon detecting medium, and thus have a useful response from 0.4 micron up to 1.1 micron with peak sensitivity in the very near infra-red i.e. at approximately 0.8 micron. A single photon, if absorbed in the silicon, may cause two types of electronic transitions: intrinsic excitation, and extrinsic excitation or impurity excitation as depicted in Figures 1.2 a, b, and c. In Figure 1.2a, the incident photons excite electrons from the valence band of a semiconductor into the conduction band, thereby creating a free hole and a free electron, whereas in Figure 1.2b and c, the incident photon ionize impurity centers producing either a free hole and a bound electron (p-type) or a free electron and a bound hole (n-type). In both cases, the minimum photon energy necessary for absorption in this manner is determined by the energy-gap, so that a photon detector will have a long wavelength cutoff at, λ_{cutoff},

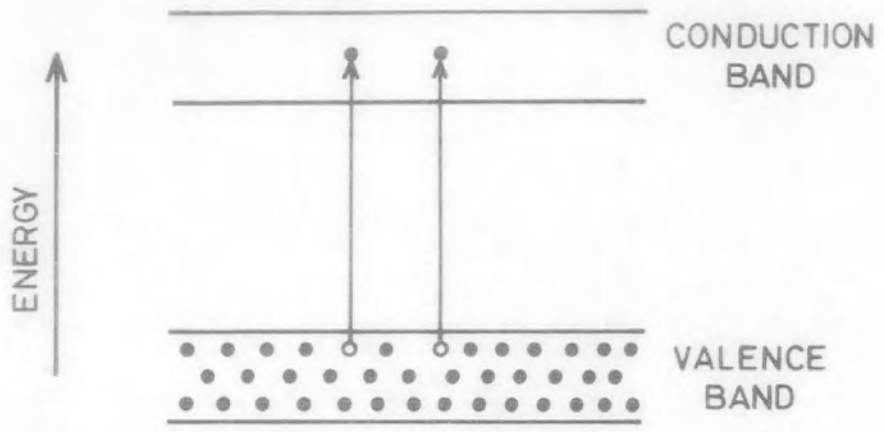

(a) INTRINSIC SEMICONDUCTOR

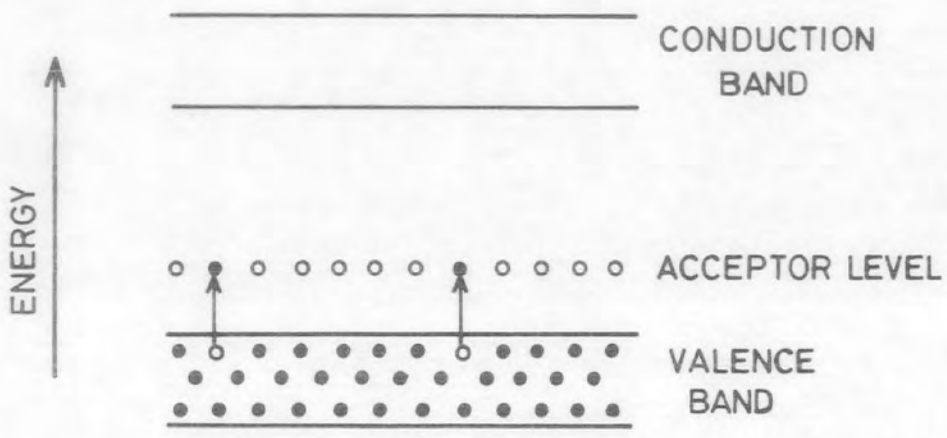

(b) EXTRINSIC SEMICONDUCTOR (P-TYPE)

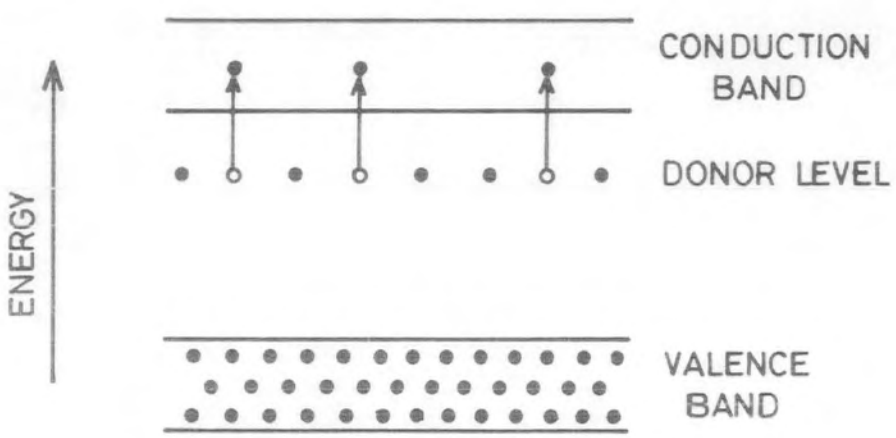

(c) EXTRINSIC SEMICONDUCTOR (N-TYPE)

FIG. 1·2

$$\lambda_{cut\,off} = \frac{hc}{E_g} \qquad (1.2)$$

where h is the Planck constant;

c is the velocity of light, and

E_g is the band gap energy of the semiconductor.

For silicon, at a temperature of 42K, if band-gap energy E_g = 1.166eV, thus the cutoff wavelength is about 1.07μm as derived from equation 1.2. However, in silicon, a slight complication occurs because it is an indirect band gap material, whereby transitions involving photons of lower energy just across the band-gap often require the additional interaction of a phonon in order to conserve momentum (see Figure 1.3). This type of indirect transition occurs with lower probability than direct transitions and leads to blurring of the relatively sharp absorption edge associated with direct band gap materials (10).

In photographic plates, the photons are absorbed by the silver halide crystals, resulting in a photochemical change in the crystals. Details of the theory of this process can be seen in publications of James (11), Engel (12), etc. The photographic plate is then processed with a chemical solution called developer, the photoactivated crystals, i.e. the silver halide crystals which absorbed photons are reduced to metallic silver much more rapidly than the unexposed crystals. During the developing time, a large fraction of the crystals which absorbed photons are reduced but only a small fraction of the unexposed crystals are reduced. These unused silver halide crystals are removed from the plate through successively

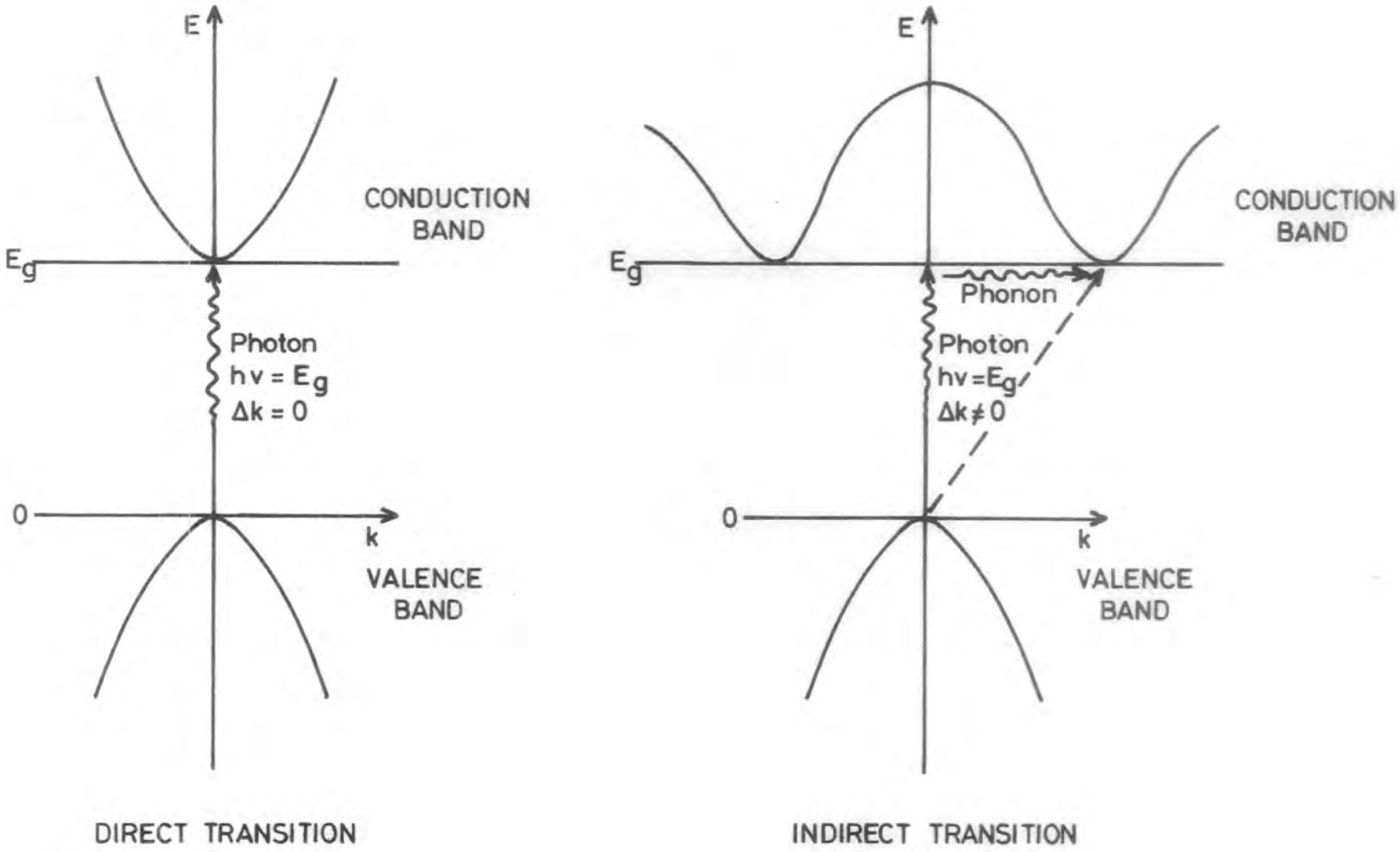
E
CONDUCTION BAND
E_g
Photon
$h\nu = E_g$
$\Delta k = 0$
0
k
VALENCE BAND
DIRECT TRANSITION
E
CONDUCTION BAND
E_g
Phonon
Photon
$h\nu = E_g$
$\Delta k \neq 0$
0
k
VALENCE BAND
INDIRECT TRANSITION

FIG. 1·3

immersing the plate in other solutions during the developing time. Finally, a negative image is produced comprising the precipitated silver crystals which are black because of their light absorption properties. Quantitative measurements and reductions are made from the photograph by means of a microdensitometer. A description of this machine can be found in Latham (13).

The main difference here between the CCD and photographic plate is that immediate observational data assessment and processing can be made on-line at the telescope with the CCD, which is not possible with photographic plates. Such an advantage is very useful because of the limited time allocated at telescopes.

1.3 The Concept of Detectivity (D)

An ideal photon detector would enable every bit of the incident photon information to be collected and recorded. In practice actual detectors will always fall short of doing so mainly due to the geometric and physical properties of the detectors which cause deviations from the ideal case. However, since the arrival of photons at the surface of a detector is characterized by both spatial and temporal noise (14) therefore an actual detector will always have a noise level higher than that inherent in the arriving stream of photons. Thus, a concept which is often used for astronomical applications in describing the performance of the detector is the noise-equivalent power (NEP). The NEP is defined as a measure of the minimum detectable signal capability of the detector i.e. the incident power required to provide a root-mean-square (r.m.s.) voltage output equal to the r.m.s. noise voltage, i.e. giving a signal-to-noise ratio of unity.

The NEP is the most relevant parameter for comparison among detectors applicable to astronomy.

The NEP is said to be proportional to the square root of the electrical bandwidth Δf, and in most cases it is also proportional to the square root of the detector area, thus a new figure of merit is defined and known as detectivity D^* (15). The detectivity is represented by the equation given below

$$D^* = \frac{(A_s \Delta f)^{1/2}}{NEP} \qquad (1.3)$$

where A_s is the area of the sensor, and Δf is the post-detection electrical bandwidth.

From this equation, it can be seen that the larger the value of D^*, the more sensitive the detector.

1.4 The Dark Output

Dark output is the detector output generated in the absence of illumination. This dark output must be known for two reasons: firstly, it is only the detector output above the average dark level that corresponds to the light being measured and; secondly, the dark component contributes noise. The dark noise in the CCD will be considered in the next chapter. CCDs show a dark signal arising from thermal or leakage currents. At room temperature, the thermal or leakage currents dominate the output of the CCD, making it unusable for low light level imaging. Refrigeration of the CCD has consequently proved very effective in reducing the dark output. There are many methods of refrigerating the CCD, but the general method of cooling is by thermal contact in a liquid

nitrogen cryostat. Integration of several hours can then be achieved with only a minor dark current contribution to the collected signal. However, there are two possible side effects of cooling the CCD; (i) the formation of condensation or even frost on the CCD or window of the cryostat; and (ii) reduced quantum efficiency at longer wavelengths (will be described in chapter 3). Resistive heaters may be placed around the window of the cryostat to prevent the condensation.

In photographic plates, the dark output is the background "fog". The background fog arises from thermal excitation of the silver halides in the emulsion, cosmic rays and radioactive trace elements in the vicinity of the plate. For this reason, the spectroscopic plates are kept refrigerated before being used. Hence, the total fog that appears during development of the used plate depends on the emulsion type, the developing procedures, the type of developer and the past history of the plate. If the fog is not uniform over the plate, then it leads to error in measurement.

1.5 The Detector Linearity

When the output of a detector is proportional to the amount of incident photon flux, the detector is said to exhibit linearity. The potential sources of non-linearities in CCD for imaging and spectroscopy applications are described in this section. There are three possible sources of non-linearities present in the CCD; (i) the charge transfer process, (ii) optical charge injection, and (iii) charge detection.

During the charge transfer process, some of the collected signal may be trapped and left behind in the potential well which leads to a transfer loss proportional to the signal charge, Q_s. This effect is known as charge transfer inefficiency and will introduce only linear distortions. The non-linearities introduced during the transfer of the signal charge are thus normally neglected when compared to those introduced by (ii) and (iii) above.

In optical charge injection processes, ideally every photon absorbed in the silicon bulk will generate a minority carrier, which is then collected in the nearest potential well. If the same fixed fraction of carriers is always collected the device will show perfect linearity up to the limit given by the saturation of the well. In a practical device this fraction may change, since the depletion areas surrounding the integration site decreases as the potential well fills up. In most devices however, the deviation from linearity is very small as demonstrated by White et al. (16).

During charge detection operation the primary source of signal distortion is the detection node itself (i.e. the output diode). A non-linear term arises from the changing depletion capacitance around the sensing diode or around the potential well in which the signal charge is to be detected. The influence of the depletion capacitance can be reduced by using a high resistivity substrate material (17), thus keeping the sensing diode small and loading the sense node with a fixed capacitance that dominates the depletion term. Nowadays most of the CCDs manufactured for astronomical applications have a linear overall transfer function, i.e. the residual non-

linearities in the input and output circuit of the device are matched.

In the photographic process, the "linearity" depends on exposure time, treatment during development, the wavelength and the emulsion type. Deviations from linearity may be more pronounced for under-exposed and over-exposed conditions. If the plate is not properly developed, (i.e. results from under and over development of low and high density sides respectively of a sharp density gradient) the so-called adjacency effects (18), will occur thus causing non-linear behaviour. The reciprocity failure of the emulsion will also cause a deviation from linearity. This is a process where the memory of the emulsion fades during long exposures to faint light, causing the developed image to be weaker than if the same number of photons had been impressed upon the plate in a shorter time. Shining on the emulsion with lights of unequal brightness does not produce the same density image as a uniform constant exposure of the same total number of photons, such effects are called the intermittency and clayden effects (19). The importance of these problems arises from 'seeing' and scintillation which cause a strong modulation in the amount of light reaching the emulsion. Finally, it can be summed up that the photographic process shows only an approximately linear behaviour over a limited density range. As a consequence, it is necessary to calibrate each and every recorded spectrogram to be used for qualitative measurements.

1.6 Quantum efficiency and Spectral Response

The quantum efficiency is defined as

$$\eta(\lambda) \equiv \frac{\text{number of detected photons}}{\text{number of incident photons}} \qquad (1.4)$$

i.e. the probability of a photon causing a recordable event. For low light level imaging, it is very important to have η as large as possible. In photographic plate, the rate of darkening on the plate is directly proportional to η . Similarly for photodetectors, the size of its output (i.e. the signal at the output) is directly proportional to η . Detailed description of the quantum efficiency of the CCD will be given in Chapter 2.

The spectral response is expressed as the change in sensitivity of a detector with wavelength, i.e. it is an inherent property of the material from which the detector is constructed. Generally, specifying quantum efficiency is one way of describing the spectral response but there are other qualities often used by the manufacturer to define the spectral response of a detector. For example, in photographic plate, the "exposure" is defined as the product of the level of illumination times the exposure time. It is proportional to the total number of photons incident upon a unit area of the plate, thus the spectral response of the photograph is the reciprocal of the exposure needed to give a specified level of darkening on the plate. For photographic plates, different spectral response over the full visible window may be achieved by introducing various dyes into the emulsion (details may be found in Brooker (20)). The maximum quantum efficiency of photographic plates is usually between

0.1 and 1.0 percent depending on the emulsion type and treatment of the plate, although values as high as 4 per cent have been reported by Millikan (21). One reason the quantum efficiency of photographic plates is so low is because a substantial fraction of the incident photons are reflected and scattered by the emulsion rather than being absorbed. Furthermore, as suggested by Webb (22), as many as 10 photons may be required per grain to make it darker during development.

In photodetectors, if the radiation incident on the detector has a strength of W watts and consists of N photons/sec, then

$$W = \frac{Nhc}{\lambda} \qquad (1.5)$$

and the photocurrent due to these photons is given by

$$i_p = \eta(\lambda) Nq \qquad (1.6)$$

where q is the electronic charge. Dividing equations (1.6) with (1.5) and rearranging gives

$$i_p = \frac{\eta(\lambda) W\lambda q}{hc} \qquad (1.7)$$

Thus equation (1.7) may represent the spectral response of the photodetector. The maximum quantum efficiency of most photodetectors usually occur in the blue and are in the range of 10 - 60 percent. However, there are photodetectors having quantum efficiency of 10 - 30 percent in the red and near infra-red region which have been manufactured recently. An example is the General Electric Company charge-coupled device. Detailed description of this device and its performance will

be given in the next chapter.

1.7 Aspects of Telescopes

For useful astronomical observations the detector must be coupled to a telescope. The main function of a telescope for studies of stellar photosphere is to collect light for spectral analysis. Several types of telescope systems may be employed for observation at various regions of the electromagnetic spectrum. In this section, some aspects of telescopes with coude focus systems and the fundamental problems in astronomical observations will be described briefly.

The size and design of a telescope must be compatible with the spectroscopic equipment, i.e. the spectrograph or interferometer coupled to it. For example, the focal ratio of the telescope, must match the focal ratio of the collimator in the spectrograph or interferometer to avoid light loss. The light increasing power of the telescope is proportional to the square of the aperture size only if the whole of the stellar seeing disc is admitted into the entrance aperture of the analyzing equipment, but for a slit spectrograph the telescope's light increasing power varies linearly with aperture. The reason for this can be described as follows: the linear diameter of the seeing disc is proportional to the effective focal length of the telescope which in turn increases linearly with the aperture because the f-ratio must stay fixed to match the spectrograph. Thus the linear size of the seeing disc increases in both dimensions; across the entrance slit, and along the entrance slit, in proportion to the aperture. The increased dimension across the slit accomplishes nothing since the light is stopped by the slit jaws. The increase along

the slit lets more light through in proportion to the increase in length. To collect most of the light coming through the slit, the CCD is read out using an on-chip pre-binning technique. This readout mode will be described in chapter five.

So far, the contribution of background noise mainly from detector noise and sky background, which impose a limitation to the starlight signal detected, has not been discussed and they are deferred to chapters 2 and 5 respectively.

1.8 Astronomical Measurements in The Infrared for Stars

During recent years there have been rapid developments in astronomy, with particular emphasis upon astronomical measurements in the infrared . To a great extent, this increased emphasis has been stimulated by recent progress in the development of photosensitive detectors, which are capable of making these difficult long-wavelength observations. Furthermore, in recent years the application of electronic data processing and computer techniques to the 'modern' detector systems (e.g. solid state imaging devices) has made it possible for data processing and recording technique to be applied on-line while at the telescope.

There are many reasons for observing stellar spectra in the infrared, (e.g. as pointed out by Spinrad (24)) infrared spectra provide information about the abundances of relatively light elements and some molecules. The atoms such as neutral helium, carbon, and sulphur have their strongest accessible transitions in the infrared and molecules such as H_2, CO and H_2O can be observed only in the infrared.

Moreover, there are spectral intervals in which the continuum is clearly defined even in very cool stars, so that equivalent widths of atomic lines can be measured and they are useful for evaluating the infrared opacity, which must be known for the construction of realistic model atmosphere of late-type stars (25). Many molecules never before observed in an astrophysical source may become available for study through their infrared rotation - vibration bands (26). Some stars, by virtue of low temperature, interstellar reddening, or circumstellar emission are actually easier to observe in the infrared than at shorter wavelengths. Finally a good deal of purely exploratory work remains to be done, whose results inevitably will add to the importance of infrared spectroscopy. This review will endeavour to incorporate the papers that report new observations of stellar spectra specifically in the one-micron region.

1.9 Atmospheric Transmission Effects

Ground-based infrared observations are limited almost entirely to several transmission "windows" in the near infrared region of the spectrum because of atmospheric absorption. The transmission of infrared radiation from the source (e.g. star) to the image plane (i.e. detector at ground based telescope) is greatly dependent upon the transmission characteristics of the earth's atmosphere which modify the spectrum arriving at the sensor. The attenuation of the infrared radiation is due primarily to molecular absorption bands in carbon dioxide and water, with additional minor contributions due to a number of other constituents, such as methane, carbon monoxide, nitrous oxide and ozone. It is

really fortunate that the two major constituents of the atmosphere, nitrogen and oxygen are homonuclear molecules, thus exhibiting no molecular absorption bands because they possess neither a permanent nor an induced dipole moment (26).
The windows available for ground based infrared observation are illustrated in Figure 1.4, withthe absorbing molecules indicated

The concentration of atmospheric absorbers varies significantly from site to site (i.e. altitudes of observation) and also with time (particularly true of water vapour). Therefore, it is important to choose a transmission "window" which is free from water vapour bands for observation or else the spectrum obtained will be blended with telluric water lines which are difficult to remove.

Infrared observations are not only affected by the absorption of the atmospheric constituents but also by deflection and scattering processes which occur during transmission. Scattering and deflection by particles in the air path may cause blurring of the image (i.e. "seeing") and thus limit the minimum usable field of view. Moreover, particles and gases themselves can be sources of radiation, including the earth's atmosphere itself. Thus, the ultimate lower limit to the background noise for an observation is determined by the earth emissivity. An additional source of noise is rapid fluctuations in atmosphere temperature and density, e.g. turbulence; this source is known as "sky noise" and is highly variable. These are the reasons why it is preferable to make some infrared observations from aircraft, high-altitude balloons, rockets or spacecraft.

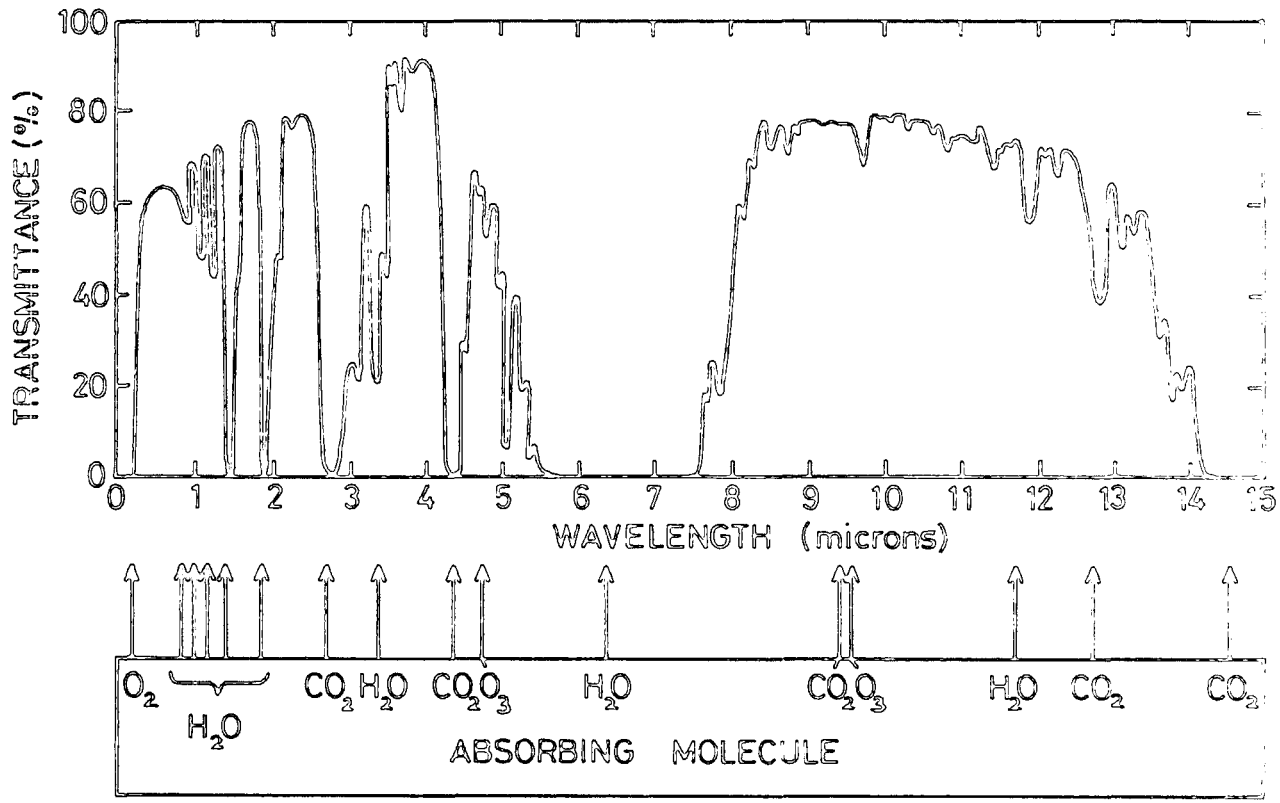

FIG. 1·4 ATMOSPHERIC TRANSMISSION

1.10 Atlases of The One-Micron Region

The infrared spectrum may be divided into the following four regions; the near infrared (0.7 - 0.9μ); the one-micron region (0.9 - 1.1μ); the two-micron region (1.2 - 2.5μ); and the far infrared covering the range of wavelengths from about 3μ to millimeters and the domain of radio astronomy. A detailed review of early developments in the infrared spectroscopy of stars was first published by Spinrad and Wing (1969) (27), followed by the most recent review given by Merrill and Ridgway (1979) (28). Since our interest lies in the one-micron region of the infrared spectrum, a brief review covering the observations of stellar spectra at one-micron and their importance will be described,

Five methods of observation (according to Spinrad and Wing (1969)) have been used to study the one-micron spectral region: (i) conventional slit spectrograms on the Z and M emulsions; (ii) objective prism spectrograms on the Z plates; (iii) image tube spectrograms using an S1 photocathode; (iv) photoelectric spectral scans; and (v) high resolution interferometric observations. Of these observational methods the Z emulsions and the image tube spectrograms using an S1 photocathode have often been used to record one-micron region stellar spectra in the past. The first stellar spectra recorded on the Z emulsion plates at the one-micron region were taken in 1945 by Sanford (29), with the Mount Wilson Coude Spectrograph and a dispersion of 20Å/mm. Sanford's high dispersion stellar spectra of α Ori and other stars between λ10000Å to λ 10915Å revealed almost nothing that could not have been predicted from solar and laboratory data

already available, and this may be the reason why no further work in the one-micron region was done for several years. Observations of many relatively faint stars at low dispersions were made possible with the improvement in the sensitivity of the Z emulsion by Eastman Kodak around 1953. For example, Barocas and Righini (1954) (30) used Z emulsions with a dispersion of 570Å/mm to measure the HeI emission line in β Lyr. This line is useful in the study of chromospheres of cool stars. At present atlases of low to moderate resolution spectra using Z emulsion for a wide range of objects with wavelengths coverage around 1μ are readily available e.g. Wyller (1964) (31), Griffin (1964) (32), etc. However, the information content of the available spectra merits more detailed analysis.

The first image tube spectrograms using an S1 photocathode to record stellar spectra in the one-micron region were obtained at the Lowell Observatory by Fredrick (1961) (33). The stellar spectra obtained were usually of late-type stars (i.e. spectral class M and C stars), in order to determine the presence of the Cyanide, CN(0,0) band in the spectra. Many more atlases of stellar spectra at 1μ have been obtained with image tubes since Fredrick. For example, Lockwood (34) made studies of cool stars in the one-micron using an image tube. Spectra of a number of late-type stars were obtained with the Cassegrain spectrograph and 32 inch reflecting telescope of the Leander McCormick Observatory at reciprocal linear dispersion of 45Å/mm. The aim of the survey was to study differences in infrared stellar spectra as a

function of spectral class, the changes in the spectra of long-period variables with phase, and to search for indicators of stellar water vapour in the 1.1μ region.

Vaughan and Zirin (1968) (35) have studied and compared the merits of the three techniques i.e. the image tube spectrograms, photoelectric spectral scan and high resolution interferometer scanning by using them to observe the chromosphere HeI λ 10830Å and for line identification in G, K, and M stars. Table 1 provides historical forms of reference by listing the papers that report new observations of stellar spectra at one-micron (i.e. covering only $0.75 < \lambda < 1.2\mu$) from 1970 onwards (Spinrad and Wing (1969) have already reported papers before 1970). The first column in Table 1 indicates the author and the year of publication, column 2 giving the type of instrument, detector, telescope and wavelength interval covered, and finally column three summarises the nature of the project and results.

From this table it can be seen that there is still a need for high resolution stellar spectra at the one-micron region in order to do further qualitative infrared spectral classification of cool stars since there remain numerous molecular absorption bands some of which have not been identified due to the low spectral resolution.

In chapter 6 measurements will be given based on observations made, in May 1982, of a bright M3 giant star (HR 5490) in the Northern Hemisphere at wavelengths around 1μm (9748Å - 10153Å). At the same time a nearby hot star

TABLE 1

SELECTED PAPERS ($0.7 < \lambda < 1.2\mu$)

AUTHOR	INSTRUMENT USED	REMARKS OF OBSERVATIONS
Wing (1970)	prime focus scanner, Crossley telescope, Lick Obs., 0.75 - 1.10μ.	spectra of M supergiants and carbon stars. CN band in 1μ region.
Miller (1970)	prime focus scanner, S1 cathode, 120" telescope, Mt. Hamilton, 0.7 - 1.10μ.	spectra of infrared object IRC & 10216. 3 features of CN band identification.
Strom (1971)	Carnegie Image tube spectrograph 84" telescope, Kitt Peak National Observatory (KPNO), at 1-micron.	Search for young stellar objects at 1μ in dark cloud & HII region.
Mihalas (1972)	dual channel scanner, 36" telescope, KPNO, 4Å resolution λ 10096Å - λ 10154Å.	spectra of O and Of stars, observed the equivalent width of HeII λ 10124 absorption line.
Lockwood (1973)	dual channel scanner, 1 metre telescope, KPNO, 20Å resolution λ 9660Å - λ 10400Å.	spectra of cool M stars, observation of TiO and VO bands, TiO bands depress the continuum of cool M stars blueward of 1μ
Wing (1973)	prime focus scanner, Lowell Obs., Perkin Obs., Cerro Tololo Inter American Obs., and KPNO, 0.7 - 1.1μ.	8 years photometry at 1-micron of 1k Tauri, observed 1K Tauri varies at maximum light M8.1, and minimum light M10.
Giquerre(1973)	Image tube plates, 32" cassegrain telescope, Fan Mountain station at Leander McCormick Obs., 48Å/mm at 1μ.	Spectra of carbon stars, search for HCN bands at 1μ.
Lockwood (1974)	Photomultiplier tube, 0.9m and 1.3m telescope, KPNO, 0.78 - 1.05μ.	Photometry of IRC stars, Colours and photometric spectral types derived for molecular bands indices.
Hirai (1974)	Kodak IZ plates, 188cm reflector of Okayama Astrophysical Obs., Coude Spectrograph, 16Å/mm and 41Å/mm, 1.0μ - 1.08μ.	Spectra of carbon stars, observation of CN and C_2H_2 bands.

AUTHOR	INSTRUMENT USED	REMARKS OF OBSERVATIONS
Meisel (1975)	Vaughan pressure-scanned Fabry Perot, Interferometer, 24" reflector telescope, C.E.K. Mees Obs., around 1.08μ.	Spectra of alpha Virginis A and B. Observed HeI λ 10830Å and measured the equivalent width to determine spectral classification.
Andrillat (1975a)	Roucas grating spectrograph, 1.93m cassegrain telescope, Haute Provence Obs., 230Å/mm 0.8 - 1.1μ.	Spectra of Of and Wolf-Rayet stars, observed high temperature and low gravity of O star which is favourable for HeI 10830 emission.
Andrillat (1975b)	Roucas grating spectrograph, 1.93m cassegrain telescope Haute Provence Obs., 230Å/mm, 0.8 - 1.1μ.	Infrared spectra of peculiar emission line stars, observed spectral variations between 1974 to 1975, and identifications of lines.
Shanin (1975)	Image tube, 50" telescope, Izv. Krym Astrofiz. Obs., 480Å/mm, λ10580Å - λ11020Å.	Spectrum of Geminoroum cepheid. Line identification and central lines intensities. Measured the equivalent width of HeI 10830Å in 700mA.
Andrillat (1976)	Roucas grating spectrograph, S1 photo-cathode, 1.93m telescope, Haute Provence Obs., 230Å/mm, 0.8 - 1.1μ.	Spectra of peculiar emission line objects with infrared excess. Observed features of Paschen series, CaII triplet, HeI 10830, OI λ8466, [SIII] λ 9069, and 9532, and FeIII λ10524. Strong emission at 9999Å remains unidentified.
Andrillat (1976)	Roucas grating spectrograph, 1.93m telescope, Haute Provence Obs., 230Å/mm, 0.8 - 1.1μ.	Spectra of hot stars and planetary nebulae. Analysis of these spectra.
Zirin (1976)	RCA image tube, 72" Coude focus telescope, Mt. Palomar 15.6Å/mm, 1.07 - 1.1μ.	Observations of the λ 10830Å helium lines in 198 stars. This line is significant as a measure of stellar activity. 80% of G and K star show this line.
Swing (1977)	Roucas grating spectrograph, 1.93m cassegrain telescope, Haute Provence Obs., 230Å/mm, 0.8 - 1.1μ.	Spectrum of the Egg nebulae CR2688. No detectable features except emission lines of the CaII triplet and a number of Paschen series.

AUTHOR	INSTRUMENT USED	REMARKS OF OBSERVATIONS
Shanin (1978)	Image tube, 50" telescope, Izv. Krym Astrofiz Obs., 0.8μ - 1.1μ.	spectrum of HM SGE in 1977. Identifications of lines.
Vreux (1979)	Roucas grating spectrograph, 1.93m telescope, Haute Provence Obs., 230Å/mm, 0.9 - 1.1μ.	spectra of O stars, Observations of the HeII and H lines. New observations of HeI 10124Å line and H λ10049 (P_8) line.
Andrillat (1979)	Roucas grating spectrograph, two stage image tube (ITT F-4718), 1.93m telescope, Haute Provence Obs., 230Å/mm, 0.75 - 1.2μ.	spectra of O stars. Observed HeI λ10830A and gives quantitative data analysis. Intensity of emission is correlated to the temperature of the star and to the rate of mass loss.

(α CrB) was also observed, with the same apparatus, to provide calibration data for the removal of telluric lines etc. (Since this star has similar right ascension and declination to the M3 giant the air masses involved should be much the same).

REFERENCES

1. McMullan, D., and Wehinger, P.A. (1977), Endeavour 1, 32.

2. Coleman, C.I., and Boksenberg, A. (1976), Contemp. Phys. 17, 209.

3. Boksenberg, A. (1970), in Proc. Symposium at Princeton University (NASA SP-256), P.77.

4. Lowrance, J.L., Morton, D., Zucchino, P., Oke, J.B., and Schmidt, M. (1972), Astrophys. J. 171, 233.

5. Fekel, F. Jr., Lacy, C.H., and Tomkin, J. (1979), Close Binary Stars : Observations and Interpretation IAU Symposium No. 88, Toronto CA, USA (Dordrecht, Netherlands, Reidel 1980).

6. Aikans, R.S., Lynds, C.R., and Nelson, R.E. (1976), SPIE Proc., 78, 65.

7. Marcus, S., Nelson, R., and Lynds, R. (1979), SPIE Conference, "Instrumentation in Astronomy III", 172, 207.

8. Low, F.J. (1969), Infrared Astrophysics, Science 164, 501-505.

9. Moss, T.S., Burrell, G.J., and Ellis, B. (1973). Semiconductor Opto-Electronics, Butterworth & Co. Ltd. (London).

10. Rosenberg, H.M. (1979), The Solid State an Instroduction to the Physics of Crystals for Students of Physics, Material Science, and Engineering, 2nd Edition, Clarendon Press, Oxford.

11. James, T.H. (1966), The Theory of the Photographic Process, 3rd ed., Macmillan, New York.

12. Engel, C.E. (1968), Photography for the Scientist, Academic, New York.

13. Latham, D.W. (1971), Am. Astron. Soc. Photo-Bull., No. 1, 28.

14. Weimer, P.K. (1975), Advances in Electronics and Electron Physics, Vol. 37, 182-259, Academic Press Inc.

15. Baum, W.A. (1964), Ann. Rev. Astron. Astrophys., 2, 165.

16. White, M.H., Lampe, D.R., Blaha, F.C., and Mack, I.A. (1974a), "Characterization of Surface Channel CCD Image Arrays at Low Light levels", IEEE Jour. of Solid State Circuits SC-9, 1-13.

17. Sequin, C.H., and Tompsett, M.F. (1975), Advances in Electronics and Electron Physics. Supplement 8, Academic Press, Inc.

18. Miller, W.C. (1971), Am. Astron. Soc. Photo. Bull., No. 2, 3.

19. Lallemand, A. (1962), Astronomical Techniques, W.A. Hiltner, Ed., University of Chicago Press.

20. Brooker, L.G.S. (1966), The Theory of the Photographic Process, 3rd Ed. T.H. James Ed., Macmillan, New York, p. 198.

21. Millikan, A.G. (1974), Am. Sci. 62, 324.

22. Webb, J.H. (1948) J. Opt. Sci. Am. 38, 312.

23. Spinrad, H. and Wing, R.F. (1969), Ann. Rev. Astron. Astrophys. 7, 249-99.

24. Carbon, D.F. (1979), Ann. Rev. Astron. Astrophys. 17, 513-549.

25. Gaydon, A.G. (1968), Dissociation energies and spectra of diatomic molecules, Chapman and Hall, London.

26. Peaslee, D.C., and Mueller, H. (1955) Elements of Atomic Physics, Prentice-Hall Inc., New York.

27. Spinrad, H. and Wing, R.F. (1969) Ann. Rev. Astron. Astrophys. 7, 249-99.

28. Merrill, K.M. and Ridgway, S.T. (1979) Ann. Rev. Astron. Astrophys. 17, 9-41.

29. Sanford, R.F. (1947), Publ. Astron. Soc. Pacific, 59, 136.

30. Barocas, V. and Righini, J. (1954) Observatory, 74, 73.

31. Wyller, A.A. (1964), 12th Liege Colloquim (Mem. 8° Soc. Roy. Sci. Liege, 5th Ser., 9), 479.

32. Griffin, R.F. (1964), Monthly Notices of The Royal Astronomical Society, 128, 287.

33. Fredrick, L.W. (1961) Lowell Observatory Bulletin, 5, 149.

34. Lockwood, G.W. (1968), Ph.D. Thesis, University of Virginia, Charlottesville.

35. Vaughan, A.H., Jr., and Zirin, H. (1968), Astrophys. J., 152, 123.

36. Wing, R.F., and Spinrad, H. (1970), Astrophys. J., Vol. 159, No. 3, Pt. 1, 973-984.

37. Miller, J.S. (1970), Astrophys. J., Vol. 161, No. 2, Pt. 2, L95-99.

38. Strom, S.E., Strom, K.M., Carrasco, L., Grasdelan, G., and Derenzo, S. (1971)., Bulletin American Astronomical Society, Vol. 3, No. 4, Pt. 1, 479.

39. Mihalas, D., and Lockwood, G.W. (1972), Astrophys. J., vol. 175, No. 31 Pt. 1, 757-764.

40. Lockwood, G.W. (1973), Astrophys. J., Vol. 180, No. 3, Pt. 1, 845-855.

41. Wing, R.F., and Lockwood, G.W. (1973), Astrophys. J., Vol. 184, No. 3, Pt. 1, 873-880.

42. Giquerre, D.T. (1973), Astrophys. J., vol. 186, No. 2, Pt. 1, 585-588.

43. Lockwood, G.W. (1974), Astrophys. J., vol. 192, No. 1, Pt. 1, 113.

44. Hirai, M. (1974), Publication of the Astronomical Society of Japan, vol. 26, No. 2, 163-188.

45. Meisel, D.D. (1975), Astrophys. J., vol. 198, No. 3, Pt. 1, 551-553.

46. Andrillat, Y., and Vreux, J.M. (1975a), Astronomy and Astrophysics, vol. 41, No. 2, Pt. 2, 133-136.

47. Andrillat, Y., and Houziaux, L. (1975b), C.R. Hebd. Scances Acad. Sci. B. (France). vol. 281, No. 15, 321-323.

48. Shanin, G.I., and Scherbakov, A.E. (1975), Izv. Krym. Astrofiz. Obs. (USSR), vol. 53, 187-95.

49. Andrillat, Y., and Swings, J.P. (1976), Astrophys. J. Letter Ed. (USA), vol. 204, No. 3, Pt. 2, L123-5.

50. Andrillat, Y. (1976), Mem. Soc. Roy. Sci. Liege 8° (Belgium), vol. 9, 355-360, (In French)

51. Zirin, H. (1976), Astrophys. J., vol. 208, No. 2, Pt. 1, 414-425.

52. Swings, J.P. and Andrillat, Y. (1977), Astronomy and Astrophysics, vol. 55, No. 3, Pt. 2, 461-466.

53. Shanin, G.I. (1978), Pisma V Astron. Zh. (USSR), vol.4, 187-190.

54. Vreux, J.M., and Andrillat, Y. (1979), Astronomy and Astrophysics, vol. 75, No. 1-2, Pt. 2, 93-96.

55. Andrillat, Y. and Vreux, J.M. (1979), Astronomy and Astrophysics, vol. 76, No. 2, Pt. 1, 221-225.

CHAPTER 2

CHARGE COUPLED DEVICES, HOW THEY WORK AND LIMITATIONS

2. INTRODUCTION

The idea of storing and transferring signal charge in an array of closely spaced capacitors on an isolated surface of a semiconductor was first proposed by Boyle and Smith (1) in their search for an electrical analog to magnetic bubble devices (2). This concept of storing and transferring signal charge is known as 'charge coupling' and the device is called a charge coupled device (CCD). In view of the potential of this concept for other applications such as signal processing, imaging, etc., it has been improved further for various applications by other workers. Since the conception of this idea of charge coupling, a wide variety of charge coupled devices have been built by companies such as Texas Instruments, RCA, General Electric Company, etc.

Two types of CCDs are commonly in use, namely the surface channel charge coupled device (SCCD) and the buried channel charge coupled device (BCCD). The name 'surface' or 'buried' associated with the CCD indicates the signal handling operation of the device. The Nuclear Instrumentation (NI) group at Durham University has acquired buried channel charge coupled devices (BCCDs) from the General Electric Company (GEC). The BCCDs provided by GEC are of two versions: the bulk and the epitaxial substrate version. Both types are primarily designed as frame transfer organisation intended for television applications.

This chapter describes the basic features of a charge

coupled device (i.e. BCCD type). There are many applications of CCDs, however this chapter concentrates on their application to low light level imaging intended for astronomical work. In order to achieve this aim the chapter begins with an introduction to the concept of the charge coupled device (the BCCD type) in terms of potential distribution in the device as a function of integrated charge. This is followed by a description of the operation and performance limitations of the General Electric Company buried channel charge coupled device as intended for astronomical work.

2.1 Buried Channel Charge Coupled Device (BCCD)

The name of this device derives from the way charge is stored and transferred within it. The basic structure of BCCD is shown in Figure 2.1. It consists of closely spaced electrodes each of which forms a MOS capacitor, each electrode operating in a manner similar to the gate of a MOS transistor. Signal information, usually in the form of a quantity of electric charge (electrons and holes) can be stored under the electrodes. These charges are localised under the electrodes (in the n-type layer) with the highest applied voltages, because the positive potentials on the electrodes (V_G) cause the underlying silicon to be driven into depletion, thus attracting the negatively charged electrons. As apparent from the shape of the potential distribution beneath the electrodes (Figure 2.1), the electrons are stored in the depletion region and this region is commonly called a 'potential well'. The BCCD can transfer the charge packets in the potential wells in discrete time increments

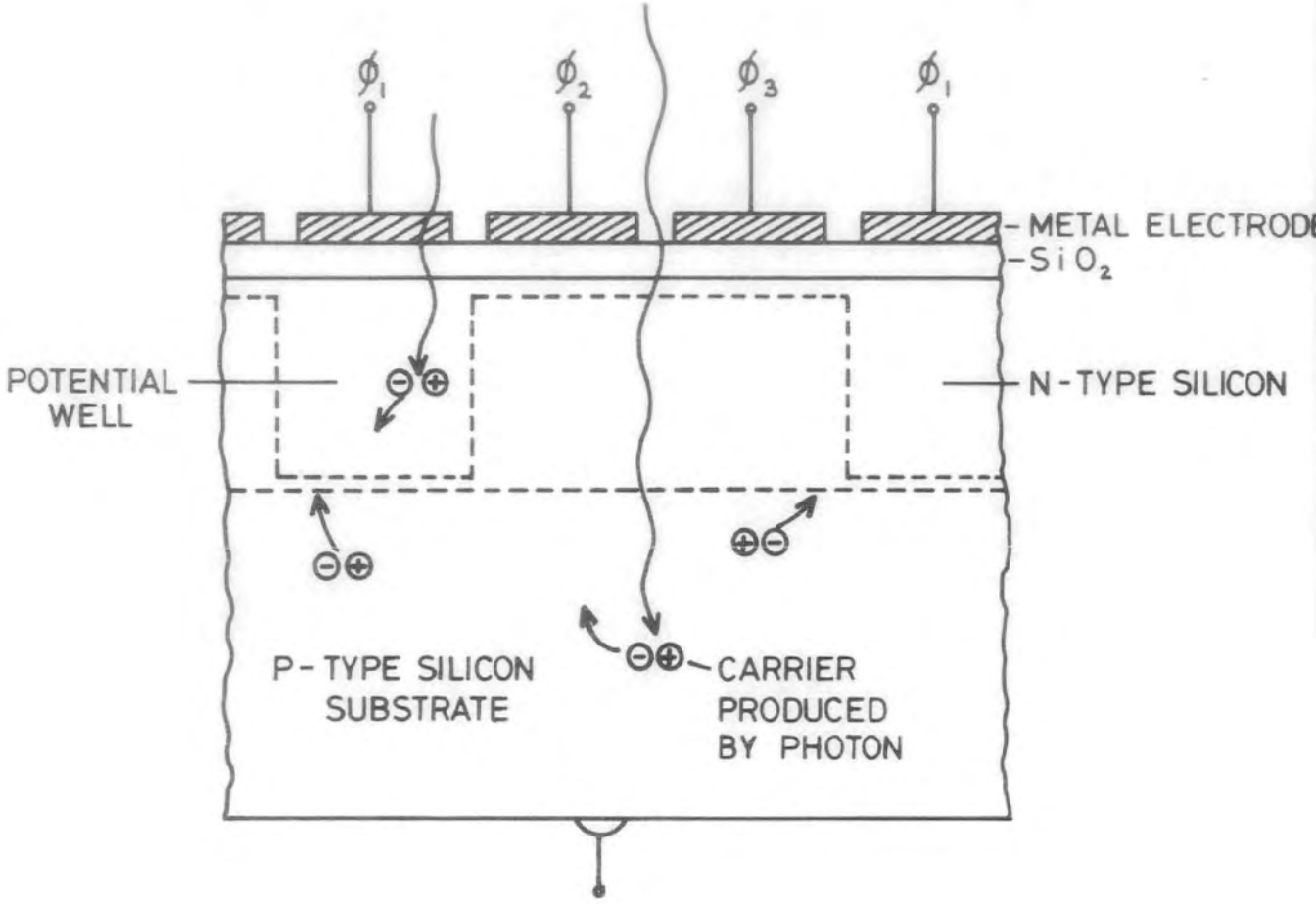

FIG. 2·1 BASIC STRUCTURE OF CCD

by controlling the voltages on the electrodes. The technique by which the charges can be transferred from one potential well to the next is called 'charge coupling'. This technique will be described later in this section. The charge packets can be detected via capacitive coupling at the output of the device.

The above physical processes can be described in a more quantitative manner by employing the profile of potential versus distance into silicon as shown in Figure 2.2. Figure 2.2 shows four separate cases of the variation of potential from the electrode through to the silicon substrate at ground potential. When an arbitrary fixed bias V_G is applied to the electrode, the applied voltage is supposed to be divided between the semiconductor and the oxide. In practice, this is not the case, because of the structure of the device, the electron energies at the Fermi level in the gate electrode and in the semiconductor will, in general, be different. This energy difference is expressed as a difference in work function (3). To overcome this work function difference, the gate voltage applied must be greater than this voltage before any conduction can take place in the semiconductor. When the gate voltage applied is equal to the work function voltage, then this voltage is called the flatband voltage V_{FB}. If the applied gate voltage is greater than this voltage, then the difference in voltage ($V_G - V_{FB}$) will be divided between the oxide and the semiconductor as illustrated in Figure 2.2 (for case (a) is

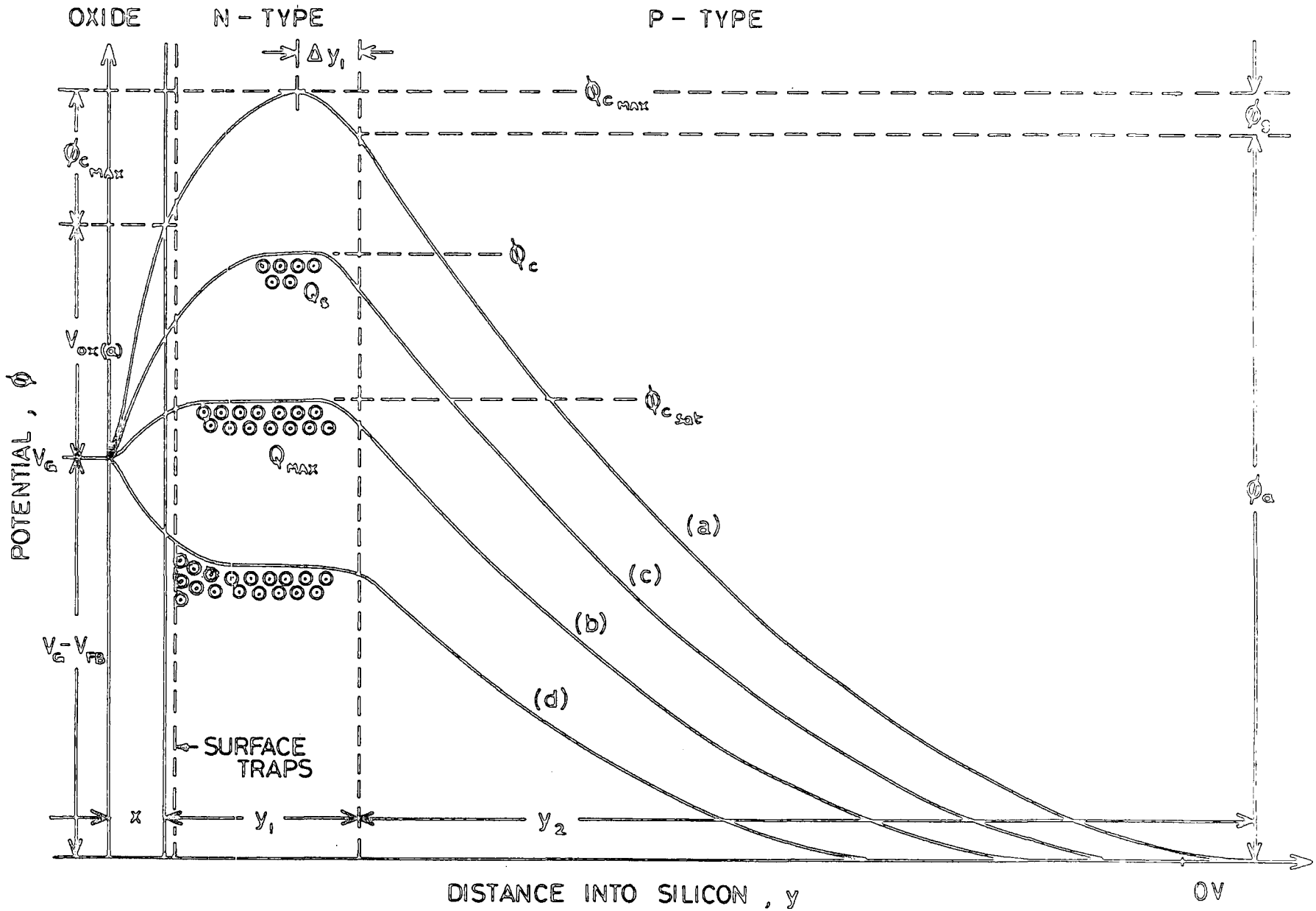

FIG. 2·2 THE CHANNEL POTENTIALS OF BCCD

shown). The relationship between the various potentials and the device parameters has been derived by Barbe (4) using Kirchoff's law and therefore shall not be considered here.

Consider case (a) in Figure 2.2, in the absence of signal charge, the potential beneath the electrode in the 'channel region' (the n-type layer) has a maximum positive value $\phi_{c\ max}$. This is equivalent to the depth of the potential well formed underneath the electrode. In the second case (b), the potential well is said to be saturated. The signal charge is denoted as Q_{max} as shown in Figure 2.2(b). It can also be said that the charge is at an equi-potential and distributed over most of the depth of the n-type layer. Therefore the potential in the channel region is now decreased to $\phi_{c\ sat}$. In the third case (c), the potential well is partially filled with signal charge Q_S, where $Q_{max} > Q_S > 0$. Therefore the potential in the channel region will assume an intermediate level between the no signal charge and charge saturation levels condition i.e. $\phi_{c\ sat} < \phi_c < \phi_{c\ max}$ as shown in Figure 2.2(c). The fourth case (d) is when the potential well is overloaded with signal charge, i.e. the condition when $Q_S > Q_{max}$. This results in excess signal charge being spilled out of the potential well. Some of this excess signal charge will be in contact with the silicon surface and so be trapped via surface states (see Figure 2.2(e)), while other excess signal charge will be spread to adjacent electrodes of the array causing a phenomenon commonly known as 'blooming'. This

occurs because the excess signal charge depresses the channel potential below that of the adjacent electrodes which are held at a lower potential, thus creating a lateral field which accelerates further excess signal charge to the next CCD electrodes.

Charge transfer takes place between adjacent electrodes when the potential on the first electrode storing charge is taken to its lowest value as the potential on the second electrode receiving charge is taken to its highest value. Transfer takes place because electrons will always flow toward the region of most positive potential. The charge transfer process (charge coupling technique) is shown in Figure 2.3 and outlined below; assuming that the signal charges to be moved along the channel are electrons. Note that three phase drive pulses ϕ_1, ϕ_2, and ϕ_3 are used to transfer the signal charge. These pulses are not generated in the CCD and must be produced in the external electronics.

At the time $t = t_a$ charge resides in the potential wells under the ϕ_1 electrodes which at this moment are at their most positive voltage relative to the grounded substrate. At $t = t_b$, the ϕ_2 electrodes have also reached the maximum positive voltage and thus creating a second potential well into which the charge (electrons) under a ϕ_1 electrode begins to move. The transfer of charge to the ϕ_2 potential wells is aided at time $t = t_c$, by the lowering or reducing of the voltage on the ϕ_1 electrodes ultimately removing these ϕ_1 wells. During this time the barrier under electrode

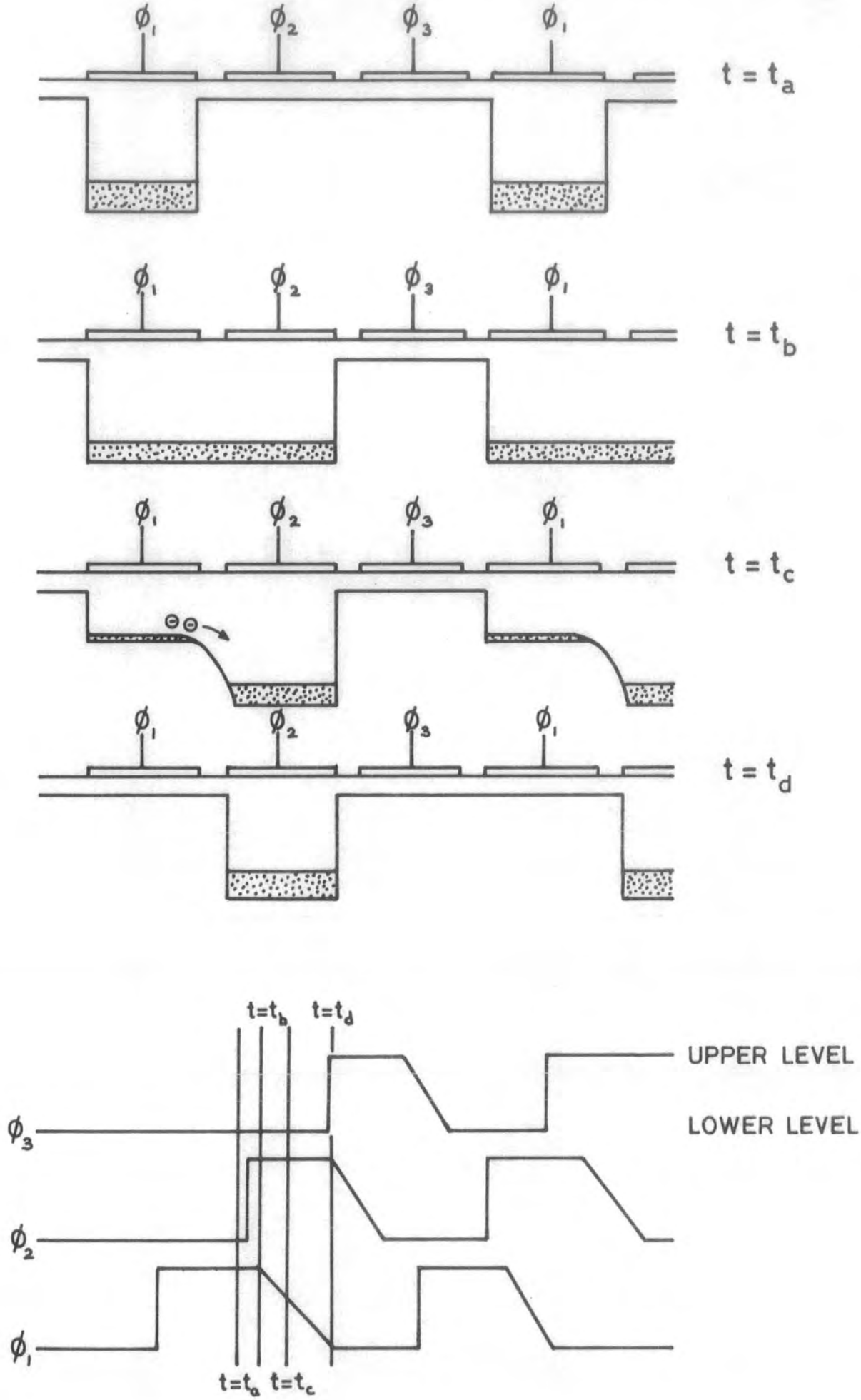
ϕ_1
ϕ_2
ϕ_3
ϕ_1
$t = t_a$
$t = t_b$
$t = t_c$
$t = t_d$
$t=t_b$
$t=t_d$
UPPER LEVEL
LOWER LEVEL
ϕ_3
ϕ_2
ϕ_1
$t=t_a$
$t=t_c$

FIG. 2·3

ϕ_2 has the least positive voltage which prevents any charges from moving backward i.e. to the left. The transfer of charge is completed at time $t = t_d$ and the original charge is now present entirely under the ϕ_2 electrode. Thus the charges move from one potential well to the next every clock period. As the movement of the charge is controlled by external voltages, transfer of charge can be achieved in two dimensions as well. Therefore a two dimensional area type charge coupled device can also be constructed and operated on the same principles as above. The design and operation of this type of BCCD will be described in the next section.

During the charge transfer process if the signal charge comes into contact with the surface of the semiconductor insulator interface, then the advantages of buried channel operation are lost because charge trapping takes place through the surface states and very low charge transfer efficiency results on signal read out. This therefore, sets the limit on maximum charge handling capability.

In the above discussion the substrate voltage (V_{ss}) is kept constant (i.e. at ground potential). However, if the substrate voltage V_{ss} is increased positively, then the potential difference across the p-n-junction comprising the buried channel boundary i.e. $\phi_c - V_{ss}$ is decreased. This decreases the electric field at the junction and the depth of the depleted silicon. As a result of this, dark current may be reduced. This is because dark current generated

in the bulk silicon is proportional to the depleted volume (5). Some reduction of white video defects has also been observed in the laboratory work when the substrate voltage is increased. Therefore the variation of substrate voltage gives reduction in dark current and video defect levels. However, it has little effect on device operation other than slight modification of the values of $\phi_{c\ max}$ (at given voltage V_G) and Q_{max} as illustrated in Figure 2.4.

2.2 A Two Dimensional Area Type Buried Channel Charge Coupled Device

In the previous section, it has been noted that the device can also be built as a two dimensional array. The practicability of imaging with two dimensional charge coupled device was performed by Bell Telephone Laboratory (6) in 1971. Such possibilities have led to this type of device being commercially developed for television applications. This device later became attractive to astronomers because it appears to be a promising detector that can be used in a wide variety of applications. For this reason the following sections will concentrate on the descriptions of the features and limitations of a particular device intended for astronomical work.

2.2.1 Design and Layout. The charge coupled device purchased from the General Electric Company is type P8600 : 385 x 576 pixel area image sensor. This device operates in the buried channel mode. It was chosen because it shows good responsivity towards the red end of the spectrum range especially near the one-micron region and

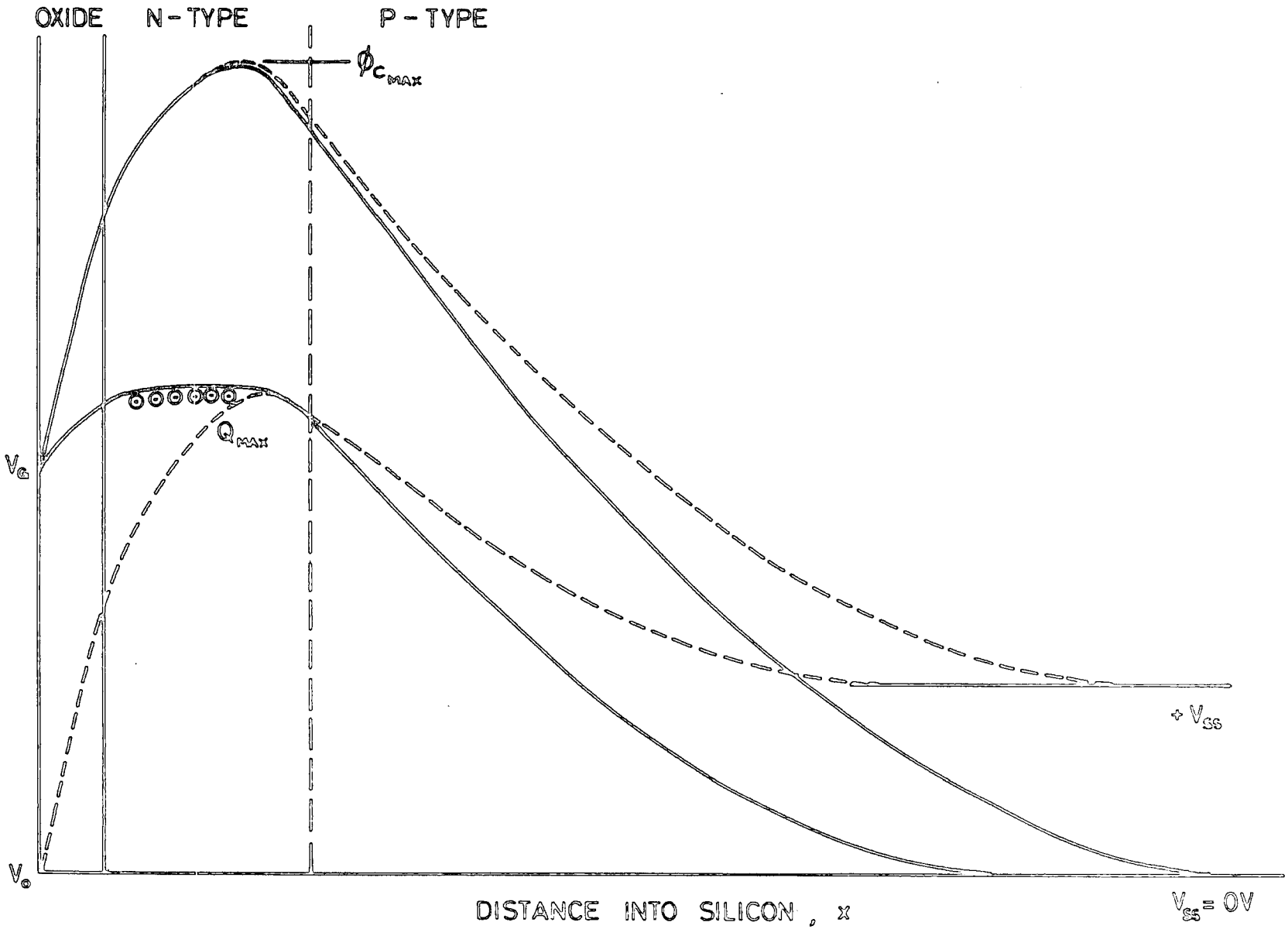

FIG. 2·4 SUBSTRATE BIAS

also low readout noise. The one-micron region is the region of interest to look at for the purpose of our astronomical work. Details of this work will be described in chapter six.

The basic design of the CCD type P8600 (385 x 576 pixels) is shown in Figure 2.5. The device consists of an array of polysilicon electrodes with charge transfer channels defined by 'channel stop' (7) isolation regions. These polysilicon electrodes are connected in sequence to the bus lines carrying the three phase drive pulses (as described previously) and are grouped in three sections: an upper 'image section', a lower 'store section' and a line readout section at the bottom of the array to transfer signals to the on-chip charge detection amplifier. The image section consists of 288 vertical by 385 horizontal pixels and is used for imaging (i.e. collecting signal information). The store section comprises 290 vertical by 385 horizontal pixels. The two extra vertical lines are to accommodate any residual signals that might arise through inefficient charge transfer out of the image section. In a full frame mode, common connections are made to the image and store sections such that the whole array (i.e. 385 x 578 pixels) is used for imaging. However, this mode is only possible with long integration times under cooled conditions, such that the relatively long read out period of this approach does not give rise to significant frame-shift smear (i.e. spurious charge picked up during read out). This operational mode will be considered in the next section. The line read

FIG. 2.5 DEVICE SCHEMATIC

out section or the output register has a total of 400 elements. One register element is associated with each of the horizontal pixels in the array; plus eleven extra at the output end of the register and four at its input. For television applications these fifteen extra registers may be used to establish a black reference level at the start of each line. For our purpose, these fifteen extra registers are used as a d.c. offset reference level at the start of each line. Therefore the drift of d.c. level with temperature between the start and the end of each line can be monitored.

The charge detection amplifier is illustrated schematically in Figure 2.6. There are two identical output circuits incorporated on chip. Each output circuit consists of an output diode connected to a dual gate MOS transistor switch T_1 and a second MOS transistor T_2 operated in the source follower mode. Only one of the output circuits is used for charge detection. The other output circuit is called a 'dummy' output because it receives no signal charge. The reason for this dummy output being incorporated will be described later in this chapter. The device is supplied in a 0.9 inch wide 30 pin DIL package with an optical window.

2.2.2 Device Operation. Operation of the charge coupled device type P8600 (385 x 576 pixels) in the full frame transfer mode requires the application of two sets of three phase drive pulses; $V\phi_1$, $V\phi_2$, $V\phi_3$ (for vertical electrodes in image section), $H\phi_1$, $H\phi_2$, $H\phi_3$ (for horizontal electrodes in read out section), an output reset pulse ϕ_R, and various d.c. bias voltages for the charge detection amplifier. Typical pulse amplitudes and d.c. levels employed are shown

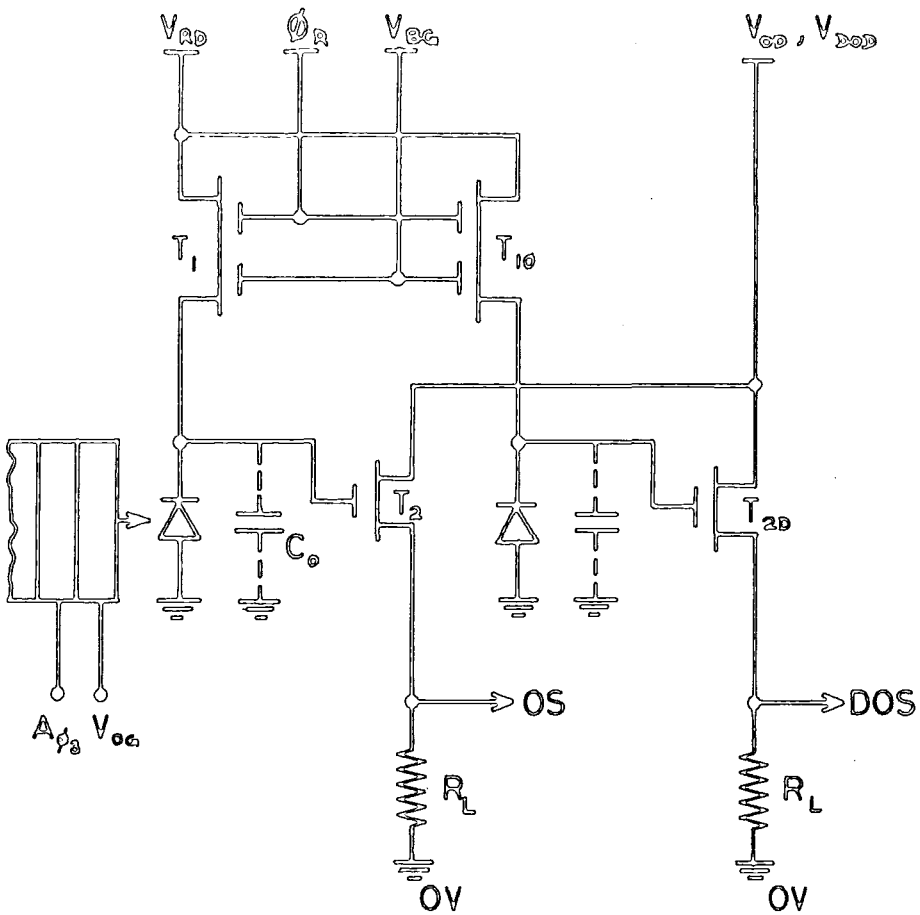

FIG. 2·6 P8600 OUTPUT CIRCUIT

in Table 2.1.

The array operates as outlined below: firstly, the electrodes of one phase in the image section must be held at a 'high' level (i.e. the electrode is biased with a positive potential) thus creating potential wells under the electrodes. When an optical image is focussed onto the image section, photons will penetrate the electrode structure and generate electron hole pairs in the underlying silicon substrate. The electrons will diffuse to the nearest biased electrode where they are collected in the potential well as signal. The holes diffuse down into the substrate where they are effectively lost through recombination processes. The quantity of charge collected in the potential well is proportional to the local light intensity and the time allowed for collection. At the end of the integration period the quantity of charge collected in the image section is transferred into the line read out section. The lowest line of charges being transferred in parallel into the lower line read out section. This last transfer is achieved through one cycle of the vertical (Vϕ's) drive pulses with one of the clock phases of the line read out section held high. In a full frame slow scan mode charge transfer between the last Vϕ_3 electrode and the line read out section is recommended by G.E.C. to be done with both Hϕ_1 and Hϕ_2 held at high level, as shown in Figure 2.7. When the voltage on the last electrode, Vϕ_3 goes low, charge transfer takes place across the upper edge of the Hϕ_1 and Hϕ_2 electrodes.

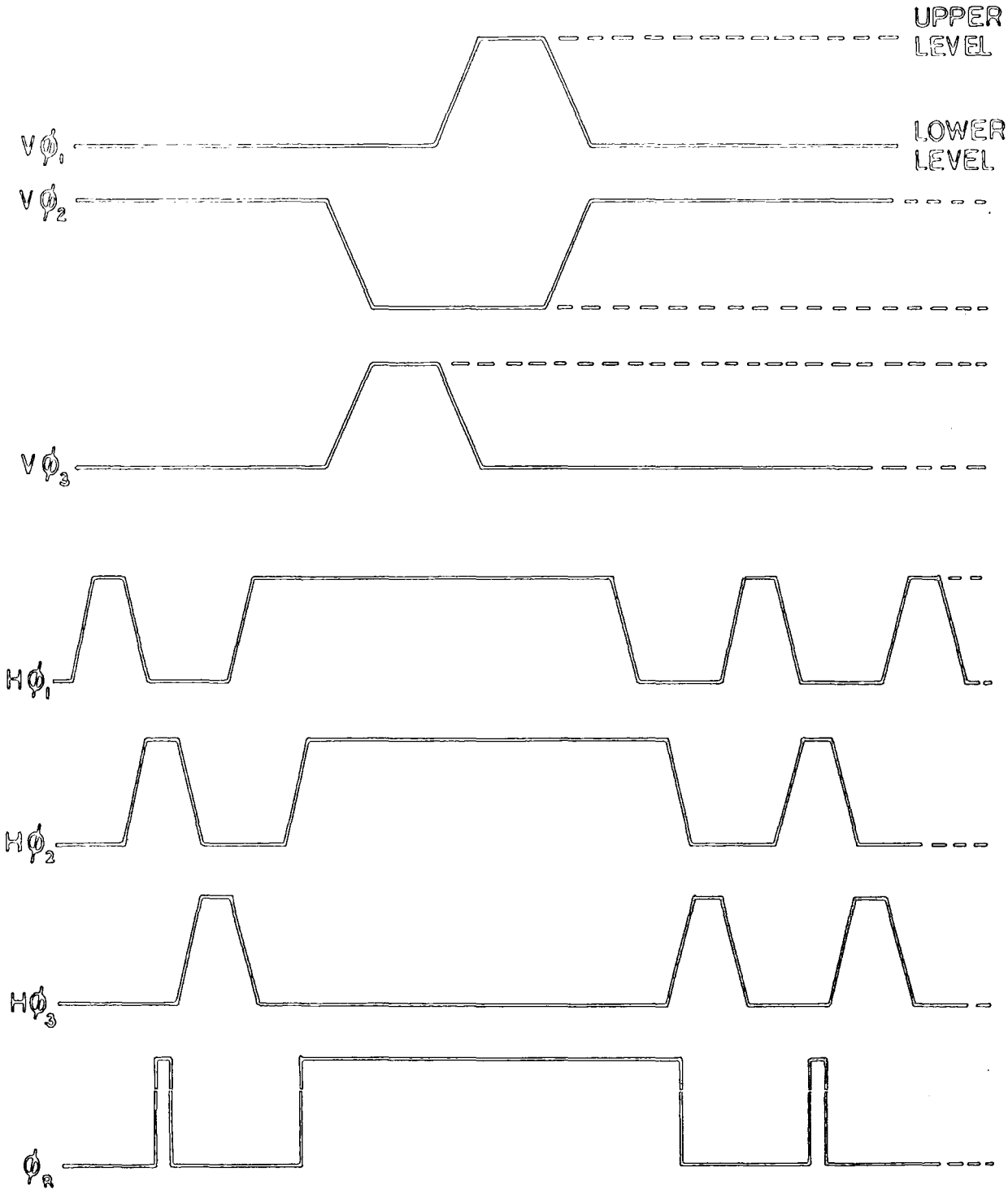

FIG. 2·7

TABLE 2.1

TYPICAL OPERATING VOLTAGES

OF THE GEC CCD TYPE P8600

	D.C. Level (volts)	Pulse Amplitude Level (Volts) Lower	Upper
Image Section $V\phi_1$		-8.75	2
Drive Pulses $V\phi_2$		-8.75	2
$V\phi_3$		-8.75	2
Line Readout $H\phi_1$		-8.75	4
Section Drive $H\phi_2$		-8.75	4
Pulses $H\phi_3$		-8.75	4
Reset Pulse ϕ_R		-8.75	1
Substrate V_{SS}	0		
Reset Transistor Drain V_{RD}	4.99		
Reset Transistor Bias Gate V_{BG}	14.00		
Output Transistor Drain V_{OD}	14.49		
Dummy Transistor Drain V_{DOD}	14.49		
Output Gate V_{OG}	-7.20		
Output Transistor Source V_{OS}	9.19		
Dummy Transistor Source V_{DOS}	9.19		
Antiblooming Drain Voltage V_{ABD}	14.00		
Antiblooming Gate Voltage V_{ABG}	-9.02		

After all the charges in the lowest line of the image section have been transferred under the $H\phi_1$ and $H\phi_2$ electrodes of the line read-out section, then by application of the $H\phi$s drive pulses the line of charges is sequentially transferred to the on-chip charge detection amplifier which converts the charge signals into a voltage modulated video output. This voltage is then measured by an external video pre-amplifier. Once all the line of charges in the line read-out section has been read out, the next line of charges is then transferred down from the image section to the line read-out section and read out in the same manner.

During the charge transfer process, some of the signal charge may be lost due to charge trapping in the potential well or at the surface of the semiconductor-insulator interface. This loss of signal charge results in reduction of charge transfer efficiency of the device. In the laboratory tests it has been observed that the charge transfer efficiency of this device is also associated with the clock level of the sets of three drive pulses in each section (image and read-out section). When the upper levels of the vertical and horizontal clocks ($V\phi_1$, $V\phi_2$, $V\phi_3$ in image section and $H\phi_1$, $H\phi_2$, $H\phi_3$ in line read-out section) are being adjusted separately, it is observed that the effects of leakage and streaking present in the array are greatly reduced or may disappear completely as can be seen on the video monitor screen. But, when the lowest levels of both clocks are being adjusted separately, no changes take place on the video monitor screen. This implies that the upper level

of the clocks is a critical factor for the charge transfer efficiency of the device. In general it was found that good transfer efficiency could be achieved by adjustment of the upper level, overlap point (between the same set of clocks) and correct three phase sequence of the vertical and horizontal clocks.

2.2.3 On-chip Charge Detection Amplifier. A detailed output circuit of the CCD type P8600 (385 x 576 pixels) is shown in figure 2.8. The output circuit has been described previously therefore only the operation of the output circuit will be explained in detail. Before the signal charge in the output register or the line read-out section is transferred into the output diode, the transistor T_1 is turned 'on' by application of a reset pulse ϕ_R which goes high, thus charging the output node capacitance C_o to a fixed applied potential V_{RD} (as shown in Figure 2.9). As the reset pulse ϕ_R goes low, the transistor T_1 is turned off leaving the output node capacitance charged to this potential (V_{RD}). The signal charge under the last $H\phi_3$ electrode is transferred into the output diode as the $H\phi_3$ pulse goes low. This signal charge partially discharges the output node capacitance causing the potential on it to change. This change in potential (assuming V_o) is proportional to the quantity of charge (assumed q_o) being read out. This potential is then present at the output source terminal with transistor T_2 operating as a linear voltage amplifier (with a gain value depending on the load used) to act as a buffer between the high impedance of the output diode and the much lower impedance of the following off-chip video circuitry.

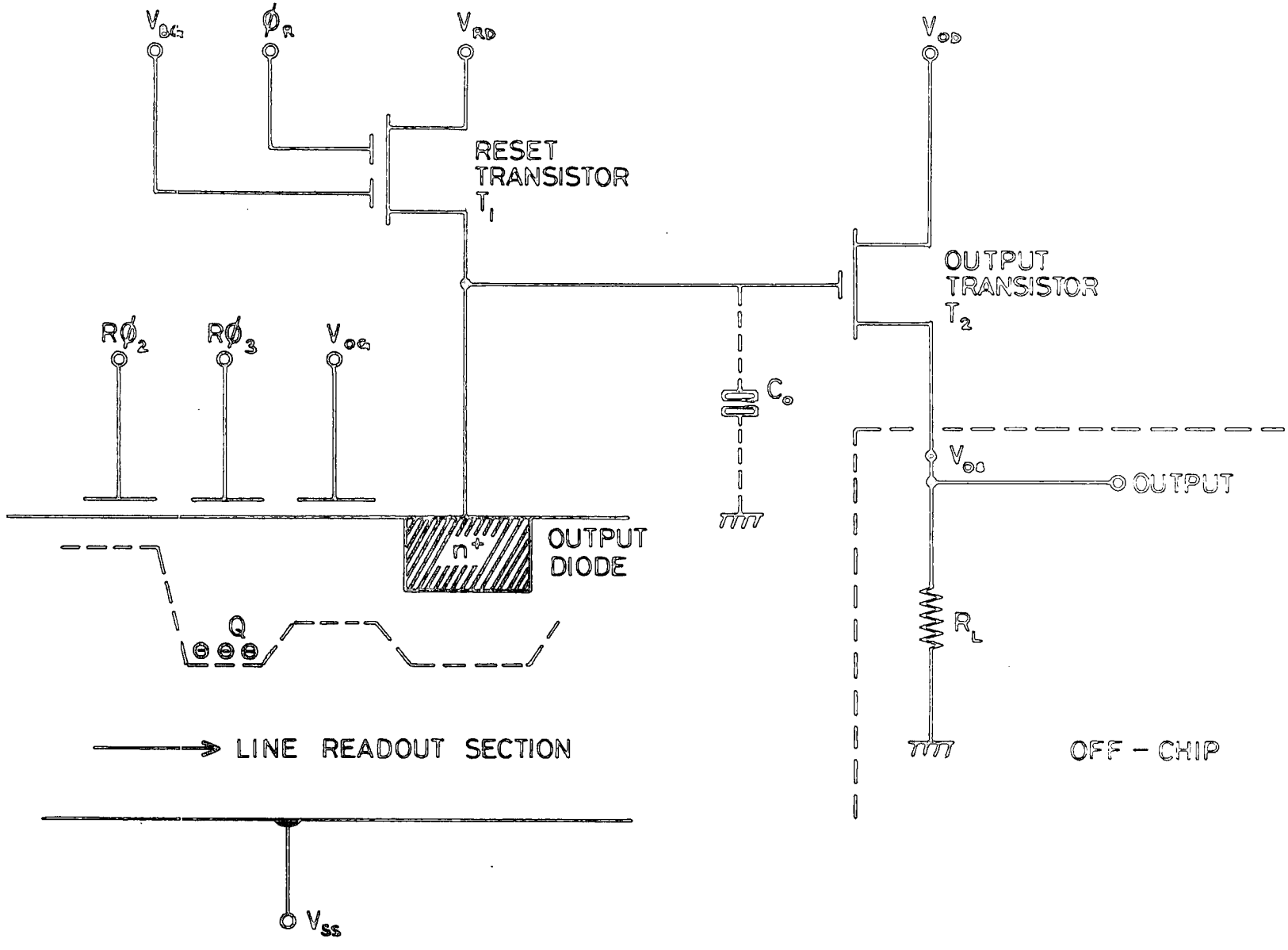

FIG. 2·8 DETAILED OUTPUT CIRCUIT

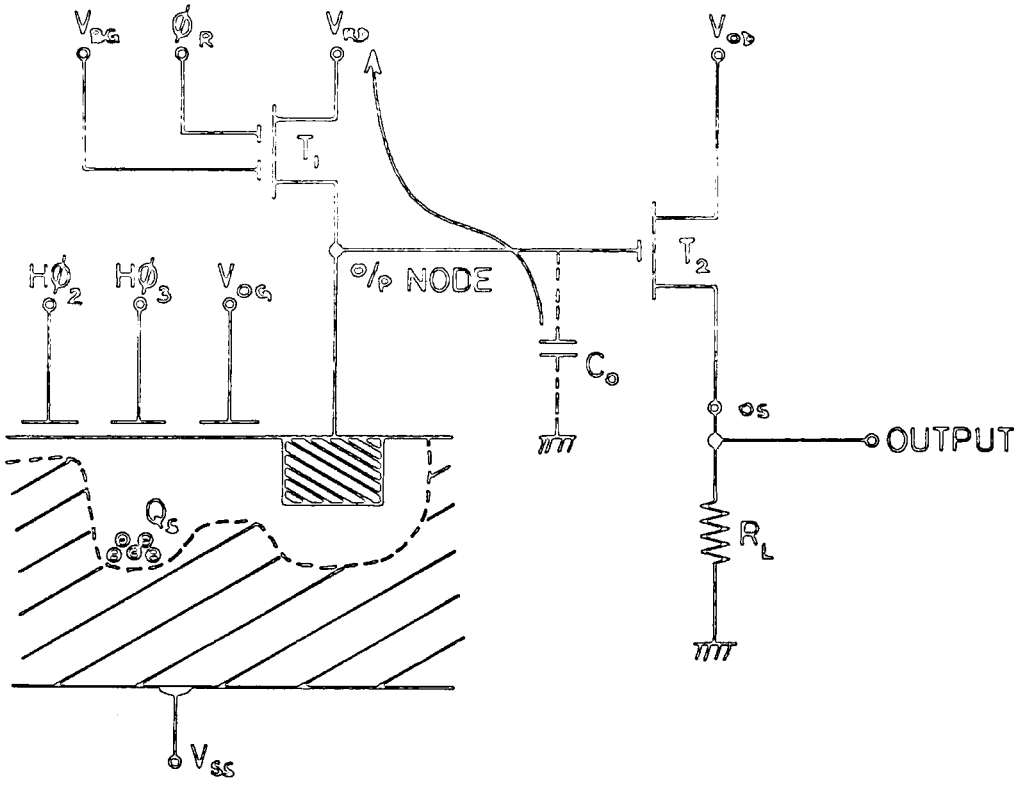

(a) RESET MODE

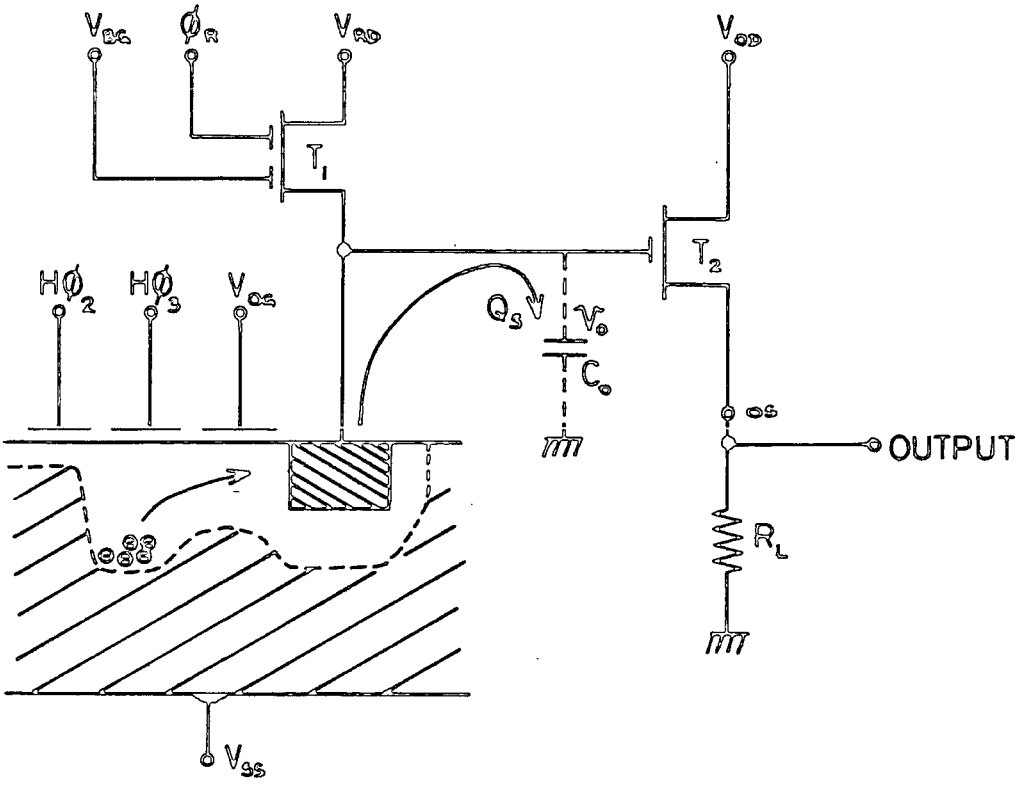

(b) CHARGE OUTPUT

FIG. 2·9

However, this potential is superimposed on the mean d.c. level preset at OS, denoted as V_{OS}. The output diode is again reset to V_{RD} by ϕ_R to prepare for the read-out and detection of the next signal charge.

The output gate (OG) (shown in Figure 2.8) has a dual function; firstly to isolate the line read-out section from the charge detection amplifier, secondly to act as a 'potential barrier' such that signal charge is only transferred into the output diode as the $H\phi_3$ pulse goes low. Therefore, it also helps to prevent pick-up of $H\phi_3$ pulses by the output diode. The reset bias gate denoted as BG (see figure 2.9) is used to reduce feedthrough of the reset pulse by partially screening the output diode from ϕ_R.

However, there is still some reset feedthrough (V_f) present in the above operation as shown in Figure 2.10). This reset feedthrough may be reduced with the 'dummy' output incorporated on the chip. Since this dummy output is of identical design to the 'real' output, its output at DOS (illustrated in Figure 2.6) must have similar reset feedthrough to that present at OS. Hence, using a differential voltage amplifier in the external video circuitry this reset feedthrough can be minimised.

In the present device operation the reset feedthrough V_f is removed through using the correlated double sampling technique. In this technique the signal waveform is sampled twice, once after resetting and again after charge has been transferred to the output node. The final output is the difference between the two values, thus eliminating reset

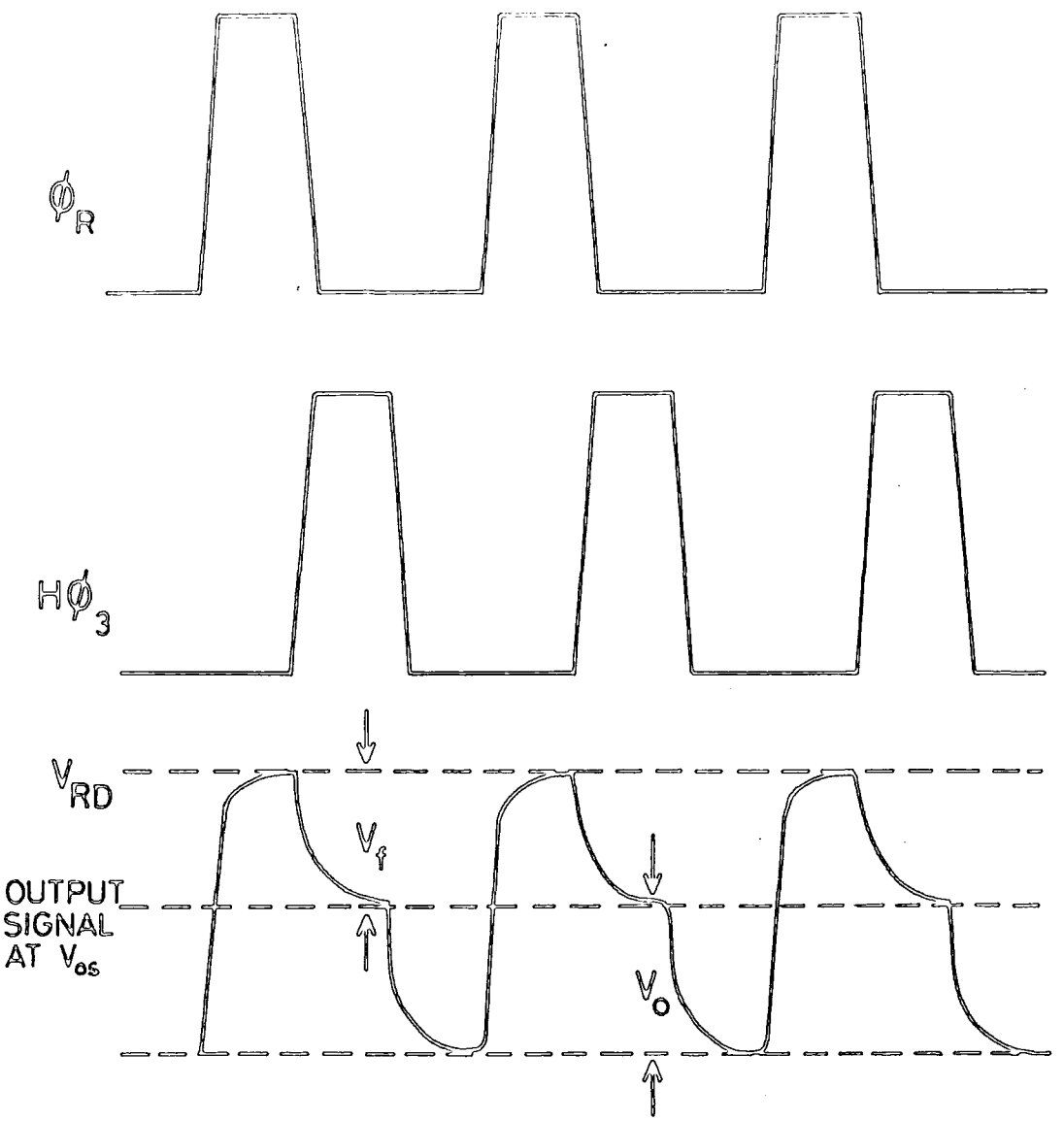

FIG. 2·10 SHOWING RESET FEEDTHROUGH, V_f

feedthrough problems and also reducing reset noise. In this operation the 'dummy' output is not used. The operation of this technique will be described later in this chapter.

2.2.4 Requirement and Measurement of Calibration of the Output Circuit. The relationship between signal levels at the output circuit can be written as follows:

$$V_o = V_{os}/G \tag{2.1}$$

and

$$q_o = C_o V_o \tag{2.2}$$

where V_o is the signal voltage on the output node,

V_{os} is the signal output at OS,

G is the voltage gain of the source follower stage,

q_o is the signal charge on the output node, and

C_o is the output node capacitance.

From the above equations, it can be seen that all measurements taken at the output, OS were referred back to the CCD output node, either as a voltage at the node or as a charge on the node. Therefore, direct calibration of the output circuit is necessary in order to directly compare different devices and different circuit configurations and is also useful for any quantitative application of the device. Calibration of the output circuit can be done by measuring the voltage gain of the source follower stage or the total capacitance associated with the output node, C_o. In the present system the signal charge at the output node is measured in terms of voltage, therefore the gain of the output transistor T_2 must be measured for calibration.

The gain of the output transistor T_2 is measured using

the following procedure: firstly, all the clock drive pulses are stopped, while the reset pulse, ϕ_R is held 'high' such that the reset transistor, T_1 is permanently 'on'. Then by varying the voltage V_{RD} on the reset transistor T_1, the corresponding voltage at the output source V_{OS} is measured. The gain of the output transistor is determined from this equation.

$$G = \frac{\text{The voltage at the output source } (V_{os})}{\text{The voltage at the reset drain } (V_{RD})} \qquad (2.3)$$

The results of this measurement are plotted in Figure 2.11. The gain G is given by the slope of the graph as 0.54 (using a 4K7 load resistor). In the above measurement the transistor T_2 is operated in the saturated part of its characteristic curve. Operating under this condition achieves the maximum gain and lowest noise of the device.

2.3 Measurement of Photoresponse

In order to reduce dark current and allow for long integration times to be performed without saturating the output, it is necessary to operate the device under cooled conditions. Operating the device at low temperatures may cause the device to function incorrectly through the behaviour of the carriers in the semiconductor. At very low temperatures (say < 40K) the carriers in the semiconductor may undergo "freeze-out" i.e. the semiconductor starts behaving as an insulator. Therefore, the performance of the device will be severely affected. Furthermore, the signal output of the device will be affected by cooling because the signal charge collected in the potential well contains charge contributed

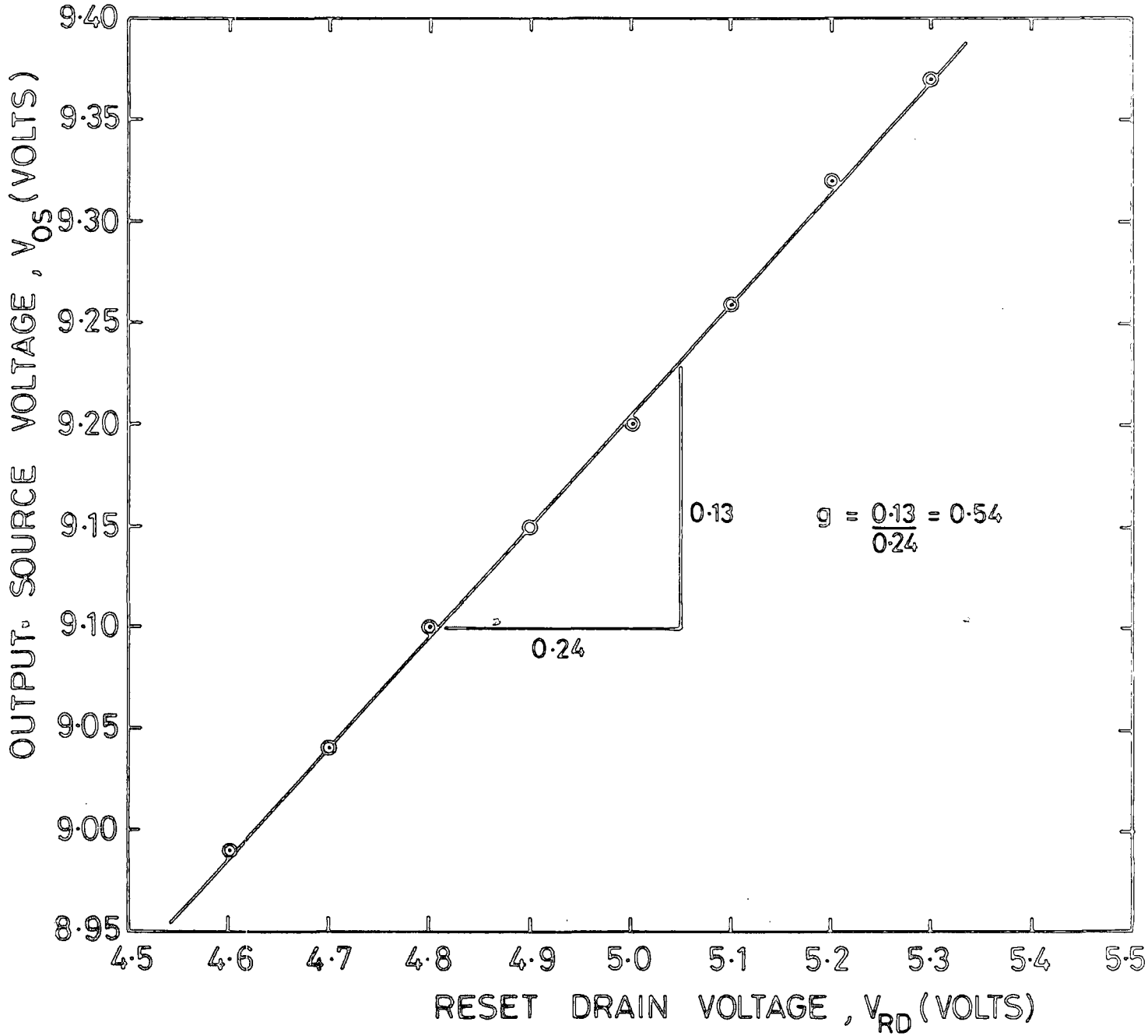
OUTPUT SOURCE VOLTAGE , V_{OS} (VOLTS)
9·40
9·35
9·30
9·25
9·20
9·15
9·10
9·05
9·00
8·95
4·5
4·6
4·7
4·8
4·9
5·0
5·1
5·2
5·3
5·4
5·5
RESET DRAIN VOLTAGE , V_{RD} (VOLTS)
0·13
0·24
$g = \frac{0·13}{0·24} = 0·54$

FIG. 2·11

by dark current. Therefore, it is necessary to check the performance of the device under cooled conditions. This can be done by looking at the response of the device to different light intensities. Measurements of the photoresponse were conducted in the laboratory using a light source together with a set of neutral density filters, to provide different light intensities incident upon the image section of the CCD at fixed integration times. A graph of signal,integrated in a fixed integration time, against relative filter transmission is plotted as shown in Figure 2.12. The graph shows that the device responds linearly with signal. In the above measurement the device is operated at a temperature of approximately -150°C (or 123K).

2.4 Noise Considerations of the Device for Astronomical Work

There are three major sources of noise associated with the CCD for imaging applications particularly in Astronomy; the electronic noise introduced by the CCD output circuit, Poisson counting noise caused by the finite number of photoelectrons detected by each pixel and, fixed pattern noise caused by dark current. From previous discussion of the operation of the CCD output circuit, it can be said that there are two main sources of noise associated with the CCD output circuit. They are the KTC noise associated with resetting the output node capacitance C_o, commonly called reset noise, and the thermal or Johnson-Nyquist noise in the output transistor T_2. All the above noise sources will be considered in this section.

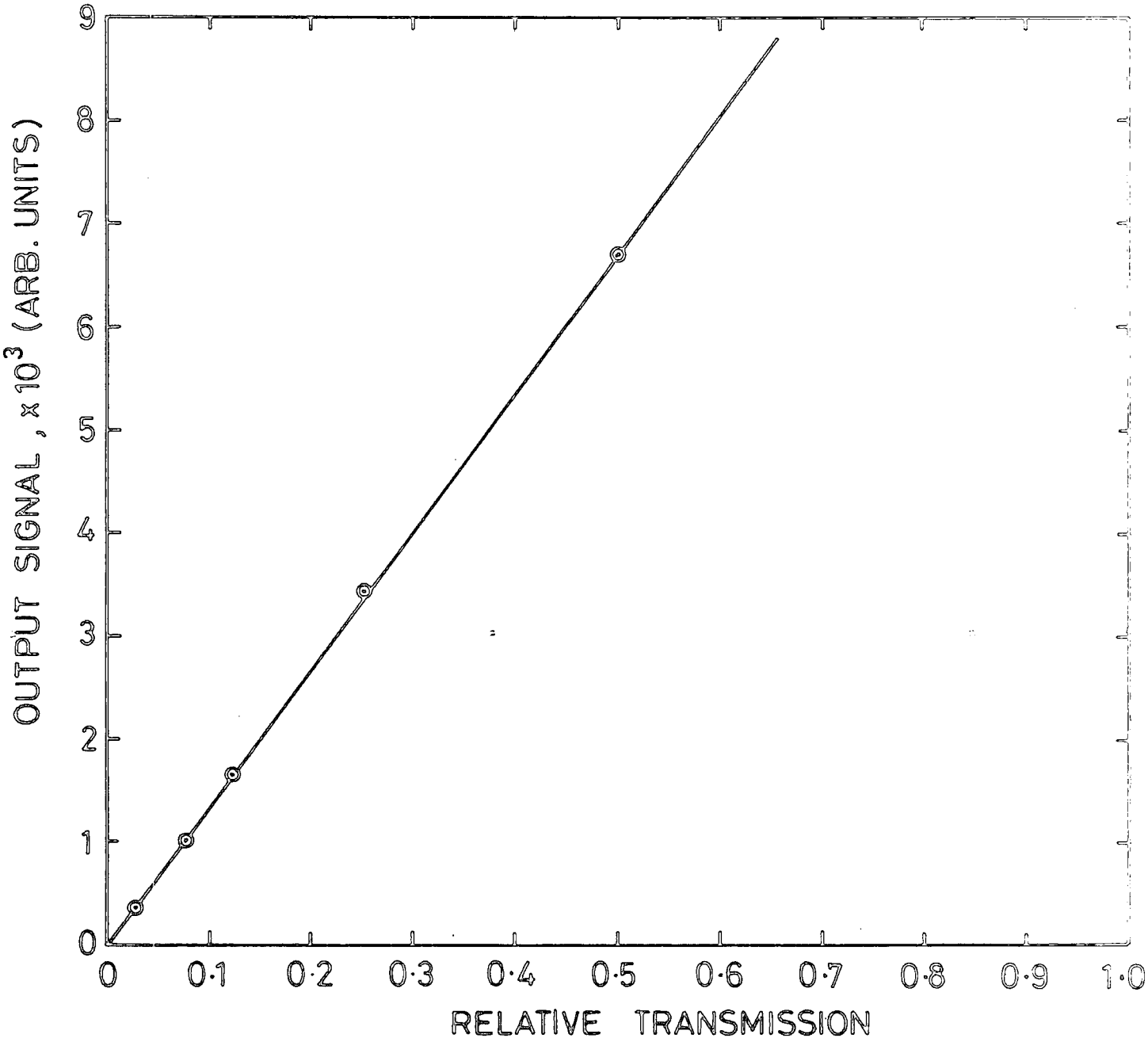
OUTPUT SIGNAL , x 10^3 (ARB. UNITS)
0
1
2
3
4
5
6
7
8
9
0
0·1
0·2
0·3
0·4
0·5
0·6
0·7
0·8
0·9
1·0
RELATIVE TRANSMISSION

FIG. 2·12

2.4.1 Reset Noise

This noise is introduced through the process of resetting the output node before charge is transferred to the node. In this process, when the reset pulse ϕ_R goes 'high', the reset transistor (MOSFET) T_1 turns 'on' and consequently the output node is reset to the potential V_{RD} (reset drain, see Figure 2.4). However, there is some uncertainty, V_{rms} in this voltage owing to thermal noise present in the reset transistor T_1. This uncertainty may be expressed as the total root-mean-square noise voltage present on the output node and given by (8).

$$V_{rms} = \left[kT / C \right]^{1/2} \qquad (2.4)$$

Equation 2.4 can also be represented by this equation (9)

$$n_{rms} = \frac{1}{q} (kTC)^{1/2} \approx 400 \left[CpF \right]^{1/2} \qquad (2.5)$$

This equation represents the uncertainty in number of charges (or electrons) on the output node,

where K is the Boltzmann constant,

T is the temperature of the system,

C is the output node capacitance, and

q is the charge on the electrons.

This noise voltage is present on the output node at the instant the reset transistor T_1 turns-off. Therefore, the output node will assume a mean d.c. voltage V_{RD} with the noise voltage superimposed on it. Similarly, on the next reset cycle, the output node will be reset again, but to a different voltage comprised of the d.c. voltage V_{RD} plus whatever noise

voltage was present at the time of turn-off and so on. It is these random fluctuations in the voltage to which the output node is reset that form reset noise.

Fortunately, this reset noise is constant during the read out of a pixel. Hence, reset noise can be reduced by taking the difference between the capacitor voltage before and after signal charge is deposited. This will result in an improvement of the system read-out noise.

2.4.2 Output Transistor Noise. The output transistor T_2 incorporated on the device is a MOSFET type. Naturally, it should be expected that associated with this kind of transistor will be thermal noise, $^1/f$ noise, and generation-recombination noise (10). However, the performance of this device shows that the noise associated with transistor T_2 is essentially $^1/f$ in character at low frequencies and decreases to a white noise floor at MHz frequencies. This was demonstrated by General Electric Company as illustrated in Figure 2.13. This behaviour may be explained as follows: the device is operated under cooled conditions, so the thermal noise in the transistor should be reduced, furthermore, the thermal noise may also be reduced by operating the transistor with a high drain voltage. Operating the transistor at a high drain voltage will also result in increasing the generation-recombination noise, while the $^1/f$ noise is practically constant (11). Since the generation-recombination noise is due to random emission of electrons and holes at the defect centers in the depletion region of the semiconductor, it may be reduced through careful fabrication of the device.

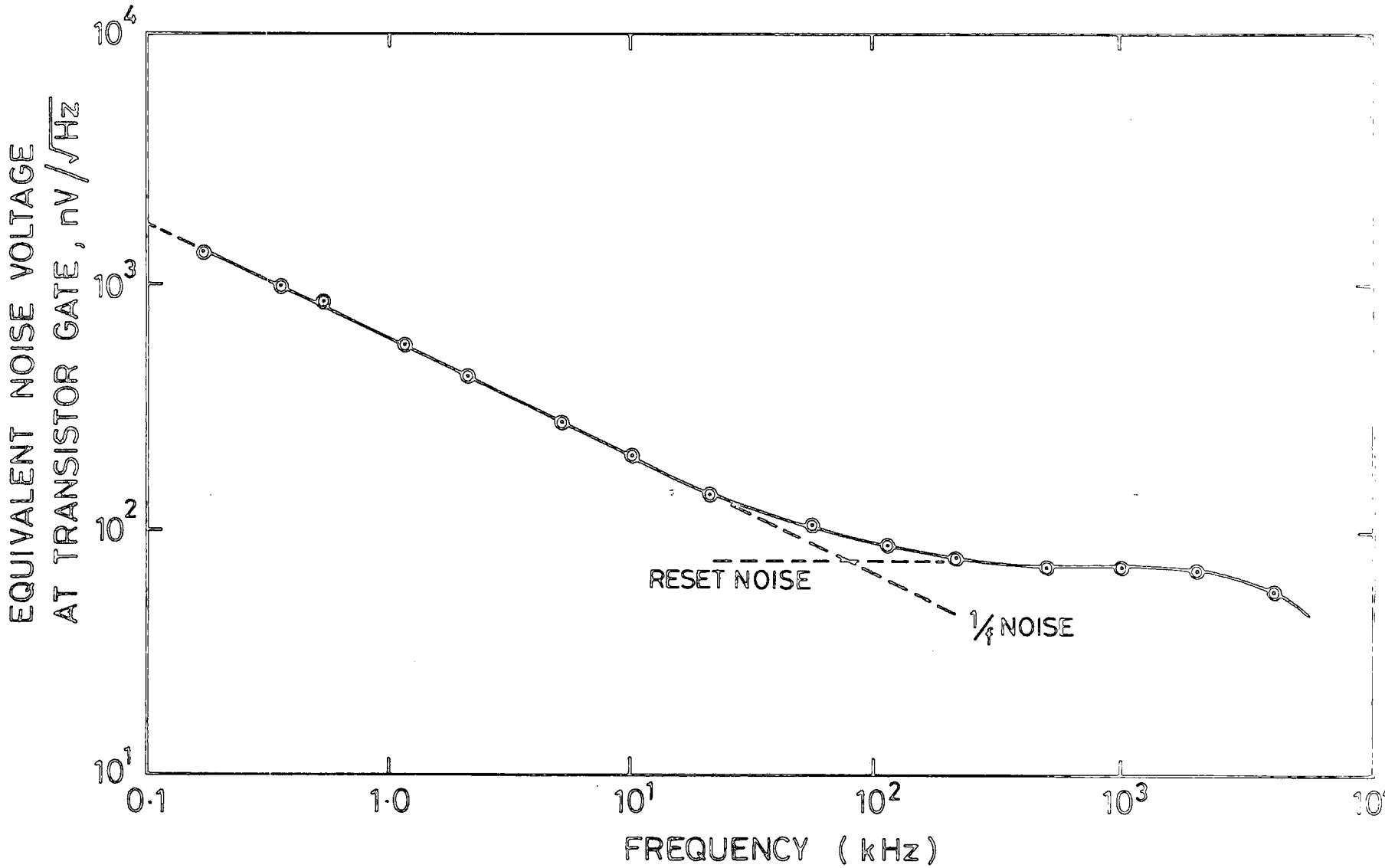

FIG. 2·13 NOISE SPECTRUM

Moreover, at higher frequencies this noise is negligible compared to the reset noise. Therefore, the dominant source of noise in the transistor will be the $^{1}/f$ noise.

The $^{1}/f$ noise is the surface noise at the oxide-semiconductor interface which is caused by the surface states present in the interface. This $^{1}/f$ noise can therefore be reduced by operating the transistor in a 'buried channel' mode where the current conduction takes place entirely in the bulk of the silicon and thus away from the noise inducing trapping states at the oxide-semiconductor interface.

2.4.3 Photon Noise. The signal charge collected on each pixel is produced by the incident flux of photons. There are also other processes in the device such as the recombination-generation process (12) which contribute to the signal charge collected on each pixel. However, their contribution to the signal charge is very small as compared to the incident flux of photons. Ideally, each photon absorbed in the silicon bulk will generate a minority carrier, which is then collected in the nearest potential well. If the same fixed fraction of signal charge is always collected, the device will show perfect linearity up to the limit given by the saturation of the potential well. In practice, the signal charge collected in the potential well in a fixed time does change. This is to be expected because of the emission of photons from any source is a random process. Therefore, the number of photoelectrons collected in a potential well in a time interval, t is a random variable. The standard deviation of

this random variable is represented as the photon noise. For example, a potential well is occupied by signal charge denoted by N_S and the photon noise is given as the square root of N_S, i.e. $(N_S)^{\frac{1}{2}}$. The other noise components associated with the signal charge can be added as the square root of the sum of the squares to obtain the resultant signal-to-noise ratio in the output circuit of the device.

2.4.4 Fixed Pattern Noise. Dark current or leakage current is produced in the device through the thermal generation of electrons that accumulate in the elements or pixels of the CCD thereby adding directly to the photogenerated signal. Theoretically speaking, the dark signal should be uniform and does not significantly affect the overall performance of the device since it would add equally to the outputs from all elements or pixels. In practice, there will be variations of dark current from one element to the next because of the inhomogeneities in device manufacture. This variation of dark current from one element to the next and so on will have a major effect in determining the dynamic range of the device particularly at the low end. As this variation is equivalent to a pattern of photogenerated charge, it is known as fixed pattern noise. This fixed pattern noise tends to set a minimum signal level below which the output signal is considered as noise.

There are also other types of fixed pattern noise present in the CCD i.e. arising from variations in sensitivity from one element to the next and from geometric irregularities in clock lines or in channel stop diffusions.

2.5 Dynamic Range of Devices

The range of signal levels over which a device gives useful output is called the dynamic range. The dynamic range of the CCD is limited at the high end by the peak charge handling capability and at the low end by the noise, particularly the fixed pattern noise. Therefore, the output dynamic range of CCD may be given as

$$D = Q_p/qn_T \text{ peak rms} \qquad (2.6)$$

where Q_p is the peak signal charge per pixel,

q is the electronic charge, and

n_T is the total noise charge associated with the CCD. In most practical applications at room temperatures the limit to small signal operation will be determined, most probably, by the fixed-pattern noise associated with dark current non-uniformity, rather than thermal noise in the output circuit of the CCD, and a lower effective dynamic range may result. Therefore, in order to achieve the maximum dynamic range of the CCD, the dark current in the device must be reduced. This is achieved by cooling the device to low temperatures.

2.6 The Spectral Response and Quantum Efficiency

The device is intended for front-face imaging. When light is incident at the front-face of the device, it can be absorbed, transmitted or reflected by the semi-transparent polysilicon electrode structure. The absorption and transmission of photons by the polysilicon electrodes is dependent on the energy of the incident photons, i.e. wavelength dependent. If the photons have wavelengths greater than the

thickness of the polysilicon electrodes, they are most likely to be transmitted through the electrode layer and generate an electron (plus hole) that is captured by a potential well thereby contributing to the signal output. However, if the wavelengths of the photons are less than or approximately equal to the thickness of the polysilicon electrodes, then they are likely to be absorbed by the electrode material, and thus not contribute to the output signal. The reflection process takes place due to the presence of various interfaces on the chip, e.g. the three-level polysilicon electrodes, thus forming interference on the chip.

All the above processes contribute to the spectral response curve of the device. A typical response curve of the device is shown in Figure 2.14. Figure 2.14 shows that the device has a poor response towards the blue end of the spectrum. This is because in the case of the G.E.C. front illuminated chip, photons with shorter wavelengths are being absorbed in the polysilicon electrode structure. There are also slight ripples in the spectral response curve, because of interference effects at the polysilicon electrode layers which cause ripples to be superimposed on the spectral response curve with the position of the peaks and troughs dependent on the thickness of the polysilicon.

A measure of the light-to-charge conversion process is known as 'quantum efficiency'. If for every incident photon, an electron hole pair is generated and detected by the device, then the device is said to have a 100 per cent quantum efficiency. Since only a fraction of the light

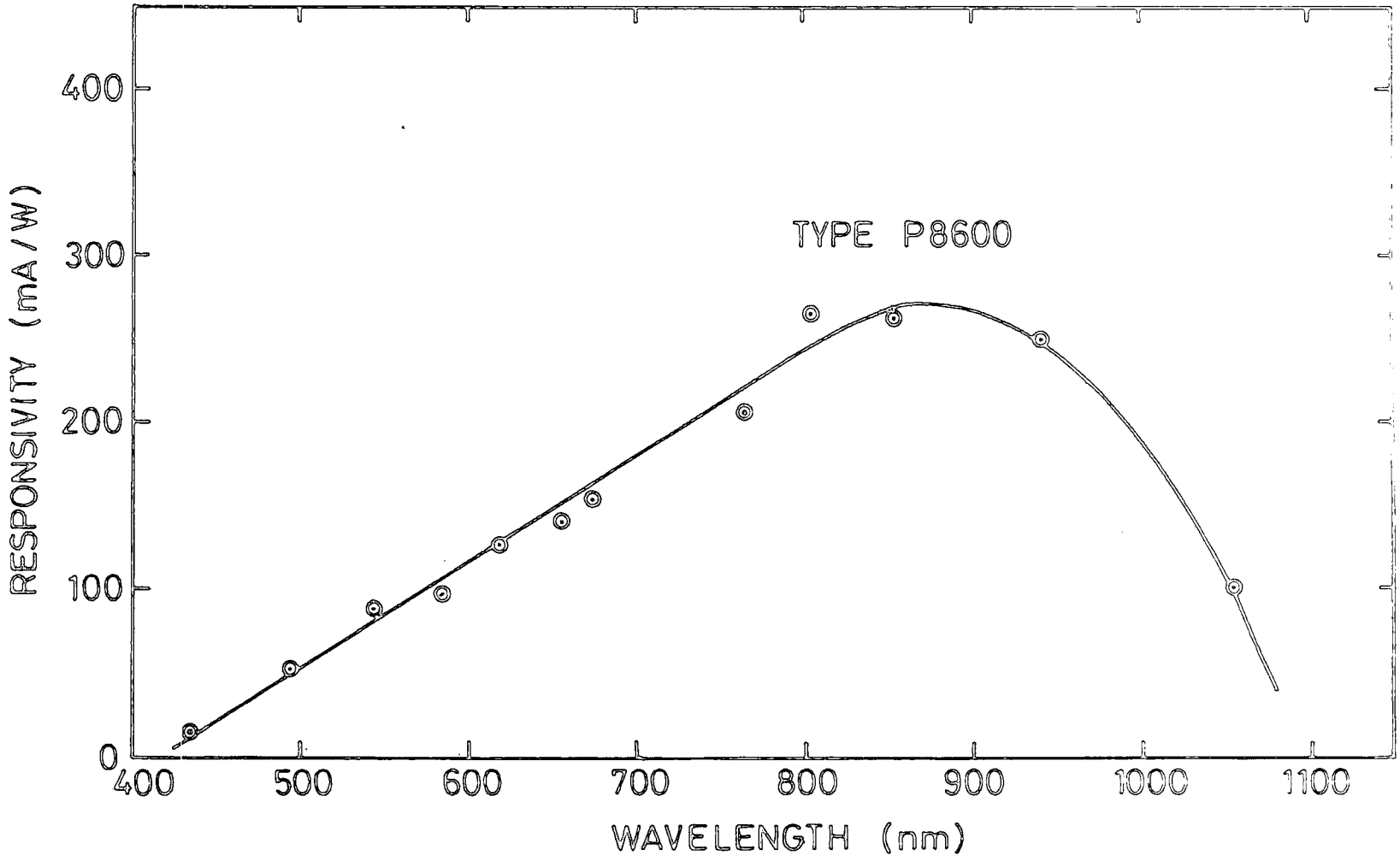

FIG. 2·14 SPECTRAL RESPONSE

incident on the front face of the CCD will actually penetrate to the substrate and generate electron hole pairs which will contribute to the signal output, the quantum efficiency of the device will therefore be lower than the ideal case. Furthermore, the photons with longer wavelengths (near IR) may generate electron hole pairs too deep in the silicon for collection in the potential well. This results in loss of response at the red end of the spectrum range as well as reduction in quantum efficiency. The mean quantum efficiency of this device is given as 25 per cent.

2.7 Resolution

One of the most important parameters of an image sensor is its spatial resolution, i.e. the ability to discriminate between closely spaced points in the image. A simple approach to assess resolution is in terms of the spatial frequency of an image focussed on the CCD and the modulation transfer function (MTF) of the output. Using Fourier theory, an image is Fourier analysed into periodic intensity variations. The spatial frequency of these Fourier components is normally expressed in black-white bar pairs per mm, where one black-white bar pair is the spacing between maximum of intensity as illustrated in Figure 2.15. The distance between the electrodes may also be expressed as a spatial frequency f_o (i.e. pixels per mm) and the spatial frequency f_i of the image focussed onto the CCD may be normalised as the ratio f_i/f_o. For example if f_i = 220 Hz and $f_o = \frac{1}{22}$ Hz (the CCD interelectrode spacing), then the normalised spatial frequency is given as $\frac{1}{22}/220$. Therefore the resolution

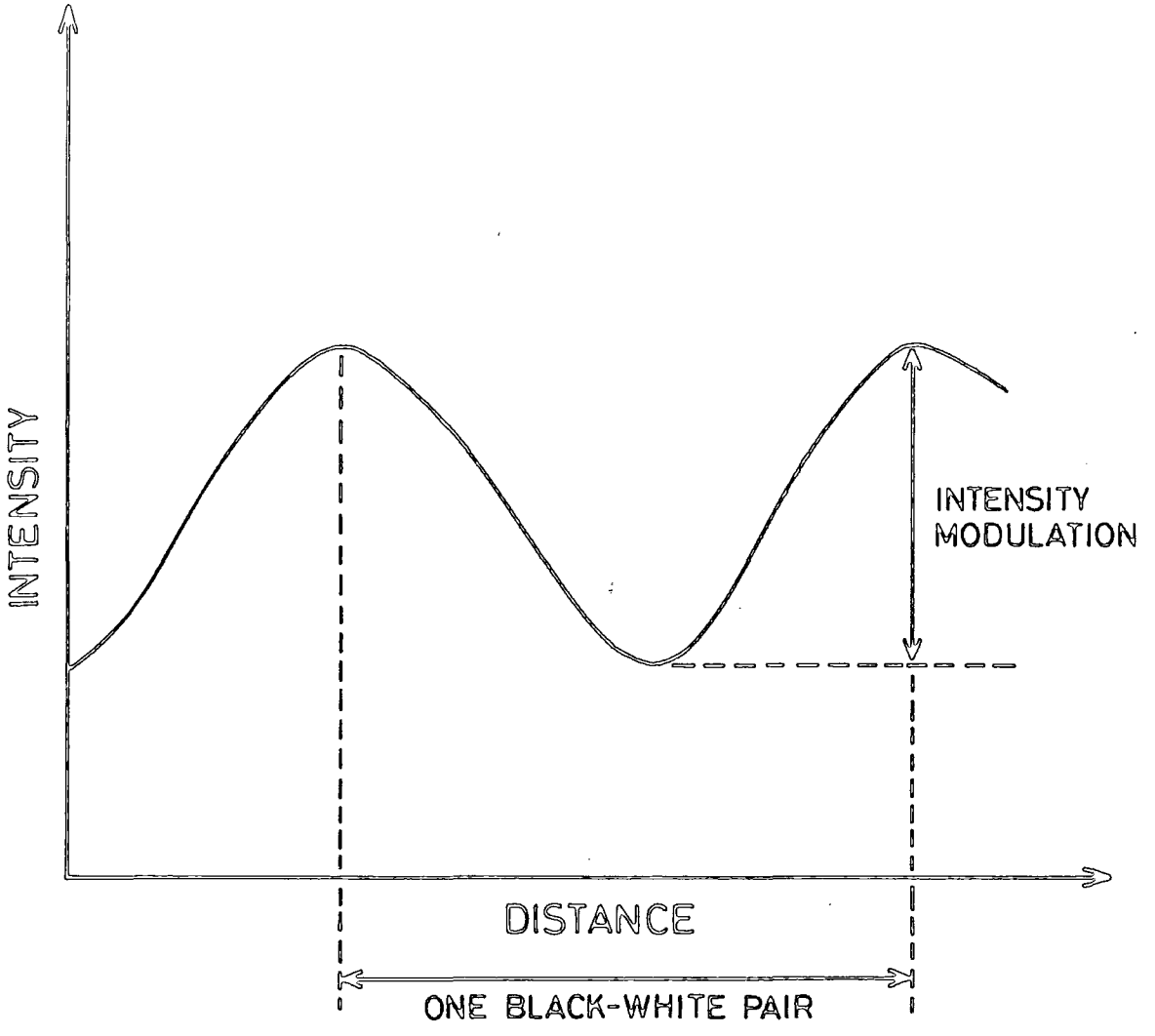
INTENSITY
INTENSITY
MODULATION
DISTANCE
ONE BLACK-WHITE PAIR

FIG. 2·15

is limited ultimately by the spacing of the resolution pixels to a normalized spatial frequency of

$$f_{i\,max} = \frac{f_o}{2} \qquad (2.7)$$

known from sampling theory as the Nyquist limit, i.e. at least two resolution pixels are required to image one black-white bar pair.

A curve of theoretical resolution expressed as the modulation transfer function (MTF) for a sinusoidal bar-pattern incident on the device is shown in Figure 2.16. In practice the device resolution is typically close to the theoretical at wavelengths up to about 800 nm. At longer wavelengths the photons penetrate deeper into the silicon before generating electrons, and there may be an appreciable lateral spread before these are collected as signal. This causes a reduction in the modulation transfer function (MTF). Resolution can also be degraded by 'inefficient' charge transfer. It is a fundamental limitation of CCDs that although charge is not lost, a small proportion of the charge signal is 'left behind' at each transfer. This residual charge adds to the next charge signal following through the array, which itself leaves a little behind and so on. This process can be expressed as the equation given below (12).

$$MTF' = (MTF)\exp\left[-n\varepsilon\left\{1-\cos\left(2\pi f_i/f_o\right)\right\}\right] \qquad (2.8)$$

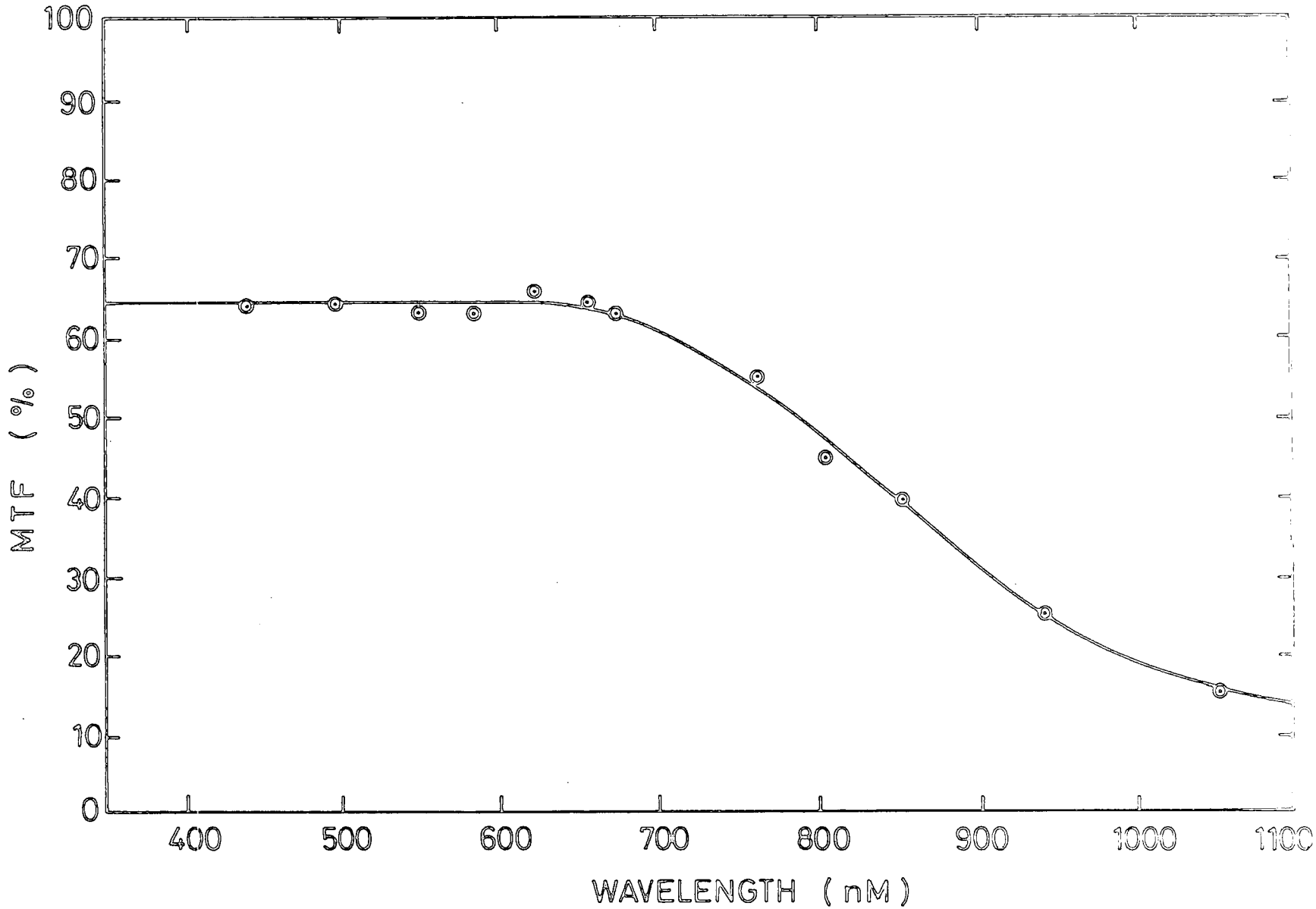

FIG. 2 16 MTF AT NYQUIST LIMIT AS A FUNCTION OF WAVELENGTH

where n is the number of charge transfer has taken place,

$\mathbb{E}$ is the transfer inefficiency,

f_i is the spatial resolution of image, and

f_o is the spatial resolution of pixel.

From the above equation, it can be seen that the modulation transfer function (MTF') is degraded by the exponential term. Therefore, there will be degradation in modulation transfer function for both the vertical (image section) and horizontal (read-out section) registers. However, this effect will be small in a buried channel charge-coupled device because its charge transfer inefficiency $\mathbb{E}$ has a very low value (10^{-5}).

It has been noted earlier, that the resolution is ultimately limited by the pixel size of the device. Therefore, to get the best resolution from this device, it is required that the highest spatial frequency content of a spectrum has a value equal to one half pixel size of the device (i.e. $f_i = \frac{1}{2f_o}$).

2.8 Blooming

As mentioned earlier, if there is a localised overload on the CCD, then once the potential well of a picture element is filled to its saturation level further minority carriers will spread sideways into adjacent picture elements. The localised overload will therefore spread over the CCD in proportion to the magnitude of the overload and the phenomenon is known as blooming. Blooming is subjectively unpleasant in that a localised overload may white-out a large proportion of an array with a resultant loss of information.

There are various techniques used for the suppression of this type of blooming. However, the basic principle applied to provide antiblooming for CCD's is that excess carriers are soaked away as they overflow from a picture element to prevent them spreading sideways. This is done by placing special overflow drains (13) in the form of reversed biased diodes or other conductive areas, between the integration sites, thus achieving complete blooming suppression.

The charge coupled device provided by G.E.C. makes use of diffused drain structures in place of channel stops in the image section for controlling blooming. The biasing and controlling of this effect is done through the MOS gates V_{ABD} and V_{ABG} (see Figure 2.5).

2.9 Cosmic Rays

Ionising radiation incident on the CCD generates electron hole pairs in the same manner as those produced by light. As cosmic rays possess much higher energies than light, they should give rise to spurious signals on the CCD. When the device is operated at low temperatures for dark exposure measurement these spurious signals have been observed on the video monitor as white patches of irregular shape. They are randomly distributed over the whole array.

When the bulk substrate version of the CCD was used the cosmic rays were detected at an average of one in every 3 seconds. Later, using the epitaxial substrate version of CCD it was found that the number of cosmic rays detected was considerably less. This is because the active thickness of

the sensor is reduced in the epitaxial device, therefore stray signals picked up through cosmic ray interaction.

2.10 Defects in CCD Arrays

Since the CCD is made from semiconductor material as the medium for photon detection, there may be several types of localised defects present on the chip. If a localised defect is present in one element then it can prevent all the subsequent elements in the line from working. Furthermore, a localised defect present in the read-out register can prevent many complete lines from working. Theoretically, it is unlikely that such defects will be introduced after device manufacture. In practice, there is always a possibility that defects will be introduced, because of the complicated fabrication process. At present it is generally difficult to obtain a chip which is 100 per cent free from defects. However, the problem of localised defects in the CCD array does not pose any difficulty for our astronomical work because only the good part of the CCD need be used.

2.11 Summary

The basic operation and performance limitations of charge-coupled devices, based on the requirements of optical imaging, have been described in the preceding sections. It may be concluded that CCDs makes a practical detector for low light level imaging applications. This is due to their promise of good linearity, high dynamic range, high quantum efficiency, low system noise and good overall system stability. It has also been shown that they can be operated at low temperatures (- 150°C) without affecting their performance.

Cooling ensures the maximum dynamic range of the CCD can be utilised through the reduction of dark current in the device. Furthermore, the basic operation of the CCD which requires external driving electronics and signal processing circuitry makes it attractive for application in astronomical spectroscopy. The main problem with the use of CCDs for astronomical spectroscopy is the restriction imposed by the non-uniformity of response from element to element when they are used in the integrating mode. Fortunately, this problem may be readily overcome by the flat-fielding method.

REFERENCES

1. Boyle, W.S., and Smith, G.E. (1971), "Charge Coupled Semiconductor Devices", Bell. Syst. Tech. Jour. 49, 587-593.

2. Bobeck, A.H. (1967), "Properties and Device Applications of Magnetic Domains in Orthoferrites", Bell. Syst. Tech. Jour. 46, 1901-1925.

3. Grove, A.S. (1967), Physics and Technology of Semiconductor Devices, Published by John Wiley and Sons Inc., p.278.

4. Barbe, D.F. (1975), "Imaging Devices Using the Charge-Coupled Concept", Proceeding I.E.E.E., Vol. 63, No. 1, 38-67.

5. Sequin, C.H., and Tompsett, M.F. (1975), "Charge Transfer Devices", Advances in Electronics and Electron Physics, Supplement 8, p.131-138, Academic Press Inc., New York, San Francisco, London.

6. Bertram, Jr., W.J., Sealar, D.A., Sequin, C.H., Tompsett, M.F., and Buckley, R.R. (1972), Intercon. Dig., p.292.

7. Lamb, D.R., and Beynon, J.D.E. (1977), "Technology and Limitations of Surface and Buried Channel CCDs", Application of Charge-Coupled Devices (Summer School Lecture notes), Department of Physics, Electronics and Electrical Engineering, UWIST, Cardiff.

8. Michon, G.J., and Burke, H.K. (1980), "CID Image Sensing", Topics in Applied Physics, Vol. 38, p.5-24.

9. Carnes, J.E., and Kosonocky, W.F. (1972), RCA Review, 33, 327.

10. Jordan, A.G., and Jordan, N.A. (1965), "Theory of Noise in Metal Oxide Semiconductor Devices", I.E.E.E. Trans. Electron Devices, Vol. ED-12, 148-156.

11. Sah, C.T., and Hielscher, F.H. (1966), "Evidence of the Origin of the $^{1}/f$ Noise", Phys. Rev. Letter, Vol. 17, 956-957.

12. Wu, S.Y. (1968), "Theory of Generation-Recombination Noise in MOS Transistors", Solid State Elec., 11, p. 25-32.

13. Sequin, C.H. (1972), "Blooming Suppression in Charge Coupled Area Imaging Devices", Bell Syst. Tech. Jour., 51, 1923-1926.

CHAPTER 3

THE CHARGE COUPLED DEVICE CAMERA AND COOLING SYSTEM

3. INTRODUCTION

The operation of the General Electric Company charge coupled device has been fully described in chapter two. It has been noted that external driving electronics circuitry is required to operate the CCD. The device should be operated under cooled condition, if it is intended for low light level applications, particularly in astronomical spectroscopy work. Cooling the device at low temperature can virtually eliminate dark current so that long charge collection times become practical for integration at very low photon flux. The signal charge present at the CCD output can then be read out with a suitably designed external signal sampling electronics circuitry to minimise noise associated with the charge detection process. Using techniques such as 'correlated double sampling' (CDS), the reset noise can be eliminated, with the result that the $^{1}/f$ noise from the output transistor becomes dominant. However, this noise can be minimized through operating the output transistor at its optimum conditions.

It is obvious that some form of control and read out system would have to be developed in order to apply the charge coupled device to optical imaging work. Design and development of a control and read out system for the G.E.C. charge coupled device was started immediately prior to the

proposal of the Faint Object Spectrograph project put forward to the Science Research Council by the group.

In this chapter, the modules designed and built for the charge coupled device camera system are described briefly in terms of their functions. A cooling system used for the charge coupled device will also be presented here.

3.1 The Requirements of the Present System

Normally for television type imaging applications, charge-coupled devices and other solid state imaging devices are being operated purely under hardware control, with analog signal processing and analog final output. However, in our applications, the requirements of the experiment dictate the use of a rather more complex operational system. Furthermore, the requirements are very different according to whether the charge-coupled device is to be used in the direct photon integration mode (1) or in the intensified photon counting mode (2).

In the present system the charge coupled device is used in the direct photon integration mode. The operating sequence employed to run the charge coupled device in the above mode has three stages: (i) a setting up period during which the charge coupled device is scan quickly 5 or 10 times in order to remove residual charges present in the image and read out sections prior to integration; (ii) an integration period for which the incident photon flux will generates photoelectron and being collected at the photosite of the array; and (iii) a final read out scan during which all the charges that have been collected at the photosite

are transferred into the line read out registers, and then each pixel is being read out using the correlated double sampling technique. This sequence of operation is accomplished by having a control system in which the control function is undertaken by computer software. In the system to be described the computer has complete control of the sequence of operation of the charge coupled device, functioning under interrupt control.

3.2 Charge Coupled Device Camera System

A block diagram of the complete system used to operate the CCD and to acquire, save, process and display data is shown schematically in Figure 3.1. The system is subdivided into three sections: (i) the camera head (cooling system and signal processing unit); (ii) the camera front-end electronics (control and timing pulses; and driving electronics for CCD); and (iii) the computer system interface to CAMAC, a modular interface system (to be described in the next section). With this configuration the development of hardware and software of the system can be implemented separately at the outset of the project. Detailed description of operation of the signal processing unit and the camera front-end electronics will be discussed more fully by Waltham (3), but briefly, the functions of each module will be outlined here. This is followed by detailed descriptions of operation of the modules located in the CAMAC crate.

The camera front-end electronics together with the

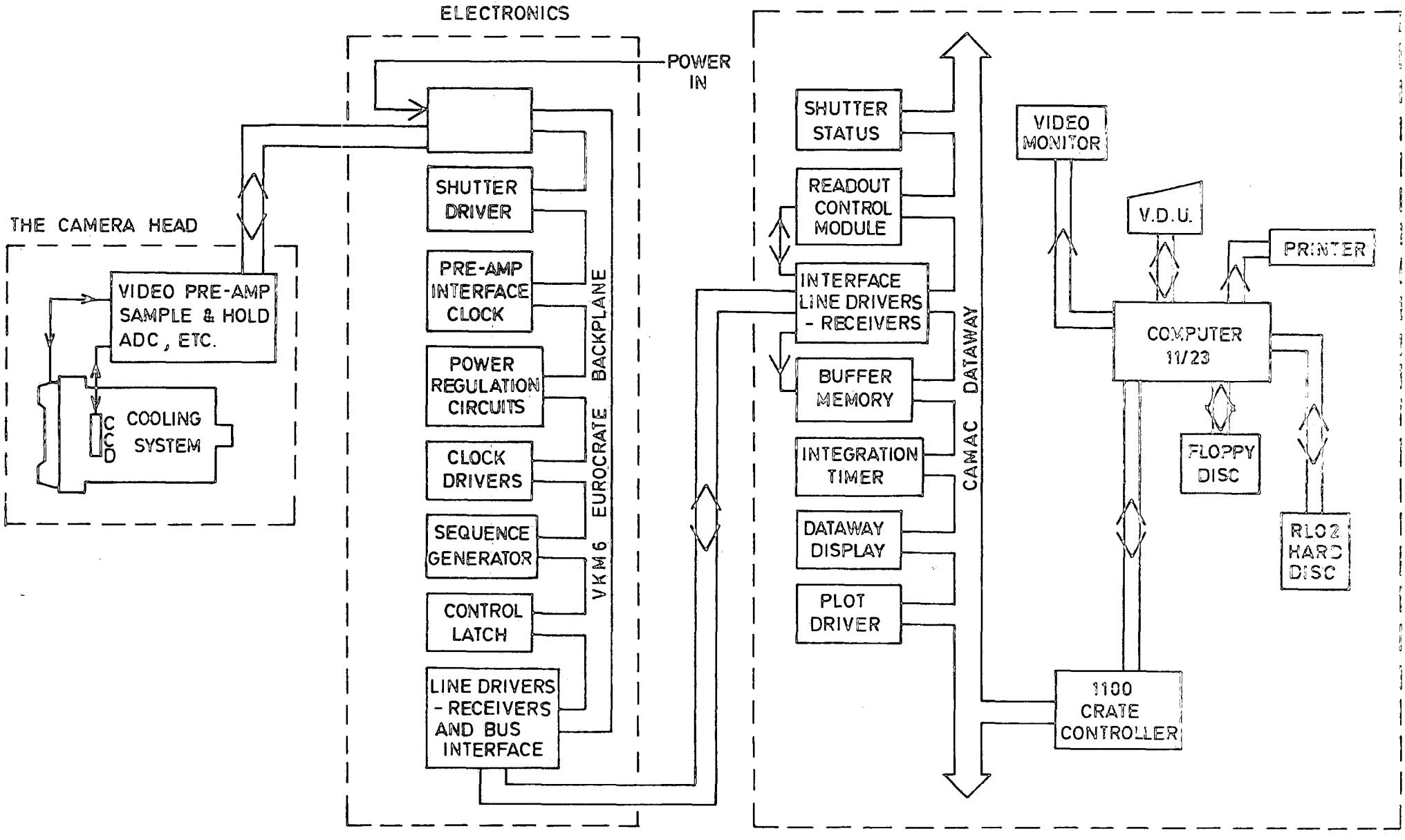

FIG. 3·1 A BLOCK DIAGRAM OF COMPLETE C.C.D. SYSTEM

camera head may form a "stand alone" hardware system, in which the signal waveform is observed by an oscilloscope with triggering derived from the "END-OF-PIXEL (EOP)" pulses produced in the SEQUENCE GENERATOR MODULE (SGM). The "heart" of this stand alone hardware system is the CONTROL LATCH MODULE (CLM). This module gates the clock pulses $V\phi_1$, $V\phi_2$, $V\phi_3$, $H\phi_1$, $H\phi_2$, $H\phi_3$ and ϕ_R to the charge-coupled device, and also the control pulses to the integrator (on the video preamplifier board), sample and hold, Analog to Digital Converter (ADC), electronic shutter and the buffer memory. The enabling and disabling of the above pulses are done by loading a control word (in the form of 16 bit number) into the control register of the CLM. The 16 bit control word defined to perform the necessary actions in the CCD camera system are tabulated in Table 3.1. For example, if bit 2 is loaded into the control register, then the vertical clocks $V\phi_1$, $V\phi_2$ and $V\phi_3$ are allowed to propagate through and thus cause a vertical charge transfer on the CCD. Similarly, other camera functions are controlled in this manner. In the stand alone hardware configurations the CLM is controlled by a module consisting of a set of 16 switches, which represents the 16 bit control word. A control word is determined through selecting the appropriate combinations of the 16 switches, if switch 1 is on and the rest are off, then bit 1 is loaded into the control register. Similarly if

TABLE 3.1

DEFINITION OF THE 16 BIT CONTROL WORD

No.	Control Word (Decimal)	Function
1	1	Enable interrupts
2	2	Enable the Vertical Clocks
3	4	Enable Memory Transfer
4	8	Alternate Memory Strobe
5	16	Power on
6	32	Enable the Horizontal Clocks
7	64	Read/Integrate
8	128	Invert
9	256	10 Vertical Clock Enable
10	512	Alternative Vertical Clock
11	1,024	Shutter Open
12	2,048	Shutter Close
13	4,096	
14	8,192	
15	16,384	
16	32,768	Bias Light

switch 2 is on and the rest are off, then bit 2 is loaded into the controlled register and so on.

For the CLM to be under complete computer control it has to work in conjunction with the readout control module (RCM) in the CAMAC crate. This RCM forms the heart of the camera controller. It contains a 16 bit storage register and the contents of this register defines the particular mode of operation of the camera. The RCM generates an interrupt to the computer once every line time just after the last pixel transfer (i.e. a line time is the duration of 400 pixel transfer clock). The interrupt pulse provided to the RCM is generated in the SGM. An interrupt routine in the control program then commands the RCM to load its current contents of storage register (comprises the 16 bit control word) to the control register of the CLM, which enables or disables the appropriate system pulses as required by the control program. This double latch system as shown schematically in Figure 3.2 is necessary for two reasons: firstly to make certain that the control word must not change in the middle of a frame; and secondly, the interrupt handling routine has one whole frame time, in which to decide upon and load the appropriate program status. Thus any type of integration cycle chosen can be implemented by the control program, which allows the operator maximum

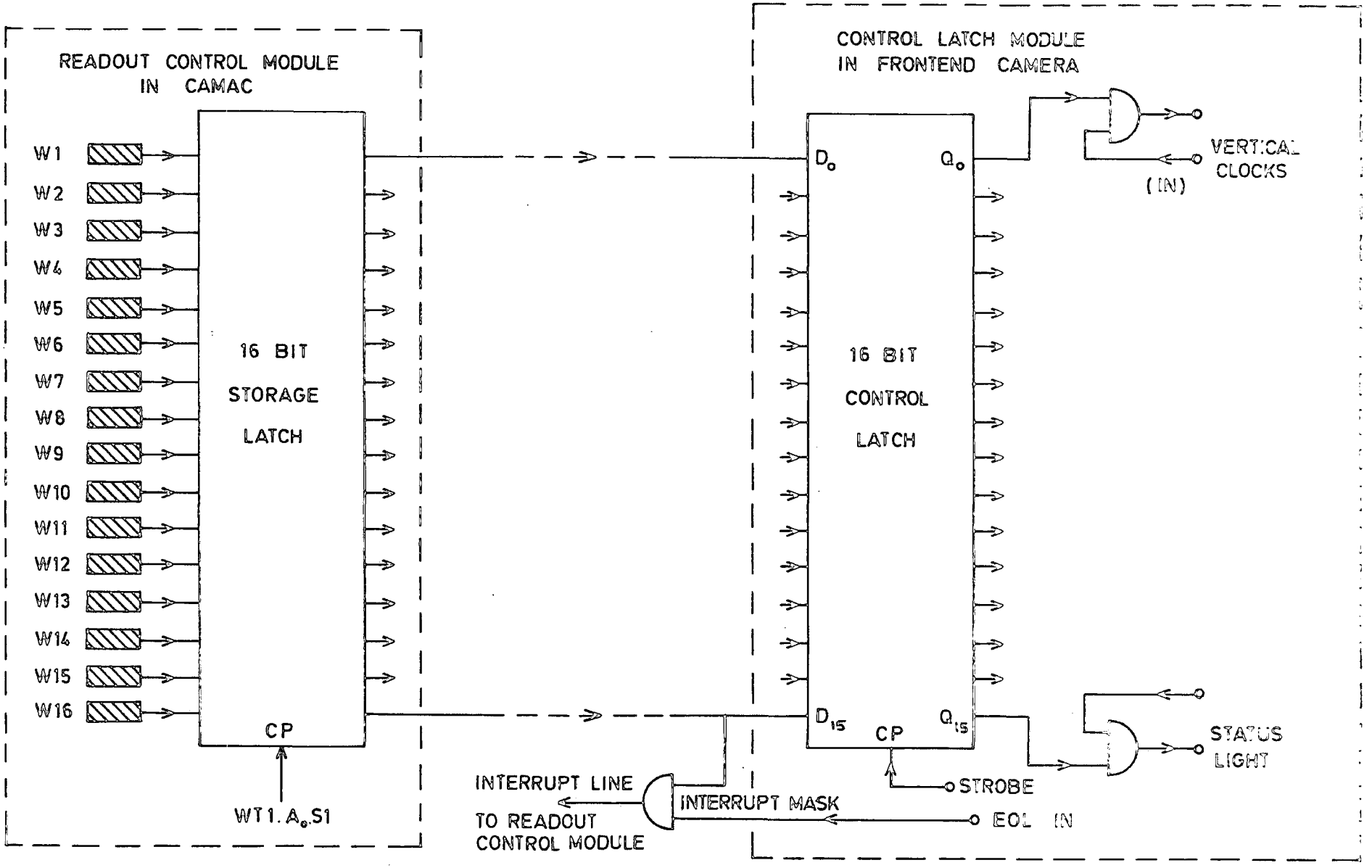

FIG. 3·2 DOUBLE LATCH SYSTEM

control over the operation of the system.

All the control and clock pulses required for operating the CCD camera system are provided at TTL level by the Sequence Generator Module (SGM). These pulses are produced in 3 Eproms. The drive pulses required by the CCD itself are converted from TTL to the required levels by the clock pulse drivers module. The required levels are adjustable from the potentiometer provided on the clock pulse drivers module.

The timing relationship of the control and clock pulses programmed in the 3 Eproms is shown in Figure 3.3, which illustrates one pixel readout of the CCD. The readout rate is 50 μs per pixel.

A video preamplifier, employing the 'dual slope integrator' mode, is used for sampling the signal at the CCD output. This method offers the versatility of simple changes of τ (the sampling time of the integrator) and $\Delta\tau$ (the delay between samples) to give good all round performance. The above mode is one of the schemes commonly used for the "correlated double sampling" techniques designed to remove reset noise and attenuates the $^1/f$ noise present at the CCD output circuit.

The signal sample at the output of the integrator is first being amplified (passing through an adjustable gain

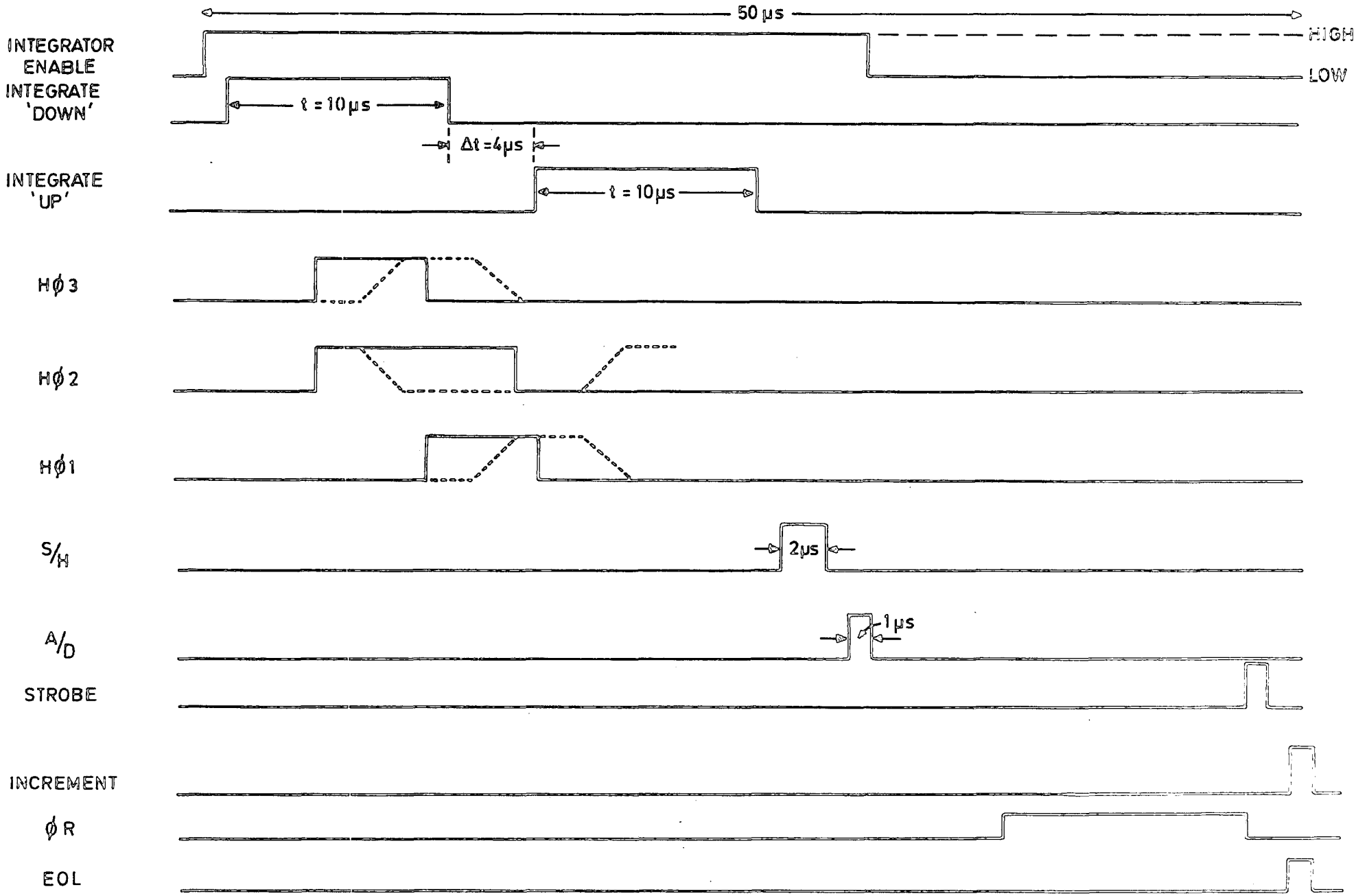

FIG 3·3 A PIXEL READOUT TIMING DIAGRAM

operational amplifier stage), before it is made available on hold for analog to digital conversion (and subsequent data storage) prior to resetting. This will give more efficient use of the ADC's resolution. An analogic MP 271 high speed precision sample and hold configured as non-inverting with unity gain follower during the sample mode, and followed by an inverting operational amplifier stage without adjustable gain during the hold mode, is used to match the video signal range to the ADC input requirements. The gain of the MP 271 quoted by manufacturers is typically within ± 300 μV of nominal 10V output. This small gain error may be compensated through the gain adjustment potentiometer on the analog-to-digital converter (ADC) following the sample-and-hold amplifier. Thus, an analogic MP 8014 (14 bit) ADC with a fast adjustable conversion times of 0.6 to 2.5 μs/bit is used for compatibility with the above sample-and-hold module. It is also chosen for its precise performance versatility in high resolution data acquisition applications at economical costs. The ADC module is configured as a low impedance direct input (having an input range of 0 to ± 10V) having parallel output with straight binary coding.

The power regulation circuits provide smooth regulated bias voltages as required by the CCD. The line drivers and receivers interface module is an optional module. It

would be necessary, when the CAMAC crate is situated at a long distance from the camera front-end electronics, such situation may arise at a telescope. However, in the laboratory work, this module would simply contain TTL buffers. The shutter driver module is used to drive an electronic shutter placed in front of the glass window of the cooling system. Its function is to blank the CCD during readout. The amplifier interface clock module provides the clocks required to operate the integrator in the dual slope integrator mode. The above system described has an overall system gain A = 100.

3.3 Introduction to CAMAC

CAMAC (4) is a modular instrumentation system adopted to computer control and acquisitions, originally developed to serve the requirements of the High Energy Physics community. CAMAC is adapted to most cases where data handling or transfer of instructions are required, generally at high speed.

CAMAC is based around a 19" rack and has up to 24 stations for plug-in units on a pitch of 17.2 mm. Each plug-in unit occupies one or more mounting stations in the crate. However, the extreme right hand station as viewed from the front of the crate is reserved for a controller module unit. At each station (i.e. normal station) there is an 86-way connector socket giving access to the CAMAC DATAWAY, a data highway which forms part of the crate. The DATAWAY consists

mainly of bus-lines for data, control and power. Thus, communications between plug-in units takes place through the Dataway. The data lines in the Dataway are accessible at the remaining normal stations, but not at the control station. Most signal lines are bus-lines connecting corresponding contacts of the Dataway connector sockets at all normal stations and, in some cases, the control station. There are also individual lines each linking one contact at a normal station to one contact at the control station. The two most important individual lines provided to the normal station, the "module address" (N); and the "module call", (LAM or "Look-at-me").

The control station is occupied by a module called the crate controller. A crate controller handles all DATAWAY operation in the CAMAC crate, e.g. operation of individual modules in the crate such as a read or write commands, etc. In our CAMAC crate system, the Hytec 1100 controller is used as the crate controller. It is a dedicated crate controller, which can be interfaced to the PDP11/23 backplane through the 1104 interface card. When the crate controller is interfaced to the computer, the Q-bus (of PDP11/23) is extended to crate controller which looks like extra memory configured between 28K - 30K by the computer. Therefore the modules in CAMAC can be read and written as the PDP11 memory (memory addresses) (5).

CAMAC has the ability to detect interrupts: in the CAMAC crate interrupts appear as LAM (Look-At-Me) signals on the DATAWAY. Each module has an individual LAM line connected directly to a register in the controller. The controller, typically looks for LAM's from the stations in cyclic order. On detecting a LAM request from a particular module the controller initiates an interrupt sequence in the PDP 11/23 putting an interrupt vector on the module producing the original LAM.

Each module in the normal station of CAMAC crate may be addressed by CAMAC commands. A CAMAC command, by convention is in the form of N.A.F.B. where

N is the location (station number) of the module in the crate,

A is the subaddress (register) inside a module selected by N,

F is the function which may be used to act on the selected address, and

B is a busy line indicating whether the Dataway is busy or not.

There are five function (F) and four subaddress (A) lines on the Dataway. These functions and subaddresses are binary coded, giving a total of 32 (coded) functions and 16 (coded) subaddresses which can be used to address a CAMAC module. These functions and subaddresses are defined in CAMAC document EUR 4100E.

A partial or full decoding of functions and subaddresses can be given to a CAMAC module. A partial decoding in a

module means not using all bits to define the function or subaddress entering the module. Whereas full decoding requires that all bits (5 for F, 4 for A) be used in the decoding process, even for one single function or single subaddress. The difference between partial decoding and full decoding is that in case of a wrong command, the module with partial decoding may execute the command, whilst the full decoding module would not execute it. CAMAC commands and sometimes data may be strobed with the strobing signals S1 or S2 provided in CAMAC. This avoids false triggering and false recording due to initial and final noise in the CAMAC command and data.

It is common practice that CAMAC users tend to design and construct their own modules by following closely the requirements and rules of the CAMAC specification. This way users can save costs and also the modules can be applied directly in the user system for the intended operation.

3.4 The Integration Timer Module

This module is used together with the Dataway Display module (to be described in the next section) to monitor the integration period. The function of this module is to measure the elapsed time of an exposure by counting interrupts produced within it, while the Dataway Display module indicates the time remaining for an integration.

The integration timer module is constructed as a CAMAC unit. A schematic diagram is given in Figure 3.4. It contains two status latches which may affect program operation. The first latch FF1 is a LAM latch set

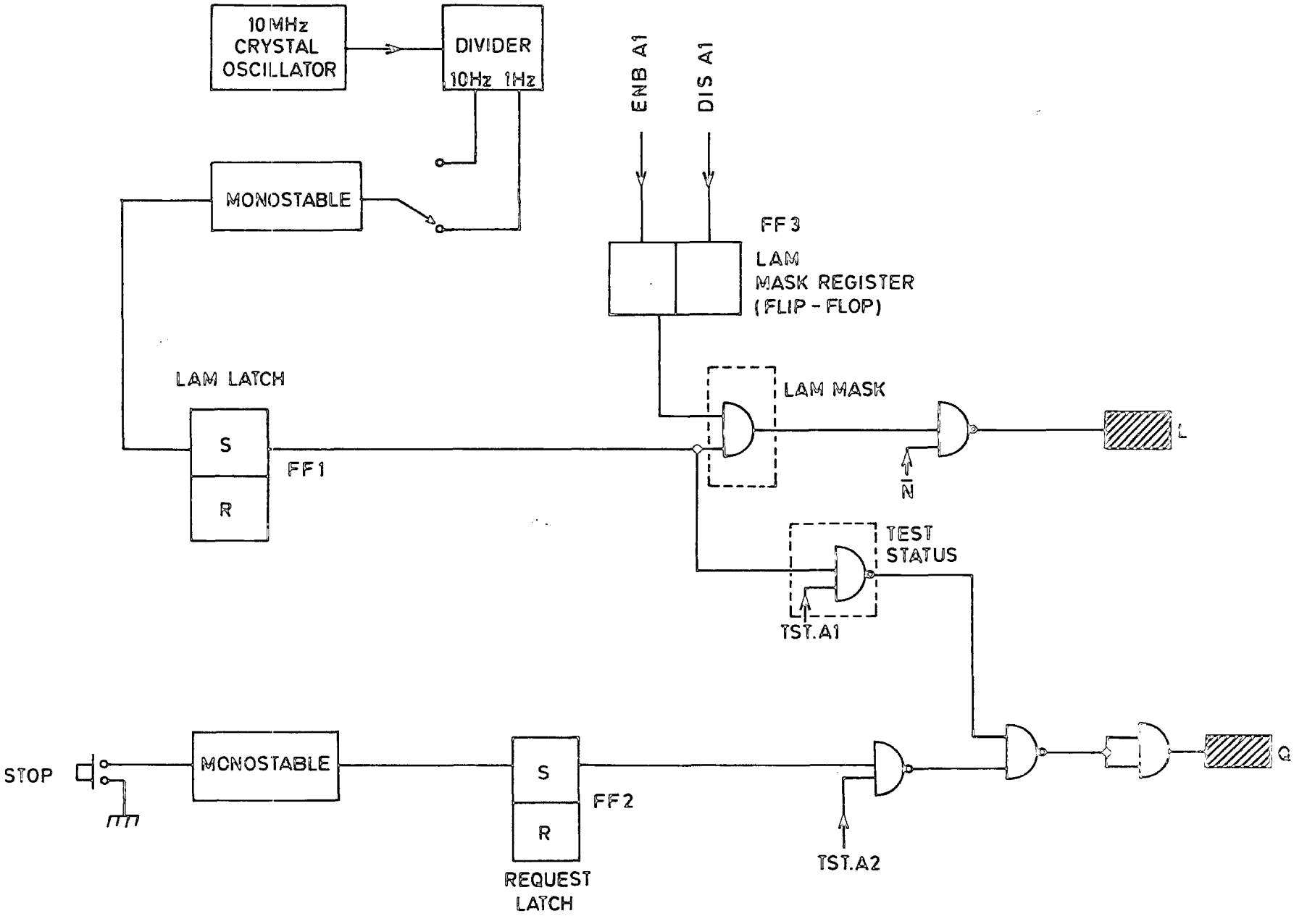

FIG. 3·4 THE INTEGRATION TIMER MODULE

periodically by pulses derived from a crystal clock. The output of FF1 may either produce a full LAM by asserting the L line on the Dataway or the status of the latch may simply be tested by sending a TST (test status command) to the appropriate subaddress within the module, thereby asserting the Q line on the Dataway. The ability of the module to cause a LAM and thus a computer interrupt if enabled or disabled by a LAM mask register, FF3. In accordance with the CAMAC specification (6) the L signal within the module is also gated with $\overline{N}$ (the complement of the station address line signal), in order that a LAM cannot be asserted by a module while it is being addressed.

The other status latch, FF2, is used to record an external event (in this case the operator pressing the stop request button) and its status may also be tested, again by a TST command, which produces a Q response if the latch is set. However, this function has no LAM capability.

The principle of operation of this module is outlined below. At the beginning of an exposure the LAM signal is enabled (i.e. the enable bit is set in the LAM mask register, allowing the LAM latch, FF1, if set to produce a L signal on the Dataway) by an ENB command from the acquisition program. Thereafter a LAM will be produced by the module at a rate determined by the crystal clock. This interrupt rate is switch selectable, from the front panel, as either 1Hz or 10Hz, the final signal being derived from a 10MHz master oscillator by division. The length of the resulting set pulse applied to the RS flip flop FF1 is determined by a monostable. A pulse width of 7μs is chosen such that the

flip-flop may be reset subsequently by a clear LAM (CLM) instruction from the computer. Thus every time the LAM latch is set an interrupt sequence is initiated in the interrupt program which decrements a counter variable used to record the duration of the exposure, tests the current value of the counter to see if any action is required and finally issues a command to reset the LAM latch, FF1. The program may check that the latch has in fact been reset by executing a Test Status (TST) command at the appropriate subaddress and looking for a Q response. Clearly, the computer must complete the interrupt sequence before the next LAM is set in the module or a clock signal may be missed. From experience it has been found that interrupt rates of $1Hz$ and $10Hz$ may be handled quite easily by the computer, allowing time for an interrupt routine to take any necessary action, e.g. set flags indicating to the main program that the predetermined exposure has been completed. Also within the interrupt routine the binary number of the unelapsed portion of the integration (units of 1 sec or $^1/10$ sec) is written to the CAMAC DATAWAY Display module, enabling the progress of the exposure to be seen.

The other status latch is provided to allow some external intervention by the operator (through a front panel push button). Typically, the status of this latch FF2 is tested periodically by the main program, and if a Q response is found the exposure is terminated prematurely. Thus any preprogrammed action may be allocated to this latch, which is set by hitting the front panel button, most commonly that of stopping the integration, i.e. commands will be

issued to mask further LAM signals and to begin a device readout sequence. A list of CAMAC commands used and actions performed in this module is tabulated in Table 3.2

3.5 The DATAWAY Display Module

The module to be described was built as a multipurpose test and development aid, combining the functions of a 24 bit output register, which can be both read and written over the CAMAC DATAWAY, and that of a visual, binary data display. The data, in the register may be accessed externally through a 25 pin D-connector on front panel and at the same time displayed by 24 red LEDs on the module. These LEDs are labelled 1-24, corresponding to the relevant read or write lines on the CAMAC DATAWAY. The usefulness of this module is found in the development stages of a program or other CAMAC hardware. If extra CAMAC write statements are inserted into a program the current value of various registers, counters etc. may be examined by the display module.

The module, a full schematic diagram of which is given in Figure 3.5, comprises 6 four bit latches to which data is written by a standard CAMAC WT1 command, the data being strobed into the latches at the time of S1 in the CAMAC cycle. A full function and subaddress decode is performed, subaddress zero being used for all commands understood by the module as listed in table 3.2. When a valid command is decoded the module automatically produces an X response on the CAMAC DATAWAY, a valuable self test feature. Since the DATAWAY is essentially an open collector bus normally pulled high by the crate controller,

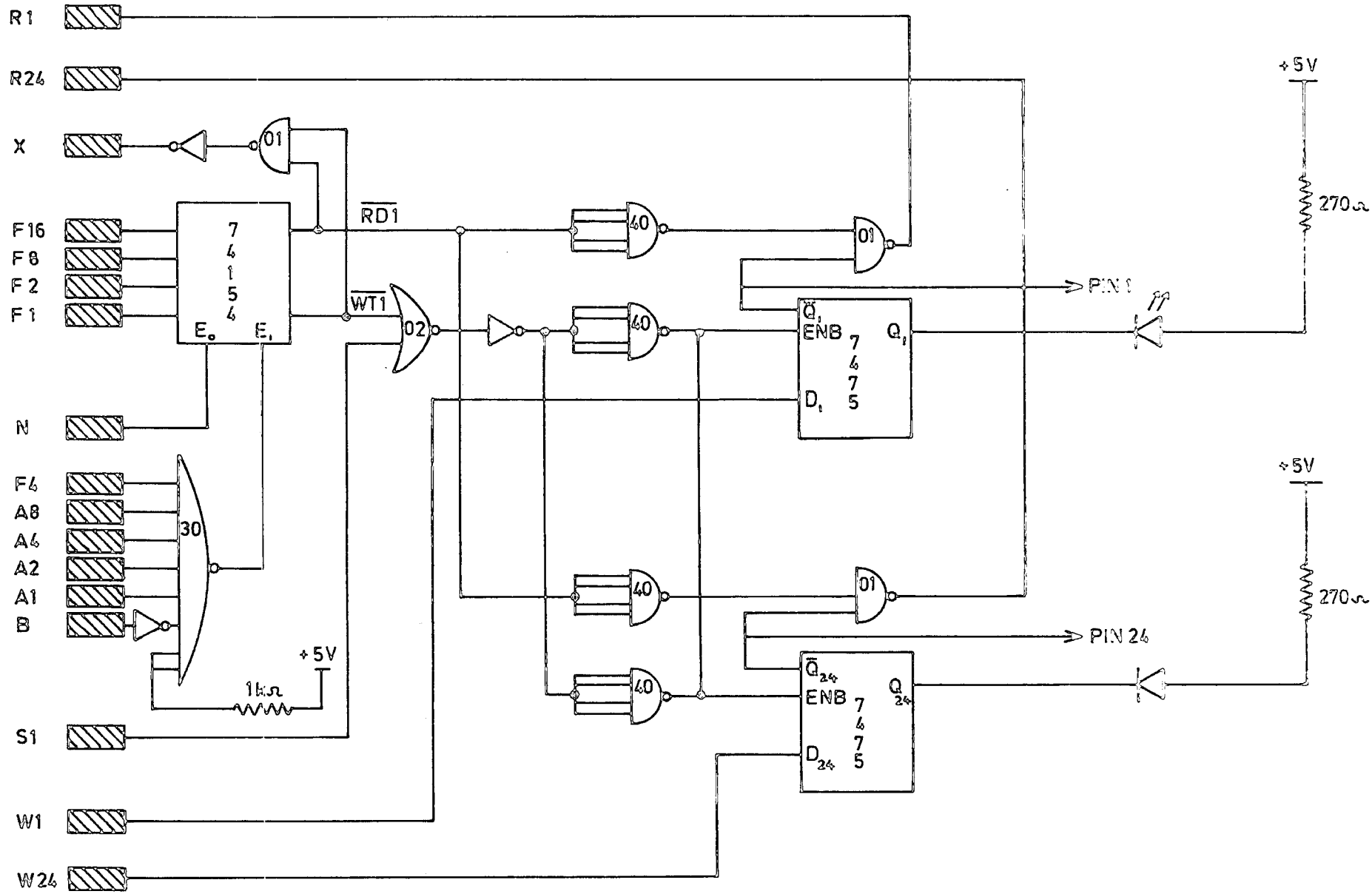

FIG. 3·5 THE DATAWAY DISPLAY MODULE

TABLE 3.2

INTEGRATION TIMER FUNCTIONS AND COMMANDS

CAMAC Commands	Action
F26.A1	Enable LAM Mask Register at Subaddress 1
F24.A1	Disable LAM Mask Register at Subaddress 1
F10.A0.S2 + F10.A2.S2 + Z.S2	Reset Request Latch at Subaddress 2
F27.A1	Test Status at Subaddress 1
F27.A1	Test Status at Subaddress 2
F10.A0.S2 + F10.A1.S2 + Z.S2	Reset LAM Latch at Subaddress 1
Z.S2	Initialise LAM Mask Register
S2	Clock LAM Mask Register

DATAWAY DISPLAY FUNCTIONS AND COMMANDS

CAMAC Commands	Action
F0.A0	Read Data
F16.S1	Write Data

OUTPUT LEVEL UNIT FUNCTIONS AND COMMANDS

CAMAC Commands	Action
F16.A0.S1	Write Data at Subaddress 0
F9.A0.S1+ Z.S2	Set (Clear) The Latches at Subaddress 0
F25.S1	Triggering Pulse

BUFFER MEMORY FUNCTIONS AND COMMANDS

CAMAC Commands	Action
F16.A0	Set Data In
F0.A0	Read Data
F9.A0.S1	Zero Address Counter
F16.A0.S1+Strobe (From Front Panel)	Set Data Out
F0.A0.S2+Increment (From Front Panel)	Increment Address Counter

data is sent to the modules in negative logic. For simplicity of design this logic sense is maintained within the modular latches, the $\overline{Q}$ outputs of the latches (7475) being taken to give a positive logic signal at the front panel connector. The LEDs, however, are wired with their anodes connected to + 5V and thus require a TTL low to be applied at their cathode connection in order to turn on. This requirement is therefore, met by the Q outputs of the latches, giving a conventional display (ON = 1, OFF = 0).

In the working system the display module is used as a visual integration countdown device as previously described, the time required for a CAMAC write operation to be achieved being fairly short (between 5-100 μs depending on the software used) and thus does not impose a large time overhead, as would writing to a serial device, e.g. the operator's console. A list of CAMAC commands used to operate this module is given in table 3.2.

3.6 The Output Level Unit (OLU) or Plot driver

This is a digital to analogue interface module which is useful for producing direct plots of digital data. This module shown in Figure 3.6 basically sends 8 bit digital data over the CAMAC write lines to an 8 bit buffer (D-type flip flop), strobed by WT1 . S1, the current contents of which drive a Digital-to-Analogue Converter (DAC08) producing a constant output level, which is maintained until the buffer is updated by further write commands. The original digital data is also available via a 15 way front panel D-type connector.

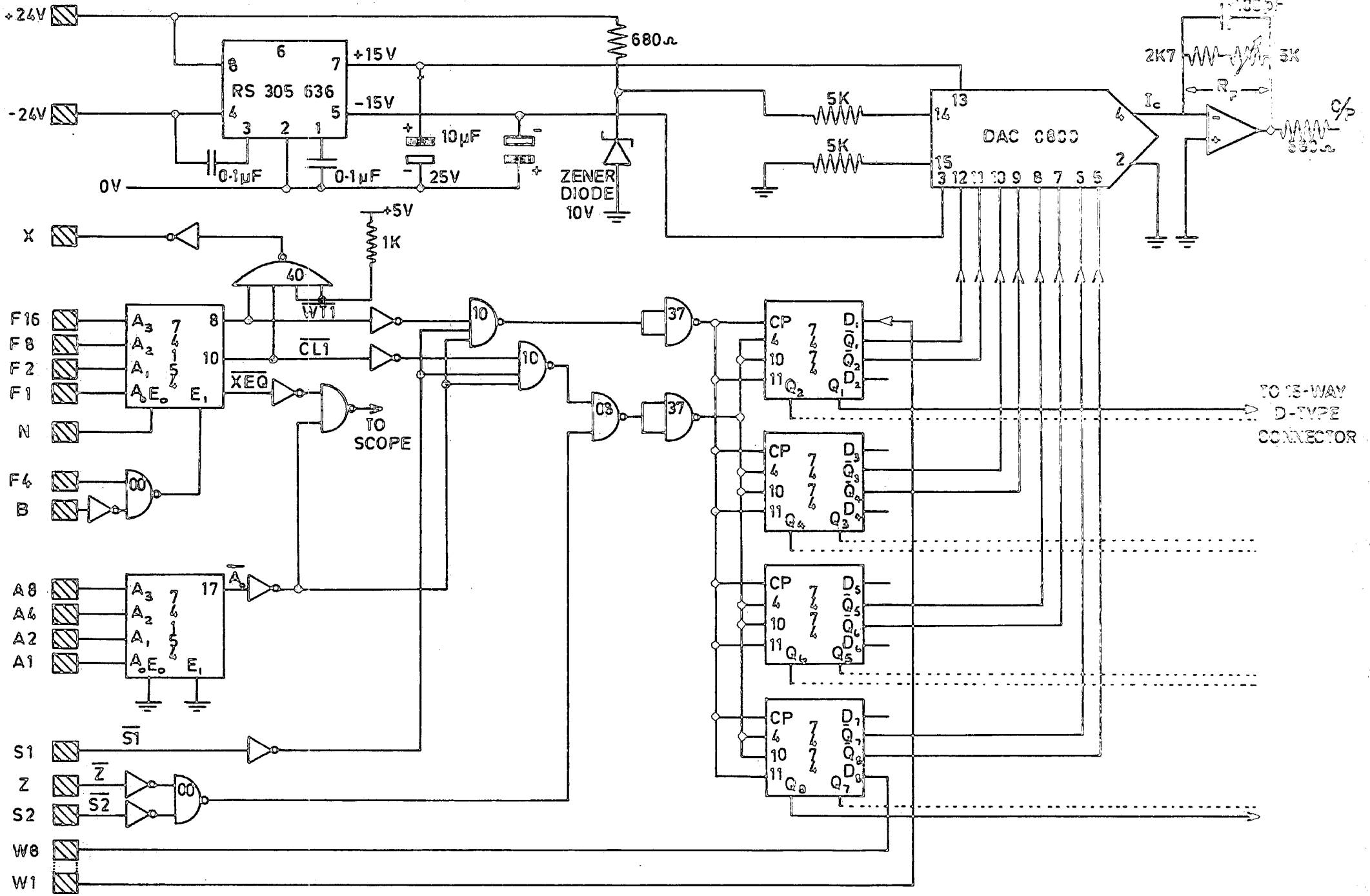

FIG. 3·6 THE OLU MODULE

The DAC08 is a monolithic 8 bit high speed current output digital-to-analogue converter. To convert the output current to a voltage output an operational amplifier is used. The operational amplifier not only converts current-to-voltage but also increases the output swing (i.e. provides gain) and lowers output impedance (load driving capability). The signal at the output of the DAC08 is inverted by the operational amplifier giving a real analogue signal.

In Figure 3.6, note that the outputs $\bar{Q}$'s of the 8 bit buffer are connected to the digital inputs of the DAC08, because data is sent to the 8 bit buffer in negative logic (CAMAC specification). The operation of the DAC08 is in the basic positive reference mode. The reference voltage (V_{REF}) of the DAC08 is supplied to the voltage across the zener diode. The voltage is approximately 10 volts. The output of the DAC08 is fed directly into the summing junction of an operational amplifier. The resulting low impedance voltage output being equal in magnitude to the product of the current, I_o and the resistance, R_F. The output of the operational amplifier can swing from 0 to 10 volts, adequate for driving a plotter. Notice also that a capacitor is connected in parallel to the feedback resistor to provide some low pass filtering. This is to prevent ringing or jittering and reduce DAC08 glitches due to spurious levels decoded at the time the data is changing. The power supplies needed to drive the DAC08 and the operational amplifier are provided by the dual voltage regulator (305-636). The inputs of this dual voltage regulator take ± 24 volts from

the CAMAC power line and produced ± 15 volts at its output.

This module makes use of only three CAMAC commands. These commands are write (WT1 or F(16)), clear (CL1 or F(9)) and execute (XEQ or F(25)). A full function decode is performed, subaddress zero being used for all commands (the command functions and actions are listed in Table 3.2). When a valid command is received the module automatically produces an X response on the CAMAC DATAWAY. A write command is used for transferring digital data from the CAMAC write lines to the buffer comprising four (7474) D-type latches. When a write command is issued, the data is strobed into the latches at the time of S1 in the CAMAC cycle. The latches may be asychronously set by a CAMAC clear command. If it is required to display the signal from the output of the operational amplifier on an oscilloscope, an accurate command is used to provide a front panel trigger signal for the oscilloscope.

3.6.1 Operation as a Graph Plotter Interface.

The simplest mode of operation, which is normally employed, is that of using the signal from the OLU as an input to a y-t chart recorder. This arrangement may produce direct plots of spectra by means of a simple computer program. The function of the program is to write stored data to the OLU at a precisely controlled rate which is chosen to suit the paper speed of the chart recorder. Thus the pen displacement is proportional to the current value of the 8 bit data word in the OLU buffer, this value being updated at regular intervals thereby constructing a graphical output. The necessary data are obtained by

truncating the original spectral data to 8 bits. A typical software routine is given in Figure 3.7. It is a list of Fortran program which writes data from an array to OLU at controlled time intervals.

This plotting facility has been found immensely useful for providing quick, hard copy outputs, allowing the quality of data to be assessed before more detailed analysis is undertaken on a larger computing system.

3.7 The Buffer Memory

The last module in the signal processing chain is the memory. Whilst it would have been possible to transfer the parallel data outputs from the DAC directly to the computer memory by a full handshake procedure through CAMAC, under processor control, it was decided that external buffer memory was preferable. This choice was made principally to simplify interrupt handling, as it is feared that the possibility of the computer missing words because it is occupied with internal tasks of higher priority.

A buffer memory has been constructed around static RAM chips (2102-2) as a CAMAC module as shown schematically in Figure 3.8. All the necessary control functions are implemented through the crate controller using the standard CAMAC functions. The buffer memory is capable of storing up to 1024 x 14 bit words. Initially, before the 14 bit data words are transferred into the memory, the address counter is reset or zeroed by a CAMAC F9 (Clear) command together with the strobe signal S1 in the CAMAC cycle. Loading the 14 bit data words from the ADC into the buffer

FIGURE 3.7

```
C     Program for 8 Bit DAC interface to Plotter.
      Integer * 2 VDAC.
      IBIT = 256
      Call Setna (VDAC, 7, 0).
10    Call XEQ (VDAC)
      DO 50 I = 1, 100
      DO 25 J = 1, 100
25    k = J
50    Continue
      DO 100 I = 1, 256, 8
      Call WT1 (VDAC, IBIT)
100   Continue
      IBIT = IBIT - 1
      IF (IBIT.EQ.-1) GO to 200
      GO to 10.
200   Stop
      End
```

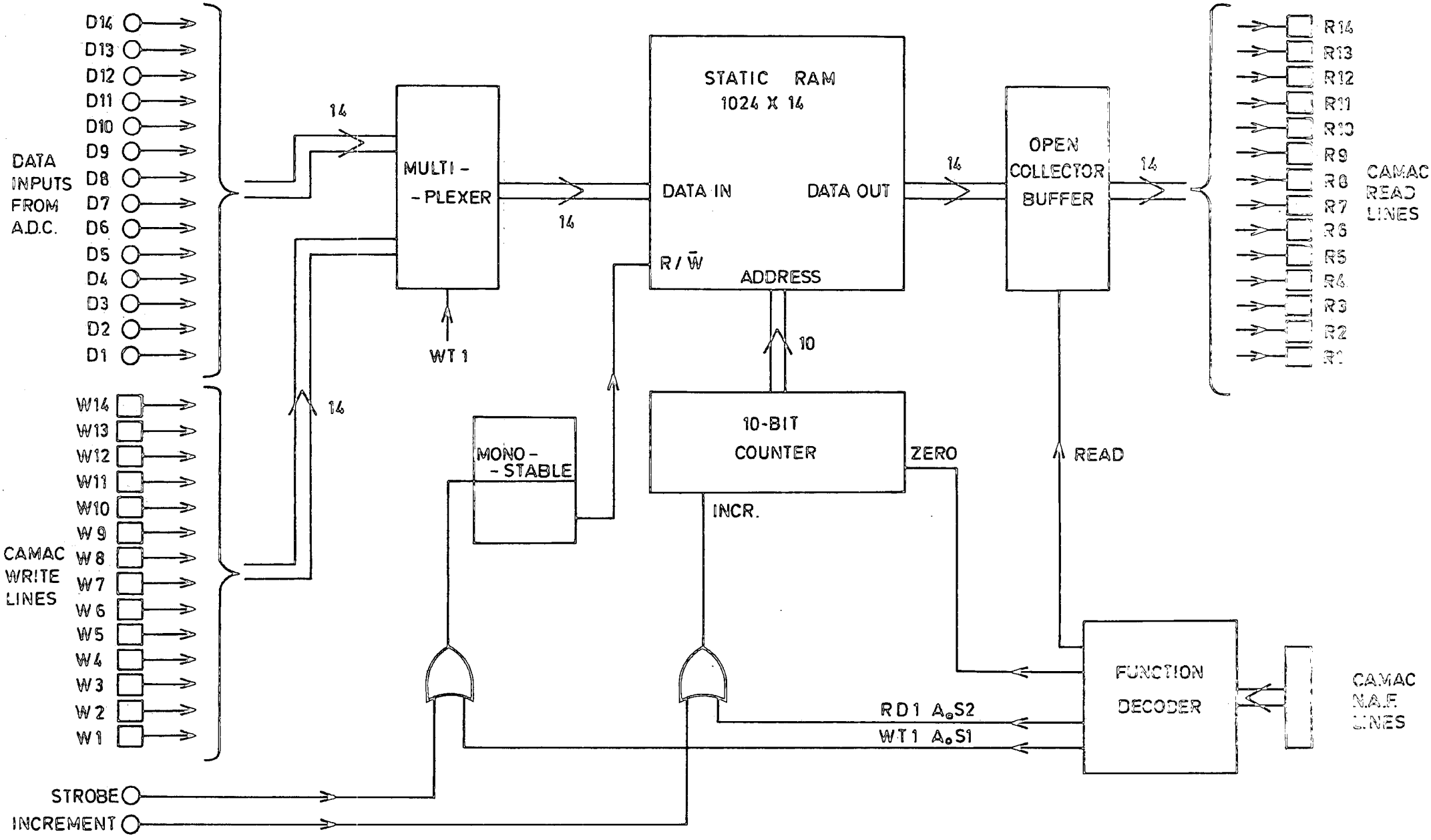

FIG. 3·8 THE BUFFER MEMORY

memory, via the front panel connector, is controlled by the control pulses, strobe and increment, which are produced from the sequence generator module. Synchronization of this transfer process can be achieved by gating the two control pulses with the Readout Control Module as described in the previous section, such that transferring begins with the first pixel or element of the line read-out of the CCD and finishes with the 400th pixel or element. The data in the buffer memory may be recovered by the computer, only when the memory address counter is reinitialized, and this is done under control of the data acquisition program . Once the memory address counter is initialized, the data in the buffer memory is read-out as well as being incremented during a CAMAC read cycle (RD1 command). The data are read-out into the crate controller dataway whereby the computer can get hold of the data. The buffer memory can be tested against memory faults by simply writing data into the buffer memory from the computer via a memory tester module, and reading back their data and compare with the original, will provide a quick check against memory faults. The above buffer memory module is later replaced by another buffer memory module using two 16k static RAM chips. This module will be described in detail by Waltham (3). A list of CAMAC commands used for operating the buffer memory is given in Table 3.2.

3.8 CAMAC Interface Line Drivers and Receivers

The possibility of requiring the CCD camera system to operate with its front-end electronics some distance from the CAMAC crate may arise, when conducting experiments at a telescope. To provide for this, a CAMAC interface module incorporating line drivers and receivers has been constructed to provide the driving capability needed for transferring the signals and data between the modules in the CAMAC crate and the front-end electronics. This ensures that the signals and data are not seriously attenuated as they propagate along the twisted pair cables.

This module comprises differential line drivers (DS 26 LS 31), line receivers (DS 26 LS 32) and opto-isolators (6N136). The opto-isolators are used to provide ground (i.e. earth) isolation between CAMAC crate and the camera front-end electronics. The supply voltage, + 5V required by the opto-isolators is provided by a + 5V "floating" power supply, i.e. the earth line on the power supply is disconnected.

3.9 Device Cooling

In chapter two it has been noted that the device is operated under cooled conditions in order to reduce dark current. This is necessary because of the variation of dark current with temperature follows the well known diode law (6),

$$I_D = A\exp^{-V_{BG}/(2kT/q)} \qquad (3.1)$$

where A is a constant,

V_{BG} is the bandgap of silicon,

k is the Boltzmann's constant,

T is the temperature, and

q is the electronic charge.

Clearly, the above equation shows that dark current is highly temperature dependent. Therefore, to achieve long charge collection or storage times, i.e. up to several hours, it is necessary to cool the device to a low temperature, thereby reducing dark current to a negligible level. As long as the temperature chosen for operation gives a dark current sufficiently low for the intended application, it would not be really necessary to control the ambient operating temperature precisely (unless it is required to stabilise the working point of d.c. coupled electronics against thermal drift in the output source voltage). However, the operating temperature chosen should not be too low (say < 40K) as this will cause the CCD to function incorrectly, owing to carrier freeze-out mechanisms (i.e. silicon starts behaving as an insulator).

It is now obvious that some form of cooling system is required for the device. A practical possibility of cooling the device is by conduction via a 'cold finger' to a liquid nitrogen reservoir. To prevent moisture condensing on the device some form of vacuum chamber is required. The cooling system will be described in the next section.

An important consequence of low temperature operation is reduced quantum efficiency, particularly at the longer

wavelengths. This is due to the light absorption properties of silicon as can be seen in Figure 3.9 which shows the silicon optical absorption coefficient, $\alpha(7)$ as a function of wavelength at room temperature (300k) and low temperature (77k). From these values of α , the quantum efficiency of the device (neglecting optical losses in the electrodes) as a function of wavelength $\eta(\lambda)$ can be calculated by using the equation below (8),

$$\eta_o(\lambda) = \frac{T_\lambda \left[1 - e^{-\alpha L_D}\right]}{\left[1 + \alpha L_o\right]} \qquad (3.2),$$

where T_λ is the electrode transmission,

α is the silicon optical absorption coefficient,

L_o is the electron (minority carrier) diffusion length, and

L_D is the depth of depletion layer (i.e. potential well).

3.10 Cooling System Design

A cooling system originally designed and used for the Plessey Photodiode array project has been modified in order to accommodate the CCD array. The modified version of the cooling system is shown schematically in Figure 3.10. The original design of the cooling system is an adaptation from a drawing of a cooling system used by the Royal Greenwich Observatory for an earlier CID project. The cooling system basically consists of a cylindrical liquid nitrogen vessel enclosed in a stainless steel vacuum container. This material is chosen for its relatively poor thermal conductivity and also its economical cost. The cylindrical wall of the

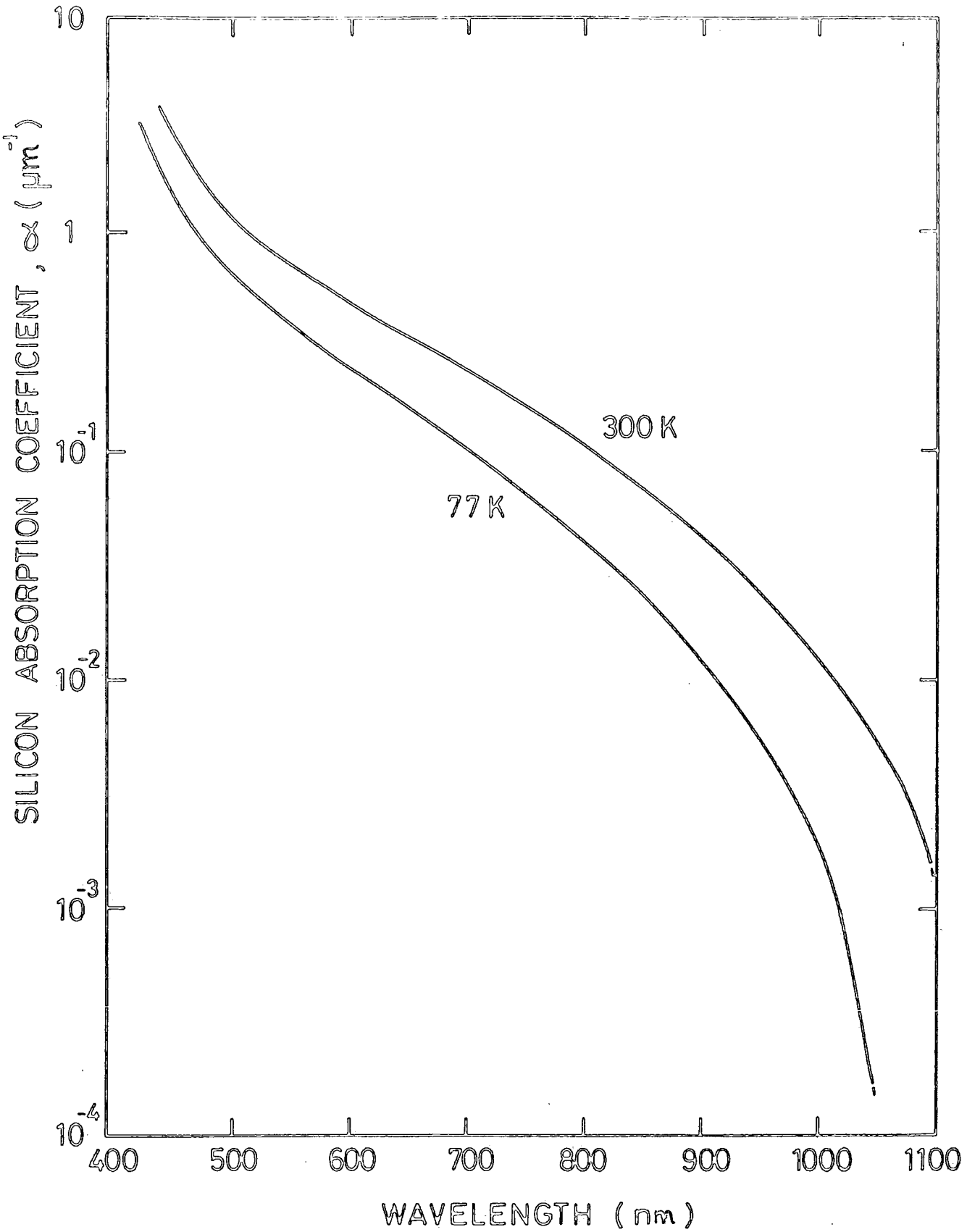

FIG. 3·9 SILICON ABSORPTION PROPERTIES

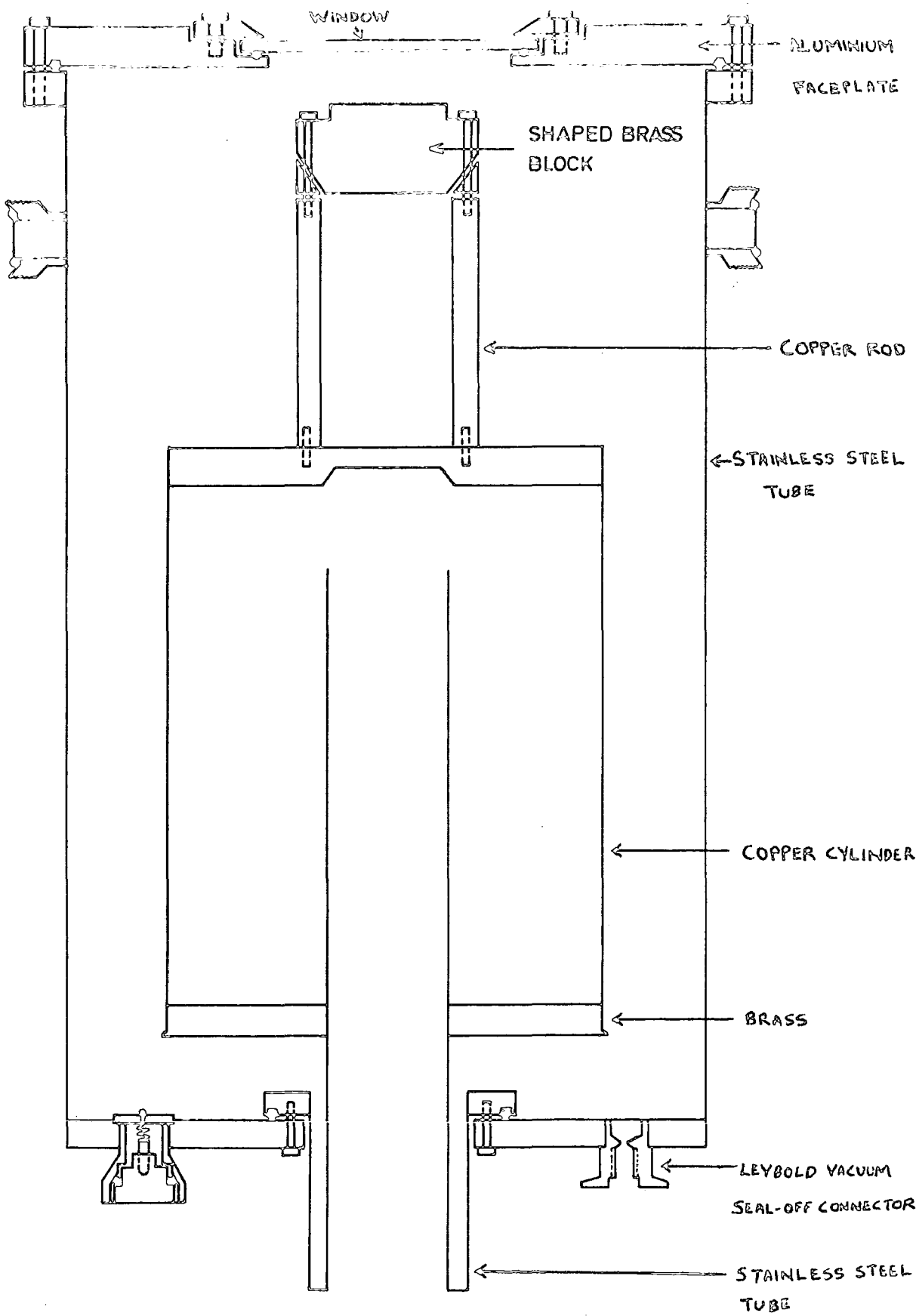

FIG. 3·10 THE COOLING SYSTEM

liquid nitrogen vessel is made from copper plate, while the end plate is made from a fairly heavy piece of brass. Such construction ensures that the temperature of the end plate does not change significantly with nitrogen level and vessel orientation. These latter materials are used because of their high thermal conductivities and their ready availability in the Workshop. The main heat loss of the system will be through the double tail pipe assembly. To minimise the heat loss, the double tail pipe assembly is built from a fabricated grade of stainless steel, chosen for its relatively poor thermal conductivity. Since the liquid nitrogen vessel and the vacuum container both have considerable surface areas, the radiation effects from their surfaces cannot be ignored. The radiation between the surfaces of the liquid nitrogen vessel and the vacuum chamber are reduced by covering these surfaces with aluminized mylar.

The evacuation of the cooling system is done by connecting a vacuum pump to the Leybold vacuum seal-off connector mounted on the rear plate of the vacuum container. As a precaution, in case the liquid nitrogen vessel might rupture in use due to the warming-up and cooling processes as well as the possibility of icing-up of the tail pipe, a blow-off valve is incorporated in the system. An optical grade glass window (9) about 6 cm in diameter is provided at the center of the front plate of the vacuum container. It was chosen for its good transmission properties, in

particular around the 1 micron region and also its relatively low cost.

The modifications done to the cooling system were as follows:

(i) A shaped brass block was mounted about 6 mm from the glass window by two cylindrical copper rods, which in turn are bolted onto the top end plate of the liquid nitrogen vessel:

(ii) The shaped brass block was machined down to the minimum surface area possible in order to minimize heat loss. This is illustrated clearly in Figure 3.10;

(iii) The CCD array was mounted on top of the shaped brass block and positioned centrally below the glass window, such that incident light falls directly to the image section of the CCD. The conduction of heat from the CCD array to the coolant may take place via the cylindrical copper rods and also through the use of strips of copper braiding which link the top end plate of the liquid nitrogen vessel to the shaped brass block. A heat sink compound is smeared on the backside of the CCD as well as on the top surface of the shaped brass block. This compound is supposed to improve the conduction process between the CCD and shaped brass block.

Obviously, from the above design the CCD array sits at some temperature between that of the coolant and the temperature of the surrounding environment determined by the relative conduction of device links (i.e. the two cylindrical rods and strips of copper braiding used) to the liquid

nitrogen vessel and also its links to the outside, principally the electrical connecting wires. In this sort of system the required operating temperature may be achieved through the use of carefully selected lengths of copper braiding linking the shaped brass block to the coolant vessel. Once a configuration has been found giving the required minimum operating temperature normally used (about -150°C), further adjustments can be made with a heater mounted on the shaped brass block. The CCD temperature is sensed by a platinum resistor mounted below the device package later superseded by a diode sensor (10). The platinum resistor and the diode sensor are prefered to thermocouple methods because they are current driven and may be operated some distance from their readout electronics with a simple two wire connection. All the electrical connections to the CCD, temperature sensor and heater are made via two M-type vacuum connectors mounted on the outside of the vacuum container. A picture of the finished cooling system with the location of the CCD array behind the front plate window and the signal processing unit attached to the body of the system is shown in Figure 3.11.

Two problems were encountered with the above cooling system during an experimental run on the 30 inch Coude telescope at RGO. Firstly, aligning and focussing the CCD at the focal plane of the spectrograph camera. Since the CCD is held fixed to the shaped brass block, aligning and focussing can only be achieved by moving the whole cooling

FIGURE 3.11 Photograph of the Cooling System

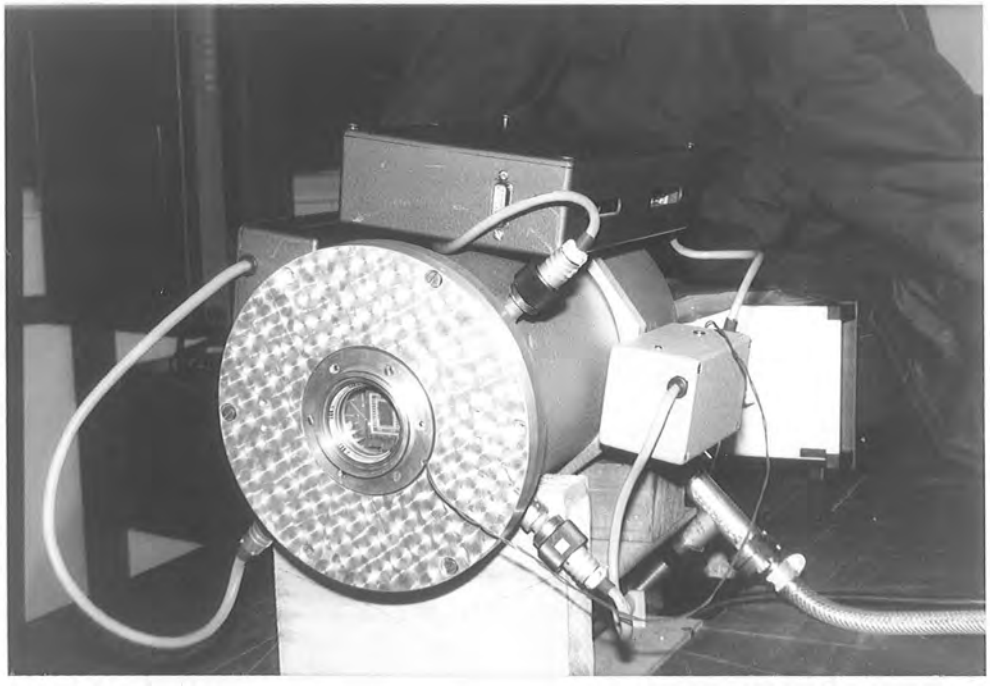

system either, forward, backward, vertically, horizontally, or in rotation. It would be convenient to have some form of movement mechanism incorporated in the system, such that the CCD array can be moved about instead of the whole cooling system. Secondly, for some reason, the glass window of the cooling system does get water vapour condensing on its surface. This phenomenon has not been observed in the laboratory. To overcome this problem a heater is provided at the glass window. It is very important to make certain that the CCD sits perfectly flat on the shaped brass block, otherwise a non-uniform temperature distribution across the chip will result, thus setting up a temperature gradient which would affect the collected data significantly.

3.11 Measurement of Leakage Rate of The Cooling System

In the above designs, it has been mentioned that different metals are used for different parts of the cooling system. This is necessary for reasons which have already been stated in the previous section. In practice, these metals were joined together with soldering during the early stages of the development of the cooling system. Inevitably there is always a chance of leaks remaining at the site of the joints. Thus it is necessary to check out the system for vacuum leaks. Unfortunately, the group did not have the use of a helium leak detector. However, since the ultimate vacuum required was not very demanding it was found possible to find leaks by the simple method of pouring alcohol onto suspected joints and observing on the pirani

gauge any small pressure changes which occurred.

The cooling system was assembled (as shown in Figure 3.12) and its leakage rate measured. Figure 3.13(a) shows an acceptable leakage rate, with the system at room temperature. The rate is 4.2×10^{-5} torr/litre/second. This leak rate is acceptable because in an overnight run the pressure would only rise to 0.05 torr. The leak rate is dramatically reduced when the system is cooled to liquid nitrogen temperature as shown in Figure 3.13(b). This reduction in leak rate is due to the pressure inside the system decreasing as the temperature decreases, which is derived from the Universal gas law equation (11). It may also be said that some of the gaseous molecules present in the system will condense at liquid nitrogen temperature, and thereby assist the pressure reduction.

A further reduction occurs with the introduction of zeolite which has the ability to absorb gases at low temperature. Detailed absorption properties of zeolite are given by Barrer (12). A typical leak rate in this case is shown in Figure 3.13(c). The leak rate is 6.9×10^{-6} torr/litre/second. The zeolite is contained in a sieve fixed at the bottom end of the liquid nitrogen vessel. With the above leak rate, the pressure inside the system is expected to change about 0.24 torr in 10 hours. Such a change in pressure inside the cooling system is acceptable for two reasons: firstly, the cooling system is evacuated

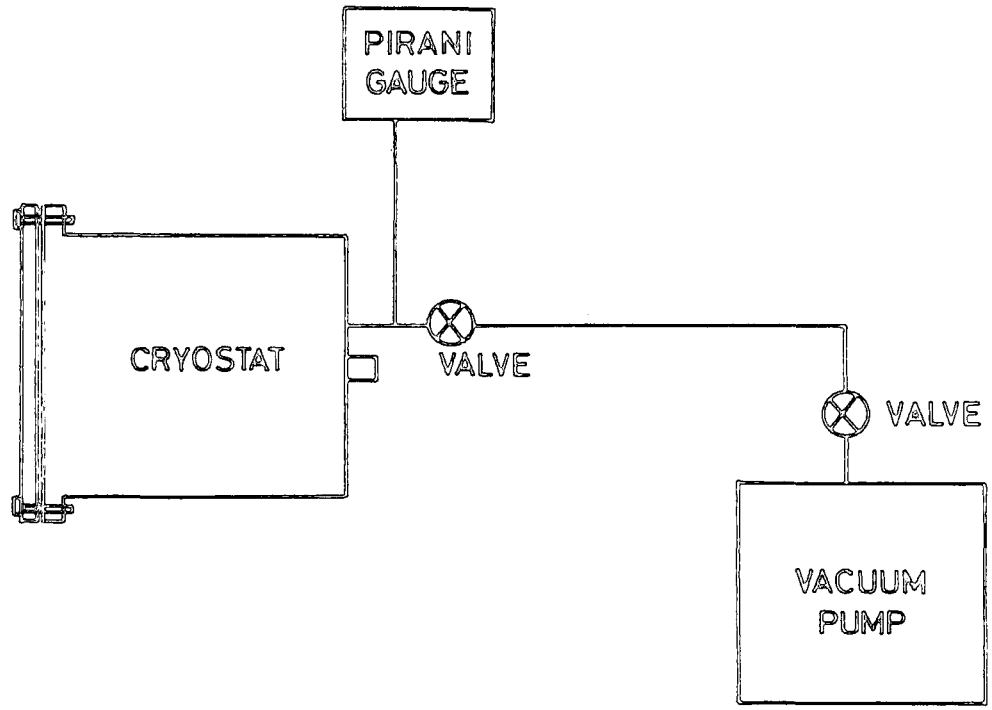

FIG. 3·12 A TYPICAL LEAKAGE RATE MEASUREMENT SET-UP

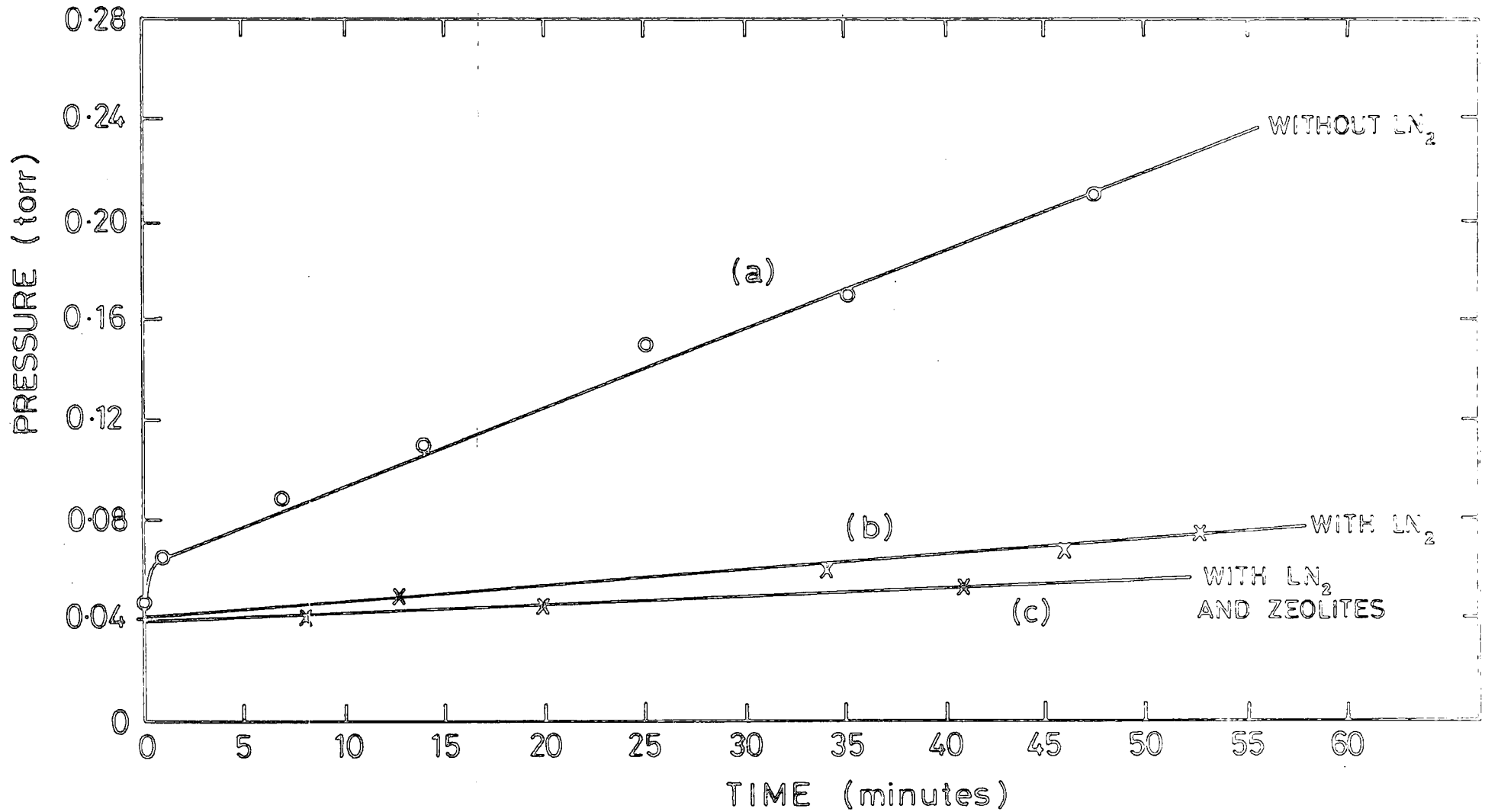

FIG. 3·13 TYPICAL GRAPHS OF LEAK RATES MEASUREMENT

continuously with a vacuum pump; and secondly, most of our exposure runs for collecting data are less than one hour. The hold time of the cooling system is approximately six hours when positioned vertically (i.e. the glass window facing upward), and reduces to about three hours in the horizontal position.

3.12 Summary

A complete computer control and data acquisition system has been designed and constructed for the General Electric Company charge coupled device, bearing in mind the requirements and specifications of optical imaging necessary for astronomical work. The CCD camera system is modular and based on the CAMAC concept. Provisions were made for operating a section of the CCD camera system under manual control, so that laboratory work on the CCD could be continued before the system development was complete. The CCD camera system is controlled by a small LSI 11/23 minicomputer running the Fortran programming language (to be described in the next chapter). Cooling the device helps to reduce the dark current, but also reduces the quantum efficiency of the device, especially at longer wavelengths.

REFERENCES

1. Choisser, J.P. (1975), "Experiments on the use of CCDs to detect photoelectron images", The Symposium on Charge Coupled Device Technology for Scientific Imaging Applications, p.150, JPL SP 43-21.

2. Currie, D.G. (1975), "On a photon counting array using the Fairchild CCD 201", The Symposium on Charge Coupled Device Technology for Scientific Imaging Applications, P.80, JPL SP 43-21.

3. Waltham, N.R. Ph.D. thesis, University of Durham in preparation.

4. EUR 4100e, Camac A Modular Instrumentation System for Data Handling (Description and Specification) 1969.

5. Digital Microcomputer Processor Handbook (1974-1980), published by Digital Equipment Corporation.

6. Uman, M.F. (1975), "The Introduction to the Physics of Electronics", Solid State Physical Electronics Series, Edited by Nick Holonyak, Jr., Prentice-Hall, Inc., P255-310.

7. Dash, W.C., and Newman, R. (1955), "Intrinsic optical absorption in single crystal germanium and silicon at 77k and 300k", Physical Review, Vol. 99, No. 4, p. 1151-1155.

8. Sieb, D.H. (1974), "Carrier Diffusion Degradation of Modulation Transfer Function in Charge Coupled Imagers", IEEE Trans. Electron Devices, Vol. ED-21, No. 3, 210-217.

9. Ealing Optics Catalogue, "Transmission of optical materials", p. 464.

10. Waltham, N.R., Clark, G.F., and Tanner, B.K. (1981), "Low Temperature Thermlmetry using inexpensive silicon diodes", Physics Education, Vol. 16, 104.

11. Resnick, R., and Halliday, D. (1960), Physics for Students of Science and Engineering, Part 1, p. 489-512, Published by John Wiley & Sons Inc.

12. Barrer, R.M. (1978), "Zeolites and Clay Minerals as Sorbents and Molecular Sieves", Academic Press, London - New York - San Francisco.

CHAPTER 4

DATA ACQUISITION SYSTEM AND ASTRONOMICAL OBSERVATION

4. INTRODUCTION

In chapter 3, the modules designed and built for the CCD camera system have been described briefly in terms of their functions. It was mentioned that the development of the CCD camera system was based around a possible operational sequences which might be employed to run the device in the direct-photon integration mode. The operational sequences chosen comprises of three stages (these stages have been outlined in Chapter 3). However, for clarity, the three stages shall be mentioned briefly here as the following: (i) a setting up period during which the CCD is scanned 5 or 10 times prior to an exposure, in order to remove any residual charges present in the storage and readout registers of the CCD; (ii) an integration time for which the incident photon flux generates photoelectrons and are collected at the photosites of the CCD; and (iii) a final readout scan at which the collected photoelectrons are transferred to the line readout registers and readout one pixel at a time using the correlated double sampling technique. This operational sequence seemed suitable for astronomical work. With the present CCD camera system, the above operational sequences may be accomplished through appropriate gating of the 16 camera control lines (i.e. the 16 bit control word which are tabulated in Table 3.1), thereby enabling or disabling the control signals and clock pulses of the CCD camera as required. Since the CCD does not have the non-destructive

readout (NDRO) facility, it is useful if the operator may terminate the integration at will so that an early assessment of the data can be made, e.g. to see any signal features (i.e. spectral lines) present in the frame. This is helpful in determining roughly how long an exposure is required before a signal-to-noise of say 100 is achieved, assuming fairly constant "seeing" conditions.

Although the above operational sequences together with storage of data on some permanent medium could be implemented by a hardwired controller, the data manipulation required is very much easier to perform with a minicomputer system. Such a system is extremely flexible, mainly because all the control functions are undertaken by software of the computer. Thus, allowing the operator total control of the operation of the CCD camera system. Furthermore any minor changes to parameters such as length of integration time, different form of operational sequences chosen, etc. may be done in software.

Development from earlier systems (i.e. the Plessey Photodiode array project), saw a simple stand-alone paper tape system (1) which uses a PDP 1103 16k memory microcomputer and Hytec crate controller to run the array. This system is based around CATY (2) and interfaced through CAMAC. In this system the experimental data was dumped onto punched tape, a slow process. System flexibility was limited by the lack of fast backing storage, programs also having to be read from tape, therefore it just read numbers from the CAMAC crate and punched them onto tape. The raw data could

be displayed on-line with a bistable graphics 603 storage scope, interfaced through CAMAC, but any reduction e.g. flat fielding required the relevant data tapes to be re-entered after the resident program had been changed.

Later the paper tape system was replaced by a floppy disk unit. Floppy disks allowed faster data storage, program retrieval and use of standard DEC operating system RT-11. CATY was still used at first but later a FORTRAN package was acquired with Culham FORTRAN CAMAC handlers. Early systems were used with one-dimensional detectors where speed of operation and memory capacity are not so important. In order to handle large amounts of data from two-dimensional devices, it was necessary to have a hard disk (10.4 Mbyte RL 02). This provides much greater storage capacity and faster data handling in the system.

4.1 The Computing System

The present system, illustrated schematically in Figure 4.1, comprises: a DEC PDP 1123 microcomputer with 28K directly addressable memory; an RXO2 dual drive, double density, floppy disk unit for program storage (may also be used for data storage); a RLO2 disk drive, double density (10.4 Mbyte) removable disk cartridge unit for data storage; a CAMAC system with data acquisition electronics and other user selectable CAMAC features, interfaced through a Hytec 1104 card which also contains a ROM bootstrap; a visual display unit (VDU) interfaced to the computer via the DLV-11 serial interface card (the VDU is the console device for the

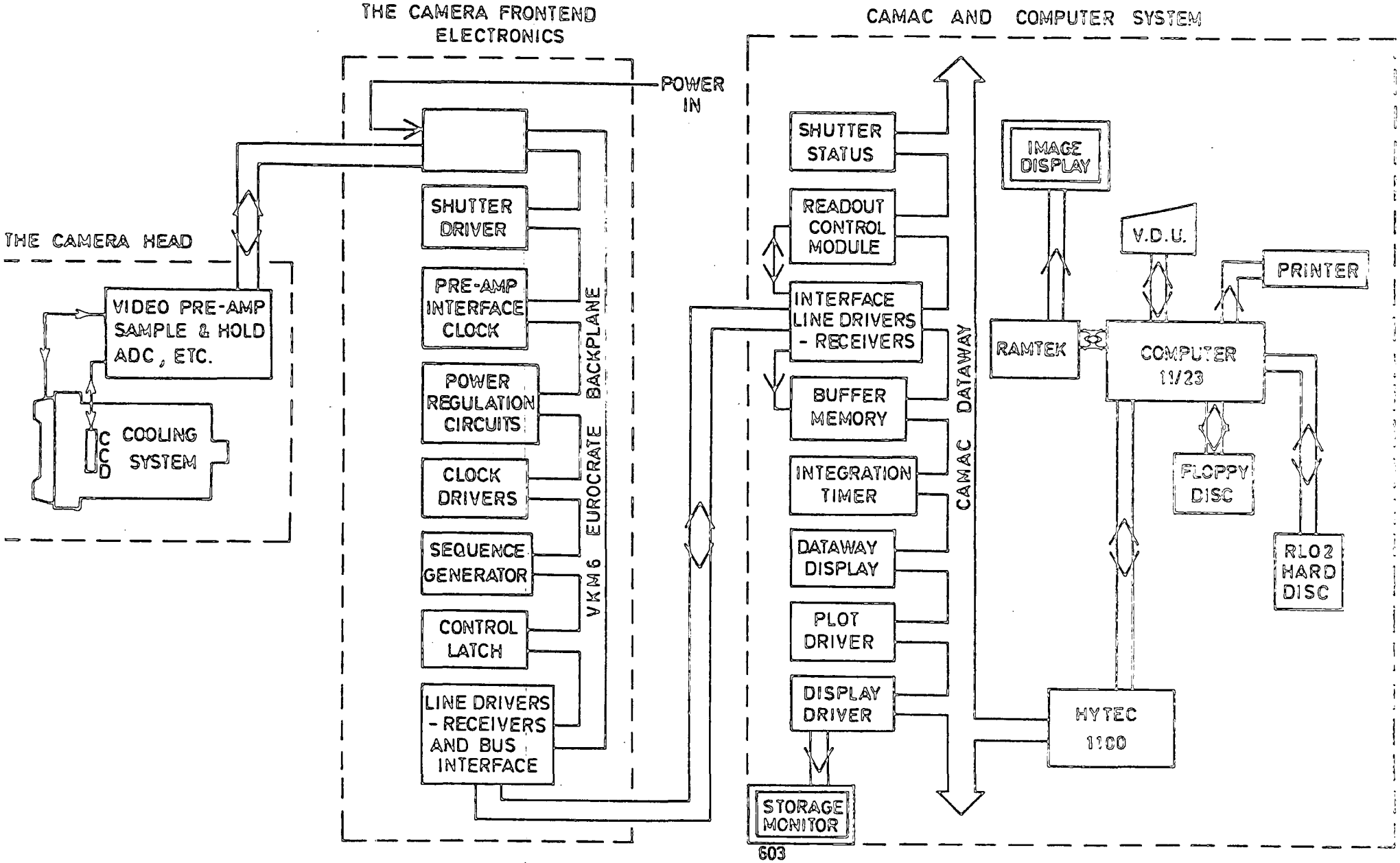

FIG. 4·1 A BLOCK DIAGRAM OF COMPLETE C.C.D. SYSTEM

computer); a graphics display which is interfaced through CAMAC by a storage display driver, NE9028 and a mode generator, NE 7011 (3); an image display unit called Ramtek; and a serial printer which is connected directly to the computer through a serial port. The above disk system is operated under RT-11 (i.e. DEC's standard software) which supports a variety of high level programming language, including BASIC and FORTRAN.

During the earlier stages of development of the CCD camera system, a specialised CAMAC control language called CATY which was supplied by Francis Golding Associates, has been used for purposes of control and acquisition. CATY is very easy to learn and use because it uses statements and commands which are a subset of BASIC. A version CATY80 is available to run with RT-11 making use of any of the RT-11 device handlers for input and output which means that data may be dumped into disk files or output on any other system peripheral from a running program.

In CATY the execution time is fairly good because the single run command first compiles the entire program and then begins execution, whereas in BASIC, at execution time, each statement in the source code is translated into machine code and executed before passing on to the next statement. It seems that CATY is ideally suited to real time systems. However, because the operating system (i.e, the RT-11 resident monitor), the source program, the compiler and the compiled version of the program are all resident in

memory, therefore the utilisation of memory is rather inefficient. Other more obvious disadvantages are that CATY can only perform very limited arithmetic operations because it is restricted to the use of integers and may only have 26 variables (vectors and scalars). Thus a CATY based system does not allow considerable on-line data reduction or graphics capability.

Finally CATY was replaced by FORTRAN for actual data acquisition in the present system. It was chosen because it is a highly versatile language and may perform both data acquisition (via special subroutines) and analysis.

4.2 Charge Coupled Device Operation

The basic principle of operation of the General Electric Company CCD intended for optical imaging work has been described in Chapter 2. When driven with the system described in Chapter 3, the CCD becomes practically an imaging array suitable for astronomical spectroscopy. However, the suitability of the CCD as an imaging array for astronomical spectroscopy depends on its geometrical layout and upon its opto-electronic properties. These factors have been discussed in previous chapters and will not be considered further.

In using the system described in Chapter 3, the on-chip operation of the CCD (i.e. collection of charges in the image section and transferring these collected charges into the read-out register) has been fully accounted in Chapter 2. In this section the readout operation of the CCD (the on-chip output detection amplifier and the off-chip signal processing

unit) and a typical sequence of events will be briefly described.

From Chapter 2, it has been noted that the line read out register of the CCD has a total of 400 elements, and one register element is associated with each of the horizontal pixels in the array; plus eleven extra at the output end of the register and four at its input. This means that the collected signal charge in the image section when shunted into the readout register will occupy from the fifth element to the 389th element of the read-out register. Therefore, when the contents of the 400 elements are sequentially read-out and displayed on a video monitor, it should be observed that the first eleven elements do not contain any signal charge, although there may be some thermal leakage current from the readout register wells. A similar situation exists for the last four elements of the readout register. This enables us to estimate any schematic drift in the d.c. level of the acquisition electronics during the time a line is being read out. For this reason, instead of only reading the 385 active elements, it was decided to read-out all 400 elements for the purpose of data reduction and later analysis work.

The CCD is read out destructively line by line, whereupon the frame of data is transferred from the buffer memory and displayed in order to check that the output signal is well within the ADC input range. Typically, a line read out of the present system takes about 20 ms, which means a pixel

or element readout time is about 50 μs.

A timing diagram of one pixel readout, which is shown in Figure 4.2 is summarised below. The fact that the signal from a CCD is the difference between the amplifier output voltage before and after the charge is transferred necessitates the use of some form of differential sampling technique to achieve optimum results (i.e. which maximises the final signal-to-noise ratio). In the present system, as mentioned earlier a dual stage integrator scheme (with initial d.c. offset adjustment) is employed for sampling the signal.

The operating mode of this scheme is as follows. At first the reset switch T_1, is turned on as the reset pulse ϕ_R goes high and the voltage (say V_i) across the output capacitor C_o is reset to the reference voltage V_{RD} with a noise uncertainty V_n. This noise voltage may be introduced through inadequate filtering of the Nyquist noise contribution of the reset switch (4) and the reference supply voltage. At the start of the reset interval the pixel charge is transferred into the last well (i.e. the readout clock pulse $H\phi_2$ goes low and $H\phi_3$ goes high) which is adjacent to the output gate (OG) and the collection diode (refer to Figure 2.7).

When the reset switch T_1 is turned off (i.e. the reset pulse ϕ_R goes low), the voltage present on the output gate of transistor T_2 (refer to Figure 2.8) consists of a feed-through pedestal ΔV_{RD} and a noise voltage V_n. The integrator,

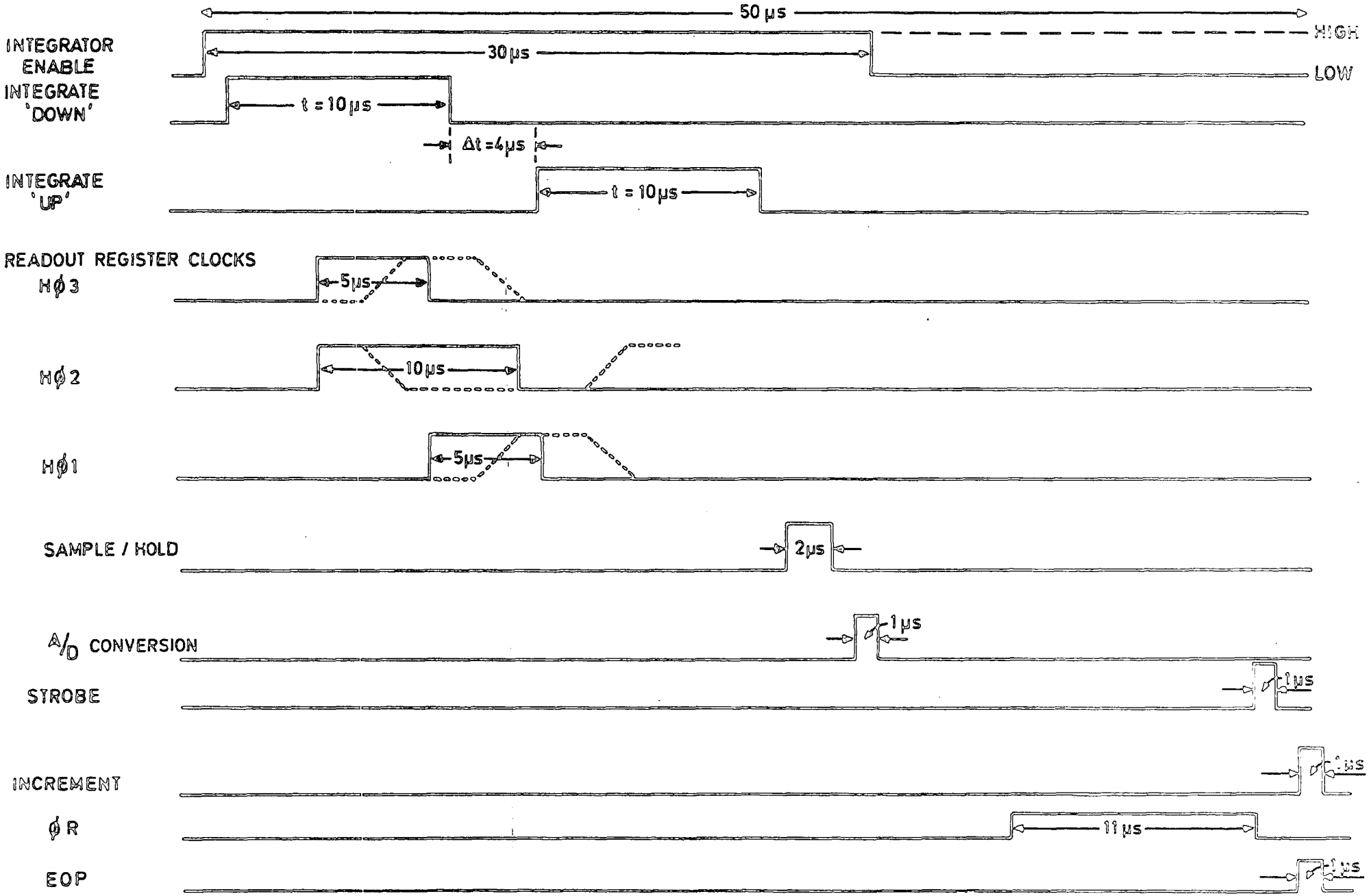

FIG. 4·2 TIMING FOR ONE PIXEL READOUT

(shown schematically in Figure 4.2.1) on the video pre-amplifier board is enabled as the integrate "Enable" pulse goes high (i.e. the switch SW3 is closed). The integrator is enabled for about 30 μs. During this period the signal charge from the CCD is sampled, and the sampled signal at the output of the integrator is then available on hold for A/D conversion (and subsequent data storage) prior to resetting. Immediately 1 micro second (μs) after the integrate "Enable" goes high, a second pulse called the integrate "Down" goes high. This pulse will close the switch SW1, thus connecting the inverting input of the integrator to the output of the first operational amplifier stage. This operational amplifier is configured as a non-inverting input with a d.c. offset adjustment having a gain of A = 11. The CCD output is fed to the non-inverting input of the operational amplifier. The output of the operational amplifier represents an amplified signal voltage (i.e. the product of reset voltage on C_o and the Op-amp gain) of the CCD output. This amplified signal voltage is allowed to charge the capacitor C_1 of the integrator when the switch SW1 is closed. After 10 μs, the integrate "Down" pulse goes low and the measured reset level is holding on a high impedance point formed by the integrator capacitor C_1.

When the $H\phi_3$ pulse goes low the signal charge in the last well is transferred to the collection diode. The signal charge (minority carriers) discharges the voltage on the output capacitor C_o to a value say V_o. This voltage is

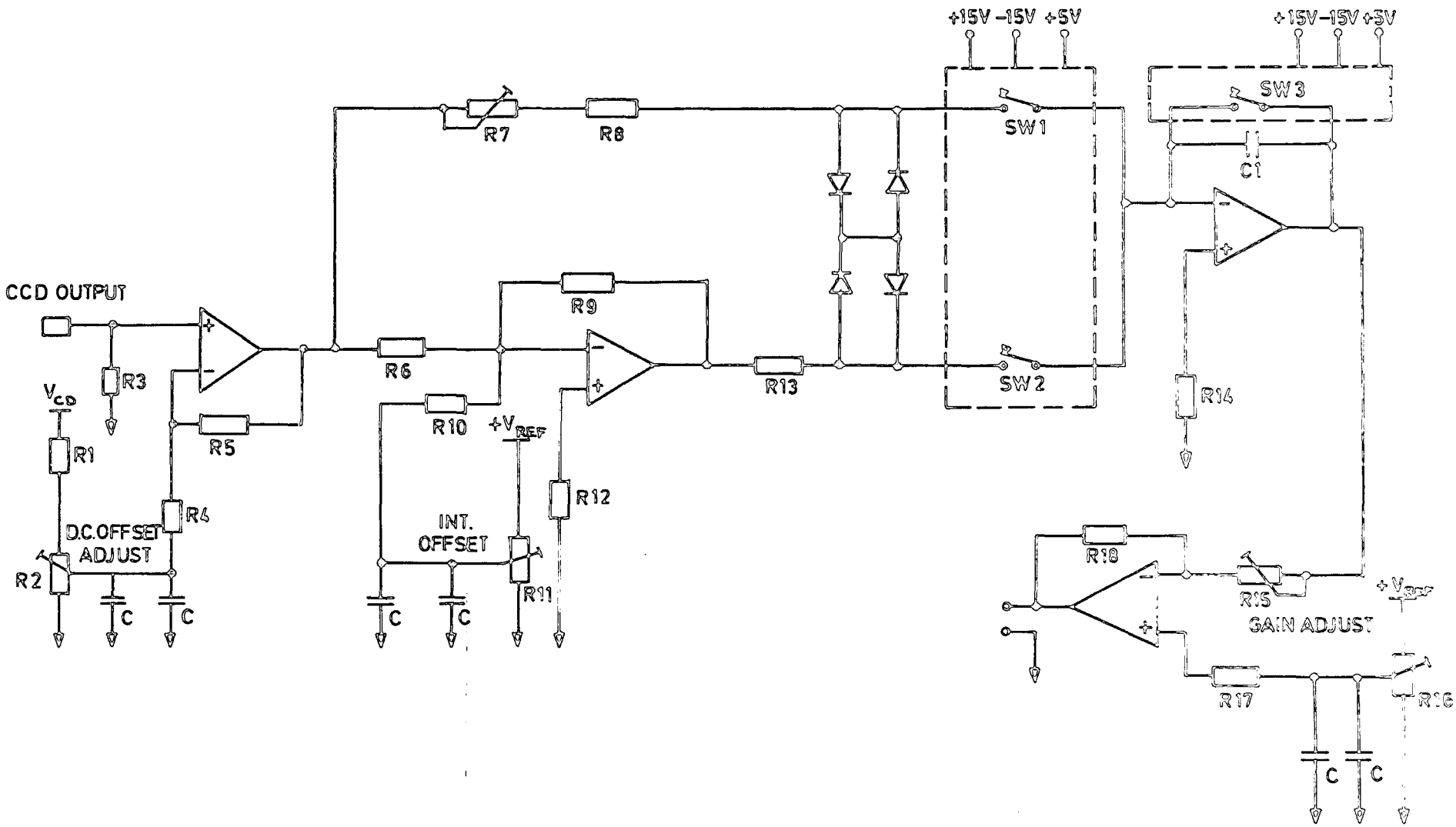

FIG. 4·2·1 : SCHEMATIC DIAGRAM VIDEO PREAMPLIFIER

present at the output of the CCD. It is amplified by the first stage operational amplifier and then fed to an inverting input of a unity gain buffer before being presented to the inverting input of the integrator via the switch SW2. Thus, the signal voltage is made to have an opposite polarity from the previous measured voltage (i.e. the reset level voltage). When the switch SW2 is closed, due to the integrate "Up" pulse goes high, the capacitor C_1 is charged with opposite polarity. At the time the integrate "Up" pulse goes low, the integrator output consists of a signal voltage which is the difference between the measured reset level and the same reset level plus signal increment introduced by the minority carriers. Thus, this signal voltage is now free from reset noise and proportional to the minority carrier signal increment introduced by the last well to the output capacitance C_o via the collection diode. This signal voltage, which comprises of sensor and readout register thermal leakage current added to photo-charge is amplified and passed to the input of the sample and hold, whereby it is sampled for two microseconds and then available on hold for A/D conversion. The A/D conversion takes about 1 μs. At the end of this conversion, the integrate "Enable" pulse goes low and thus resetting the integrator.

When the data at the parallel outputs of the 16-bit ADC is valid, they are strobed into the buffer memory with the strobe pulse. This is followed shortly by an increment pulse which incremented the address counter of the buffer

memory. Simultaneously an "End of Pixel" (EOP) pulse occurs, thus indicates the end of one pixel readout. Notice that in Figure 4.2, the reset pulse Φ_R, goes high after a few microseconds of the conversion time and goes low as the data from the parallel outputs of the ADC are strobed into the buffer memory. This is to ensure that the output capacitance C_o is reset before the next pixel readout begins and so on. The "EOP" pulse occurs every 50 μs interval. The above process is repeated until all the 400 pixels have been readout and finally an "End of Line" (EOL) pulse occurs, which means the end of a line readout.

In the above sampling process, the sampling interval τ = 10 μs and the delay between the samples $\Delta\tau \approx 4$ μs were used. The signal charge in the last well is transferred to the output diode during $\Delta\tau$. This is to avoid pulse feedthrough, however $\Delta\tau$ must be kept short in comparison with τ or else the signal is lost. Using the dual slope integrator scheme not only eliminates reset noise but also reduces the noise contribution from the output transistor, especially in the low frequency $^1/f$ region (5).

For astronomical spectroscopy application, a typical operational sequence of events was chosen to run the CCD camera. This operational sequence of events, which is shown in Figure 4.2.2, may be described as the following. At first the operator will load a run table and then set an integration time say 1, into the running programme via the VDU keyboard. A typical run table content is given in

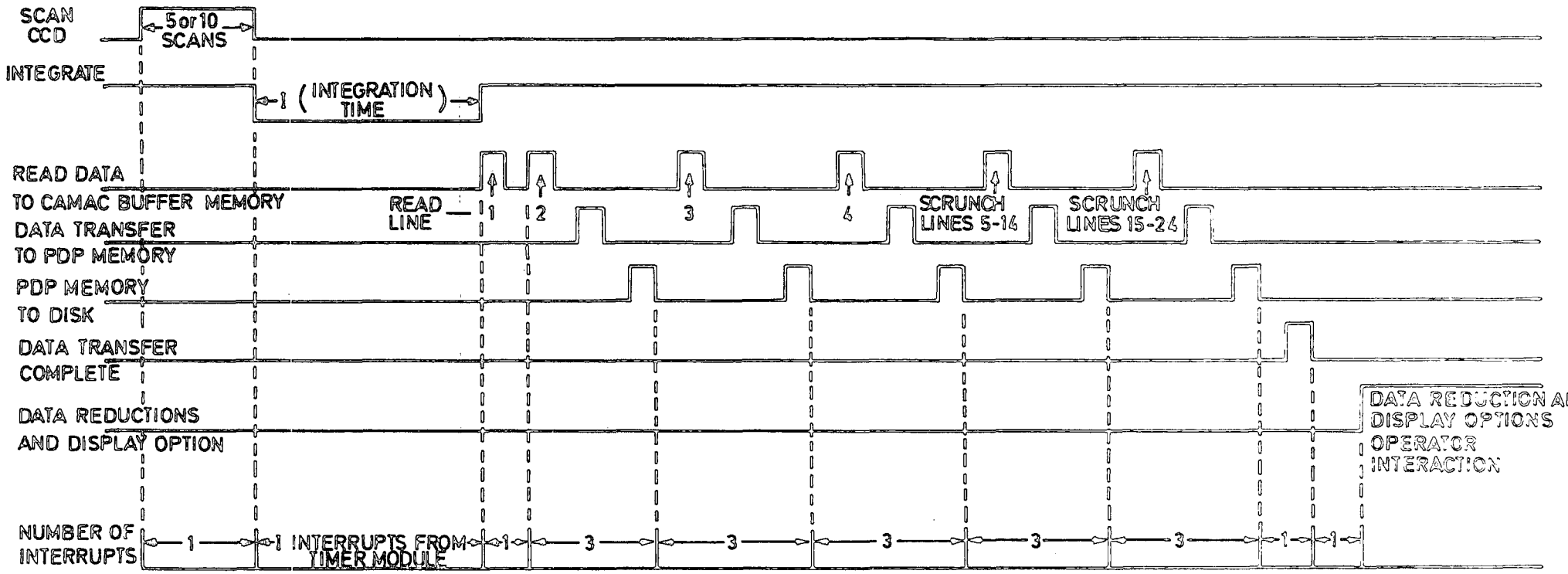
SCAN CCD
5 or 10 SCANS
INTEGRATE
1 (INTEGRATION TIME)
READ DATA TO CAMAC BUFFER MEMORY
READ LINE
1
2
3
4
SCRUNCH LINES 5-14
SCRUNCH LINES 15-24
DATA TRANSFER TO PDP MEMORY
PDP MEMORY TO DISK
DATA TRANSFER COMPLETE
DATA REDUCTIONS AND DISPLAY OPTION
DATA REDUCTION AND DISPLAY OPTIONS
OPERATOR INTERACTION
NUMBER OF INTERRUPTS
1
1 INTERRUPTS FROM TIMER MODULE
1
3
3
3
3
3
1
1

FIG. 4·2·2

Table 4.1. The run table is programmed to run the CCD camera i.e. it contains the command required for execution of sequence of events chosen to run the CCD. When a "Run" command is issued by the operator, firstly the camera servicing routine (i.e. the camera interrupt routine handler) is cleared without any other action (Null Function). When the next interrupt is received by the computer from the camera, the CCD array is cleared 5 times in order to remove any residual charges present in the CCD before an exposure is started. On the next interrupt occurrence, the camera shutter opens and integrates for user set period of time (i.e. I seconds). At the beginning of the integration period the camera interrupts routine is disabled and interrupts from the CAMAC integration timer module are enabled. The elapsed time is displayed by the CAMAC dataway display module. At the end of the integration period (i.e. after the final interrupts of the integration time), the camera shutter closes and the interrupts from the CAMAC integration timer module are disabled. This is followed by the camera interrupts being enabled. When the next interrupt is generated, the first line of the CCD is readout and stored in the CAMAC buffer memory module. The first line of data are not stored on the hard disk because it has been found that the first line of readout from the CCD seems to be corrupted. The corruption of data is caused by a software bug and only occurs during the first line readout and data transfer operation. The next interrupt will cause line two

TABLE 4.1

A TYPICAL RUN TABLE CONTENT

COMMAND	FUNCTION
Set Intensity - 6	Set Intensity of 603 monitor to 10 M.S.B.
Null Function	Clear the Interrupt of Camera.
Clear 10 289	Clear 10 lines of CCD 289 times i.e. Scanning CCD 5 times.
Integrate	Start integration, shutter opens, Interrupts from Timer Module Enabled.
Clear 1	Clear 1 line of CCD i.e. Read 1 Line and Store in Buffer Memory Module
Read 1 3	Read 1 Line of CCD and Stored on Hard Disk, do Three Times.
Read 10 2	Read 10 Lines of CCD and Stored on Hard Disk, do Twice.
Plot/Display	Plot Data on the 603 Storage Scope Monitor
End	End of Run

of the CCD to be readout and stored in the buffer memory, thus overwriting the first line of data stored previously in the memory chips. The data in the buffer memory is then transferred to the PDP 1123 memory. Finally, the data from the computer memory is dumped to the hard disk for permanent storage. The process of readout and storing of data onto the hard disk takes three interrupts. Similarly lines three and four of the CCD are readout in the same manner as above. After the data from line four of the CCD has been stored on the disk, on receiving the next interrupt, lines five to fourteen of the CCD are scrunched, i.e. binned together onto the readout register and then readout for storage permanently on the hard disk. This is followed by scrunching lines 15 to 24 of the CCD readout and dumped to the hard disk. Therefore the data file on the hard disk contains five lines of data. As soon as all the lines are readout and stored, the next interrupt will cause the scrunched data (i.e. lines 5 to 14) to be displayed onto a video monitor. When the data has been displayed, the next interrupt will cause the end of the run, giving a "Run Finished" message on the VDU screen. At the same time the camera interrupt servicing routine is disabled and the computer will revert to its internal priority task operation. Now the frame of data which is stored on the hard disk may be recalled by the computer for simple data reduction, plot and display routines.

In the above operation, five lines of data have been stored for data reduction and analysis work in astronomical spectroscopy. Lines 1 to 3 in the data file are the data from lines 2, 3 and 4 of the CCD respectively. These lines do not contain the signal from the observed object (i.e. starlight). The signal charges present in the above lines are primarily the collection of thermal leakage current from the sensor and the readout register wells. This gives us an estimate of the dark current contribution to the 'true' signal charge collected. Line 4 of the data file contains the scrunched data from lines 5 to 14 of the CCD. The signal charge collected in these 10 lines is proportional to the incident starlight falling onto the CCD. Finally, line 5 of the data file contains the scrunched data from lines 15 to 24 of the CCD. The signal charge present in these 10 lines is supposed to be the sky background signal. Detailed use of these lines of data for analysis will be discussed in Chapter 6.

4.3 Software and Acquisition Program

The development of the software and acquisition program for the CCD camera system will be described in detail by G.P. Martin (6), but briefly, the philosophy in its layout structure has been to make it as general and expandable as possible. A typical flow diagram of a control and data acquisition program is illustrated schematically in Figure 4.3. The programming language used is FORTRAN. A FORTRAN package was acquired with Culham FORTRAN CAMAC handlers.

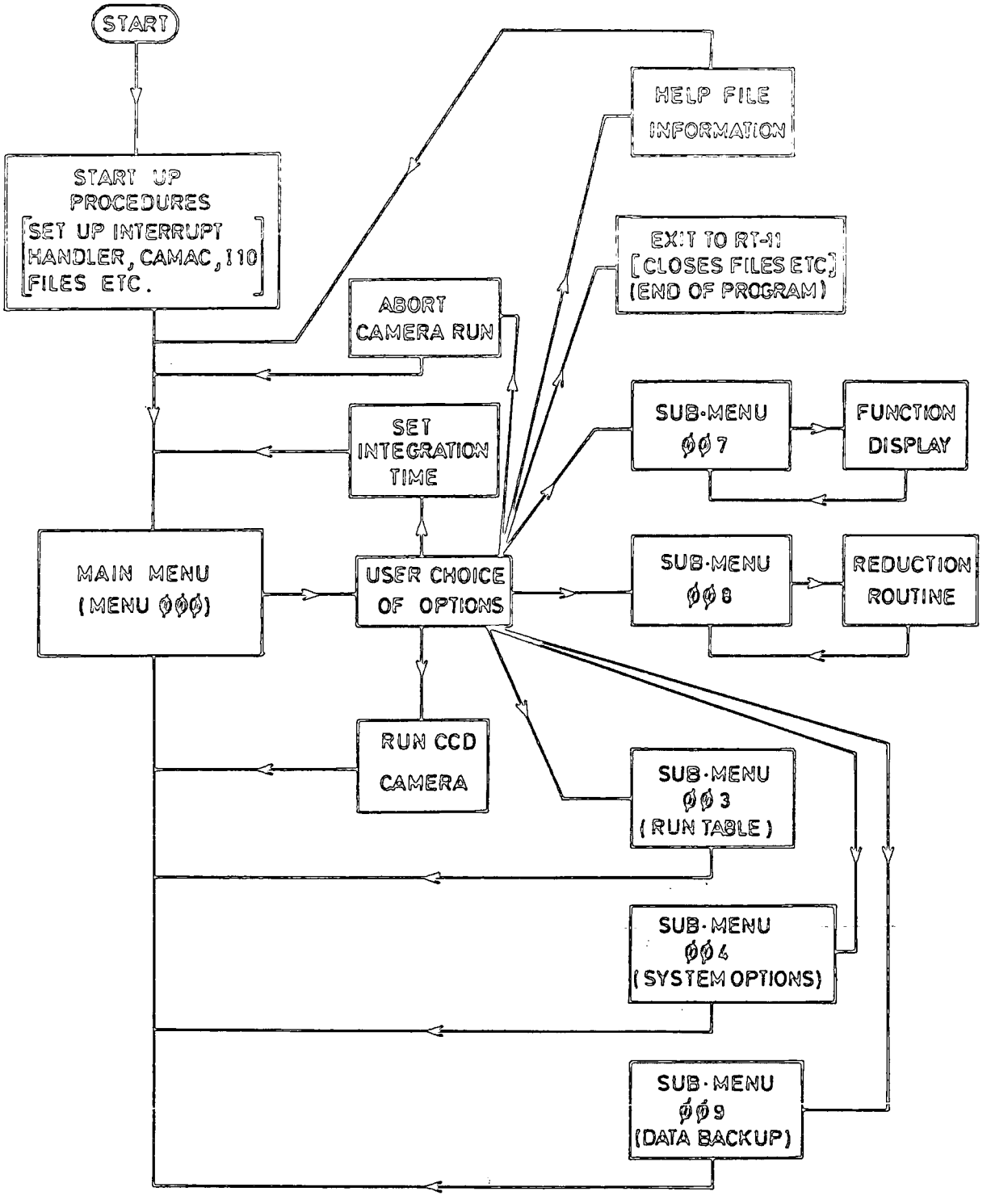

FIG. 4·3 CONTROL PROGRAM FLOW CHART

This package together with the RT-11 (DEC's standard software) forms the system software.

Referring to Figure 4.3, at the start of the program the variables and arrays used by the program are declared, many of them allocated to common storage blocks, thus allowing them to be access by the various subroutines in the program. This initialisation section also sets up the CAMAC stations to be used, the interrupt handler and any necessary input/output files. When all the start up procedures have been completed a table called the main menu (Menu 000) will be displayed on the VDU screen. This menu lists the user options available in the system. At present there are 10 options listed in the menu, as follows:-
(1) the help file, containing information about the choices available from the menu; (2) integration time, to display the current camera integration time, and allow the user to alter it; (3) Run Table, causes sub-menu 003 to be entered and displayed on the screen, allowing functions relating to camera run table to be executed; (4) system options, this causes a sub-menu 004 to be displayed on the screen which contains functions to set various system options; (5) Run start, starts a camera run: the camera then operates at interrupt level, asynchronously for the rest of the program; (6) Abort, premature termination of a camera run; (7) Data display and plot routine, this causes a sub-menu 007 to be displayed which offers a variety of data display and plot functions; (8) Data reduction, this gives sub-menu 008 which allows a choice of simple data reductions; (9) Data

backup, this shows sub-menu CO9, allowing the use of data back-up and transfer functions; and (10) Exit to RT-11, this is a routine that tidies up (closing open files etc.) and then stops the program, exiting to RT-11. However, when this option is chosen it does query the operator, in case the option was selected by accident.

In option (5) above, as mentioned the camera operates at interrupt level, asynchronously for the rest of the program and this operation may be shown roughly in Figure 4.3.1. When an interrupt is issued by the camera, the computer will get the next command from Run Table (i.e. referring to the main program) as set-up by one of the menu functions. This function is then executed and returns to the start of the interrupt routine, i.e. waiting for the next interrupt to occur before the next command in the Run Table can be executed and so on.

Some points about the acquisition programme are worth mentioning here. This menu and sub-menu layout structure provides flexibility for the operator to interact directly with the main programme. For instance, if the operator decided to enter different forms of Run Table (i.e. the way the lines of data in the CCD are to be readout and stored or displayed to an image display unit) to operate the CCD camera. This may be done by choosing option 3 from the main menu and sub-menu 003 will be displayed. In this sub-menu are options for creating (i.e. editing) Run Table and compiling and loading the new version into the main program,

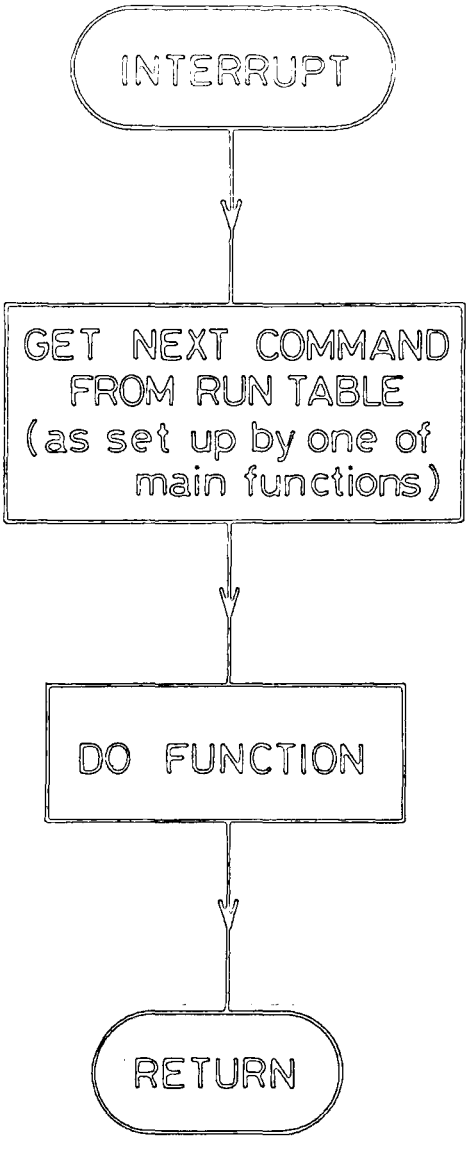

FIG. 4·3·1 INTERRUPT HANDLER (RUNS CAMERA) FLOW CHART

allowing the operator freedom to create a "Run Table" as required.

While waiting for the run (i.e. exposure time) to finish, the operator may want to look at the previous run data or do some simple data reduction to it, and this may be achieved by selecting the options (7) or (8) in the main menu.

4.4 Astronomical Observation

Several field trial runs of the CCD camera system have been conducted at the 30 inch reflector telescope at the Royal Greenwich Observatory (R.G.O.). During the field trips many observing programs of astronomical spectroscopy work have been attempted. One of the observing programs that will be discussed here is the compilation of a near infra-red spectral atlas of the M3 giant HR 5490 covering the wavelength interval of $\lambda 9748\mathring{A}$ to $\lambda 10153\mathring{A}$. This wavelength region was chosen because it is relatively free of strong water absorption features since it lies well outside the $\wp$ and σ bands (7) ($\lambda 9123\mathring{A}$ - $\lambda 9665\mathring{A}$) and before the ϕ band of the telluric H_2O ($\lambda 10844\mathring{A}$ - $\lambda 11409\mathring{A}$). This was the first time a spectral atlas had been compiled for this class of star in this part of the spectrum.

During May 1982 for six nights the CCD camera system was placed on the 30 inch reflector telescope to take seven overlapping frames of the M3 giant HR 5490 and a nearby hot star α CrB. The right ascension, declination, spectral type and magnitude of these stars are tabulated in Table 4.2. from this table it can be seen that the two stars have a

TABLE 4.2

Name of Star	Right Ascension* h	m	s	Declination* o	m	Spectral Type	Magnitude V
HR 5490	14	42	38	+ 26	36	M3 III a	4.8
α CrB	15	33	56	+ 26	46	AOV	2.2

* EPOCH OF COORDINATES IS 1950

similar declination and are separated by 50 minutes of right ascension. Since the two stars are in approximately the same part of the sky, we should expect that the respective air masses were not too different. Therefore this should allow the removal of telluric lines present in the M star frame, i.e. by dividing the M star frame with the hot star frame taken with the same set-up. In the next sections the full operating procedure for this observation will be discussed. Beginning with a brief description of the telescope system.

4.4.1 The 30 Inch Reflector Telescope. The 30 inch reflector telescope is a coude instrument. It is arranged as an F/47, 4 mirror coude, with the beam directed up the northerly extension of the polar axis (as shown in Figure 4.4.1) and reflected vertically downwards by a flat mirror to the slit of the specgrograph, the axis of which is therefore vertical. The telescope can be driven at sidereal rate only, and has manual or autoguider override controls. The observer can first set the star near the slit by setting the telescope manually (i.e. setting the R.A. and declination of the star) and then lock in the automatic guider. This automatic guider can be released by the observer through the manual override control if required by sky conditions (e.g. cloudy spells).

There is a small finder attached to the telescope with a field of the order of 1°, a centering eyepiece covering

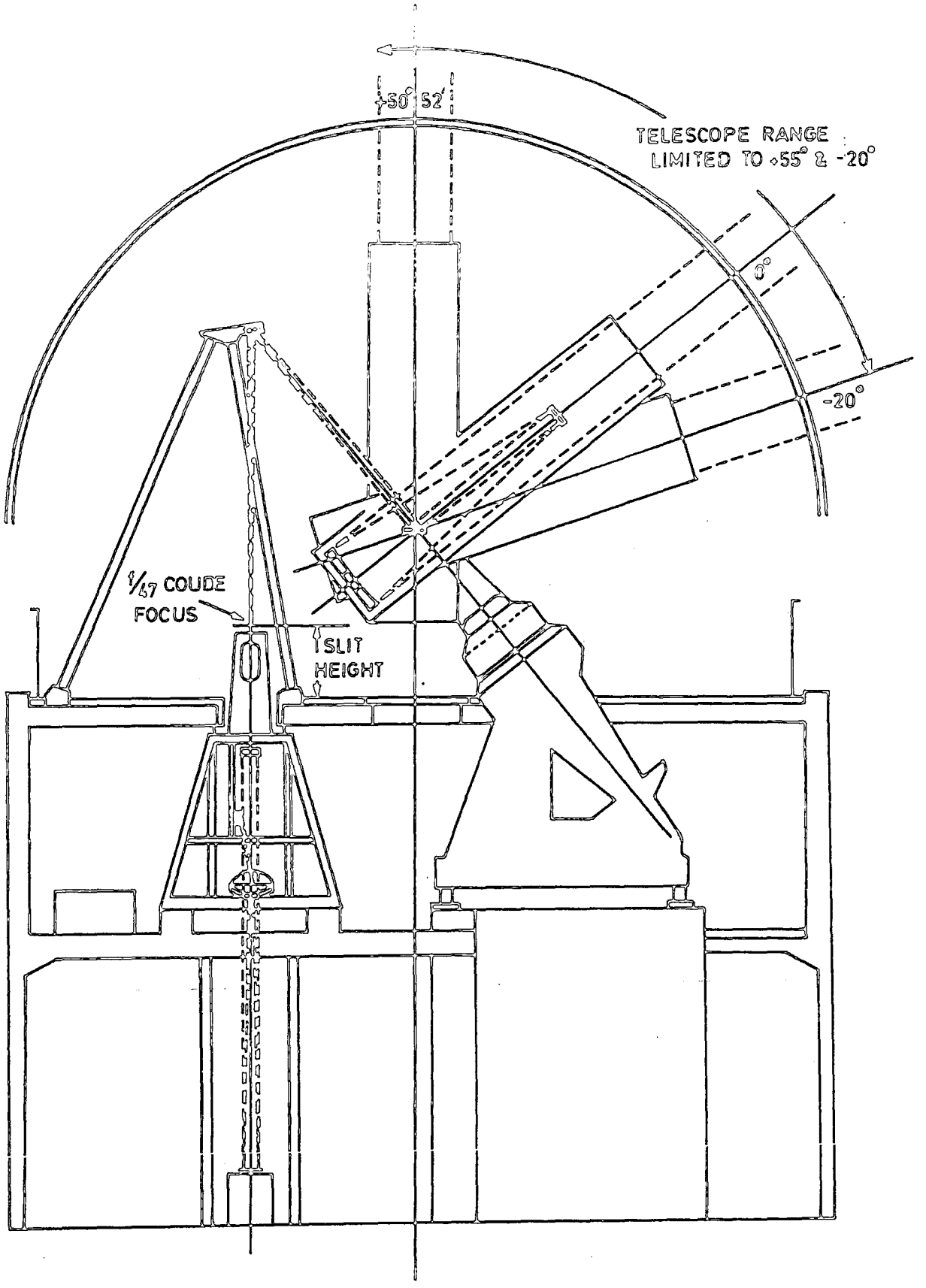

FIG. 4·4·1 R.G.O. 30° REFLECTOR COUDE ARRANGEMENT (view looking east)

a field of about 7 arc minutes and a guiding eyepiece has a field of about 20 arc seconds. When the position of the observed star has been set, on viewing through the centering eyepiece (this viewing is only possible by pulling across a flat above the slit assembly, which will then direct the telescope beam to the centering eyepiece), the star should appear in the 7 arc minute field. Then the star must be set near the left hand edge of the central "box" (in the centering eyepiece) using the manual control. Now if the flat above the slit assembly is removed, the star should appear in the 20 arc seconds field, i.e. on the slit. Since the guiding eyepiece looks at the light reflected from the slit jaws, centering the star in the field eyepiece is important.

The Coude spectrograph of the 30 inch reflector comprises a collimator mirror, a 600 grooves mm^{-1} grating blazed at 10000Å in first order, and two mirrors used to focus the beam coming from the grating to a focal point as shown in Figure 4.4.2. The slit to CCD factor for this coude system is 7:1. The detailed mechanical arrangements of the telescope are described in the telescope handbook (8).

In operation the CCD was placed at the focal plane of the spectrograph with the 385 pixels (each pixels being 22 μm square) in the direction of dispersion to facilitate on chip pre-binning and a fast readout time. Since the grating is blazed at 10000Å in 1st order, this produces a dispersion of 8.6 Å/mm and thus, the 385 pixels covered a

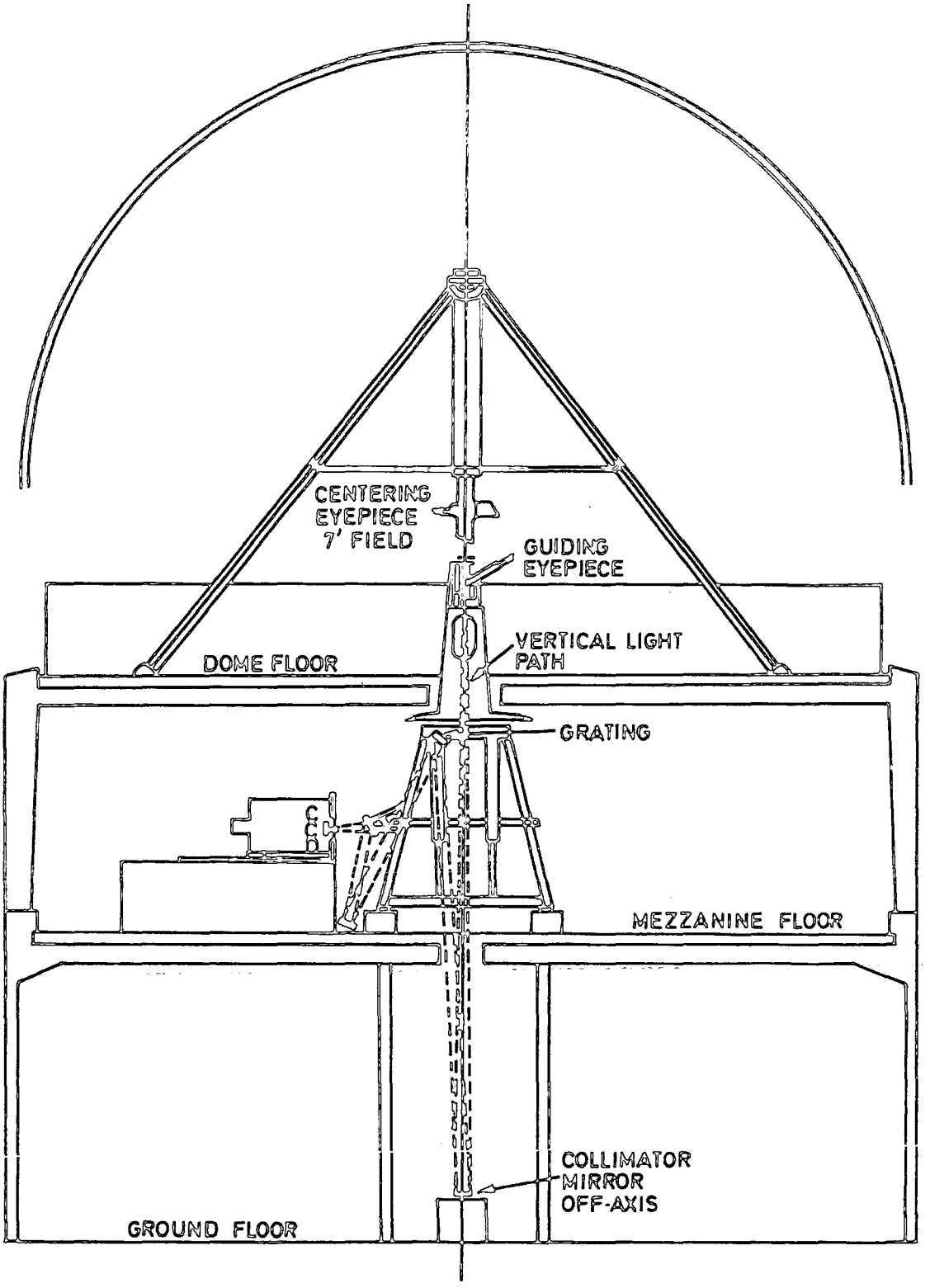

FIG. 4·4·2 COUDE SPECTROGRAPH (view looking north)

region of approximately 69Å. This gives an instrumental resolution of 0.18Å. Normal to the dispersion direction the image scale was 25 μm = 1 arc second at the CCD therefore the spatial resolution was approximately 1 arc second.

4.4.2 Focussing, Aligning and Calibration Operation

Before an observation can be conducted, there are two things that have to be done: firstly, aligning and focussing the CCD, and secondly calibrating the grating angles with the wavelengths of the 1st and 2nd order spectrums of the argon/iron discharge tube. This calibration was necessary because the display unit which indicates the position of the grating angle with respect to the wavelengths of the 1st and 2nd order spectrum, was found to be faulty.

First of all the CCD was placed at the focus of the spectrograph with the slit width wide open, the slit length limited to about 15 pixels (i.e. 15 lines of the CCD) and a tungsten lamp illuminating the slit. The CCD camera was then run and the image displayed on a video monitor. By looking at the image on the screen, the alignment and focussing were carried out. When the tungsten light seemed to fall within 15 vertical lines of the CCD, it was assumed that the CCD had been aligned correctly.

The slit width was then reduced to setting 6(i.e. 150 μm wide) which projects an image size of approximately 25 μm on the CCD. The slit-length was also reduced to 10 pixels. Then instead of the tungsten lamp, the arc source was used to illuminate onto the slit, choosing a strong

arc line and displaying it onto the Tetronix 603 storage scope, a final focussing was done.

When the aligning and focussing of the CCD were satisfactory, the calibration was conducted. This calibration measurement was made by moving the grating angle step by step along the East ⟺ West direction and finding the strong arc line from the blue end onwards upto the red end of the argon/iron spectrum using the appropriate filters. A KG1 and copper sulphate, $CuSO_4$ filters were used to cut out 1st order red, a GG18 filter was employed to cut out 3rd order blue and OG1 filter for cutting 2nd order red (9). The arc lines were displayed onto the 603 storage scope and identified by referring to the arc charts (spectrum of argon/iron of the 30 inch coude taken by photographic plate) and the revised multiplets table by Moore (10). The calibration graph is shown in Figure 4.4.3.

4.4.3 The Operating Procedure of Data Collection.

The observation procedure for collecting astronomical data followed the conventional practice as outlined below. Firstly a frame of an arc source consisting of a few identified arc lines corresponding to the required wavelength range was taken and stored onto the hard disk for wavelength calibration. Whilst there are not many strong arc lines (i.e. the Argon I and Argon II lines from the argon/iron discharge tube used) in the wavelength region of interest, it was decided to look at the strong arc lines in the 2nd order spectrum having

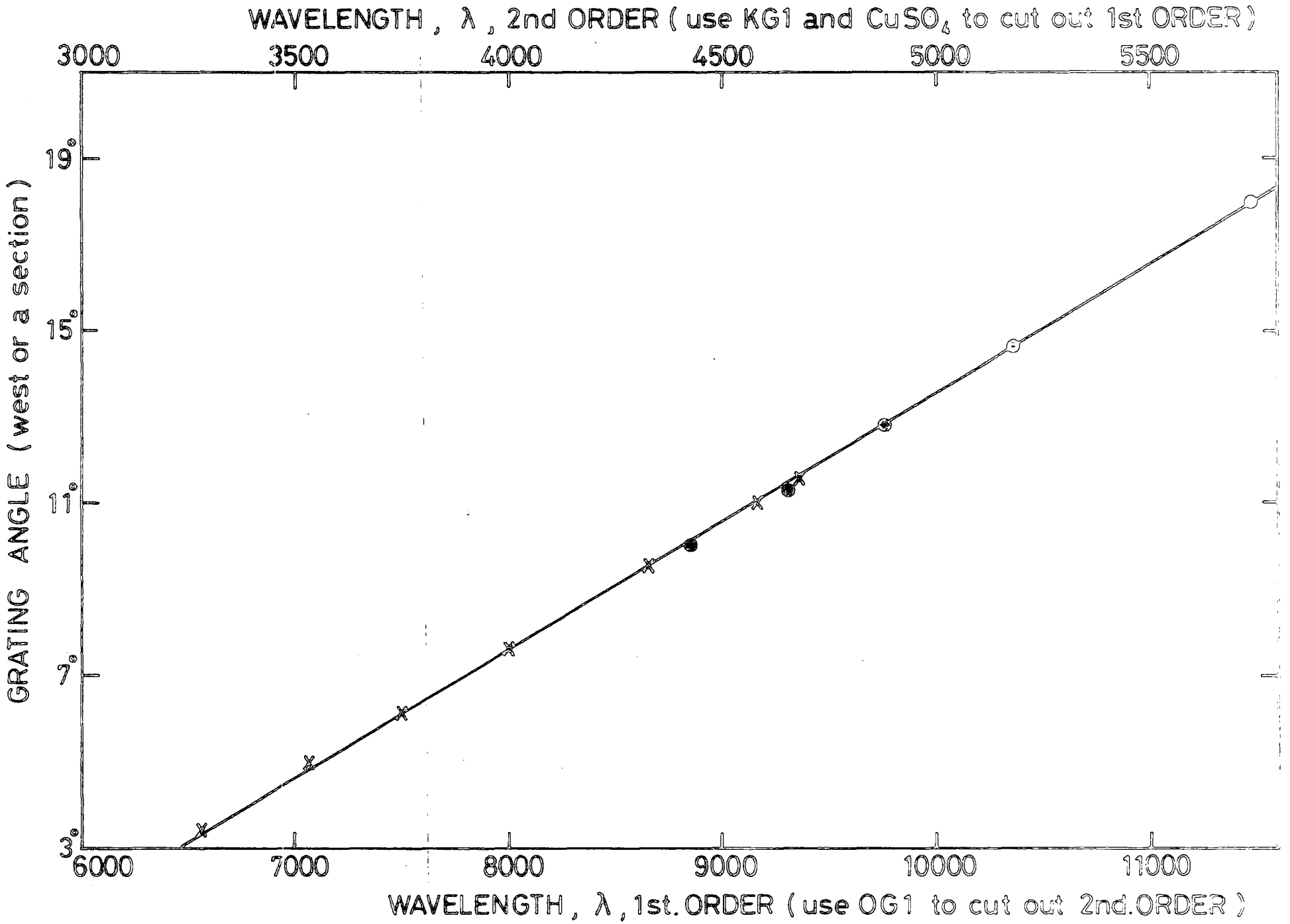
WAVELENGTH , λ , 2nd ORDER (use KG1 and CuSO4 to cut out 1st ORDER)
3000
3500
4000
4500
5000
5500
GRATING ANGLE (west or a section)
19°
15°
11°
7°
3°
6000
7000
8000
9000
10000
11000
WAVELENGTH , λ , 1st. ORDER (use OG1 to cut out 2nd. ORDER)

wavelengths between λ4800Å to λ5100Å. This decision was taken mainly because there are many strong arc lines in this wavelength range and they are easily identified by referring to the arc charts.

The slit width was set at setting 6 (i.e. 150 μm wide) giving a projected image of about 25 micron on the CCD, enough to cover one pixel of the CCD. The length of the slit may be limited through the use of the dekker (prism) mask. In our case, the slit length is limited to 10 pixels. This is chosen, such that only line 5 to line 14 of the image section of the CCD are allowed to be illuminated i.e. collecting signal charge. The arc lines would fall on one of these lines (normally line 6 was chosen) and then the 10 lines are scrunched and stored. However, due to instrumental broadening, we observed that the image covered about 2 to 3 rows of pixels (i.e. light falling on line 5 to line 8 of the CCD).

Next, a frame of M star (HR 5490) was taken and stored. In this observation, the slit-width was opened wide enough to catch all starlight. Widening the slit width results in loss of resolution of the system and cannot be avoided because the "seeing" at R.G.O. is usually poor. This loss in resolution does not severely affect the results because our main concern is to compile an atlas of a star in the wavelength range λ9748Å to λ10153Å by identifying the absorption features present in this wavelength region which

belongs to the star (unless a line profile measurement is to be performed the resolution of the system is less important). The slit length remained unchanged (i.e. 10 pixels in length). The starlight will be collected from lines 5 to 14 and the sky background may be collected on lines 15 to 24 of the image section of the CCD. These collected signals are then read out and stored in the manner described previously. A RG1 (9) filter was used to cut out 2nd order lines.

With the same set-up a frame of hot star (α CrB) were immediately recorded after the M star frame. This is mainly to avoid the problems of air masses. Finally, a flat field frame was taken using the tungsten lamp which is powered by a constant current source to provide stability. Here the slit width was again setting '6'. In the flat field frame, the signal must be about half the value from saturation of the CCD. This is to ensure that all the pixels are biased properly. The whole procedure was then repeated until the seventh frame of M star had been taken and stored.

4.4.4 Problems at the Telescope. During the observational run, we were faced with a few problems as mentioned below. Firstly, the power for the whole CCD camera system is derived from a single 13 amp socket. Obviously running the system from a single socket is not a good practice because the overall performance of the system may be affected by earth loops present between the devices. Nothing

can be done about it except by trial and error in arranging which plugs of the devices should go to which sockets on the extension boards to give minimum pick up from the mains.

Secondly, the aligning and focussing of the CCD at the spectrograph focus. The alignment of the CCD has to be done by either rotating, vertical (upwards) and horizontal (sideways) movements of the whole cooling system (cryostat). Fortunately, the trolley in which the cryostat is set has a vertical and horizontal movement incorporated into it. Therefore our main problem was trying to align the CCD when a rotation movement is required. Focussing the CCD involved the movement of the whole cryostat forward and backward. Therefore it would be helpful, in future to have some form of movement mechanism incorporated in the cooling system such that only the CCD can be moved vertically, horizontally and rotationally rather than the whole cryostat.

Thirdly, it was found that as the grating angle is moved, the image does not fall on the same line of the image section of the CCD as it should do. This is probably due to the fact that the axis of rotation of the grating is not exactly parallel to the direction of the grating rulings. A problem that would not be noticed by photographic plates where the image often has to be artifically broadened in order to be visible. Therefore every time the grating is moved, we have to ensure that the image falls on the appropriate lines of the image section in the CCD.

Finally, and not least, it has been observed that condensation of water vapour occurred at the glass window of the cryostat. A heater in the form of resistors is provided at the glass window to prevent any condensation.

4.5 Summary

A complete operational system with a CCD camera controlled by computer software, using interrupt driven routines has been developed as a general purpose instrument typically for astronomical imaging and spectroscopy applications. The software was developed around RT-11 (i.e. DEC's standard real time operating system) with the FORTRAN programming language for fast readout and data transfer operation. The control program is presented in the form of menu structure mainly to provide the operator information about how the system may be operated and interact with the running program.

A typical astronomical observational operating procedure at a telescope and the problems involved have also been discussed.

REFERENCES

1. Campbell, A.W., (1981), Ph.D. Thesis, University of Durham, England.

2. CATY was originally developed specifically as a CAMAC testing aid at DNPL. It is presently marketed by Francis Golding Associates.

3. Hedge, A.R., (1981), Ph.D. Thesis, University of Durham, England.

4. Barbe, D.F., (1972), "Noise and Distortion considerations in charge coupled devices", Electronic Letter, vol. 8, 207.

5. Heygi, D.J., and Burrows, A., (1980), "Optimal Sampling of charge coupled devices", Astronomical Journal, vol. 85, 1421-1424.

6. Martin, G.P., Ph.D. Thesis, University of Durham in preparation.

7. Fredrick, L.W., (1968), "Spectra at 1 Micron of Planetary Nebulae and Stars Obtained with a Mica-Window Image Tube", Lowell Observatory Bulletin, No. 114, vol. V, No. 8, 149-152.

8. Science Research Council Royal Greenwich Observatory Equatorial Group Facilities Handbook.

9. Catalogue of Colour Filters by Schott, Mainz, Federal Republic of Germany.

10. Moore, C.E., (1945), A Multiplet Table of Astrophysical Interest (N.B.S. Note 17 [Washington, D.C. : National Bureau of Standards]).

CHAPTER 5

CAMERA SYSTEM INSTRUMENTAL EFFECTS AND THE SELECTION OF SUITABLE ASTRONOMICAL OBJECTS

5. INTRODUCTION

The review of infrared spectroscopy by Spinrad and Wing (1) revealed most of the work at 1 micron to have been done on the late-type stars (e.g. K, M, C, S stars etc.) for the purpose of identification of atomic and molecular spectral features of astrophysical interest. Similarly, our survey of infrared spectroscopy over the past decade (1970 - 1979, see Chapter 1) shows more work to have been done, at 1 micron, on late-type stars. This is mainly because of the tremendous improvement in detectors at infrared wavelengths in recent years.

Most of the atomic lines and molecular bands identified in the infrared spectrum (e.g. at 1 micron) become more prominent in cool stars because of reduced ionization and reduced continuum opacity (i.e. the continuum on both sides of the lines or bands is clearly defined), such that they provide a greater number of plausible identifications. Moreover, many molecules which have not been observed in an astrophysical source may become available for study through their infrared rotation vibration bands. From these identifications of spectral features, the chemical abundance of the star, the temperature and luminosity of the stellar atmosphere may be derived. Therefore, the spectral classification is not the primary concern of the author,

whose main objective has been to compile a spectral atlas in the wavelengths interval λ9748Å - λ10153Å and identify the principal spectral features present in the spectra of a M3 giant star, HR5490. Detailed analysis of stellar chemical abundances and spectral classification may be found in the work of King (2).

Since a M3 giant star HR5490 was chosen as the subject for a spectral atlas in the wavelength interval λ9748Å to λ10153Å, this chapter begins with a general introduction to star classification and a description of M stars. Furthermore, because the data collected using the "on-chip prebinning" technique, the general effects of this technique on the observed data will also be considered next. Moreover, the noise of the CCD camera system sets a lower limit to the true signal detectable by the system, i.e. signal-to-noise ratio of unity. Therefore, it is worthwhile mentioning noise sources in our equipment and its effects on the observed data, at this stage.

5.1 The Classification of Stars

Stars are completely gaseous bodies, held together by gravitation and distended by gas pressure and also by the energy of the radiation emitted from their interiors. Some stars may be distorted by the gravitational influence of other nearby stars and also by their own rapid rotations. In these cases the stars may appear slightly aspherical: ellipsoidal, if distorted by external gravitational forces; or spheroidal, if they are flattened by rotation.

It is most probable that all stars increase in temperature and in density from the outside inward. Since the interiors of the stars are hidden from our view by all the gas surrounding them, when we study the light that we get from the stars we are not observing the processes of energy generation directly. What we observe at the outer layer (i.e. the gas surrounding the stellar atmosphere) is merely the final result of the mechanisms of energy transportation outward from the stellar interior. However, the processes of energy generation in the stellar interior may be determined from the information gathered from the outer layer. So far observations of the outer layers of stars have shown them to be made of the same substances that are familiar to us on the earth, and no material has been observed on the surfaces of the stars that cannot be found on earth. Previous observation of the stellar atmospheres has shown that they are often in more or less violent motion, some stars throwing off material steadily or in bursts while others may be accumulating material from their surroundings. These effects may all be seen as necessary stages in their evolutionary paths.

The greater number of the stars in the universe can be arranged in a sequence of decreasing temperature, size and brightness, etc. A plot of brightness against temperature for stars is known today as Hertzsprung-Russell (H-R) diagram as shown in figure 5.1. The stars which mainly lie on a diagonal band from upper left to lower right

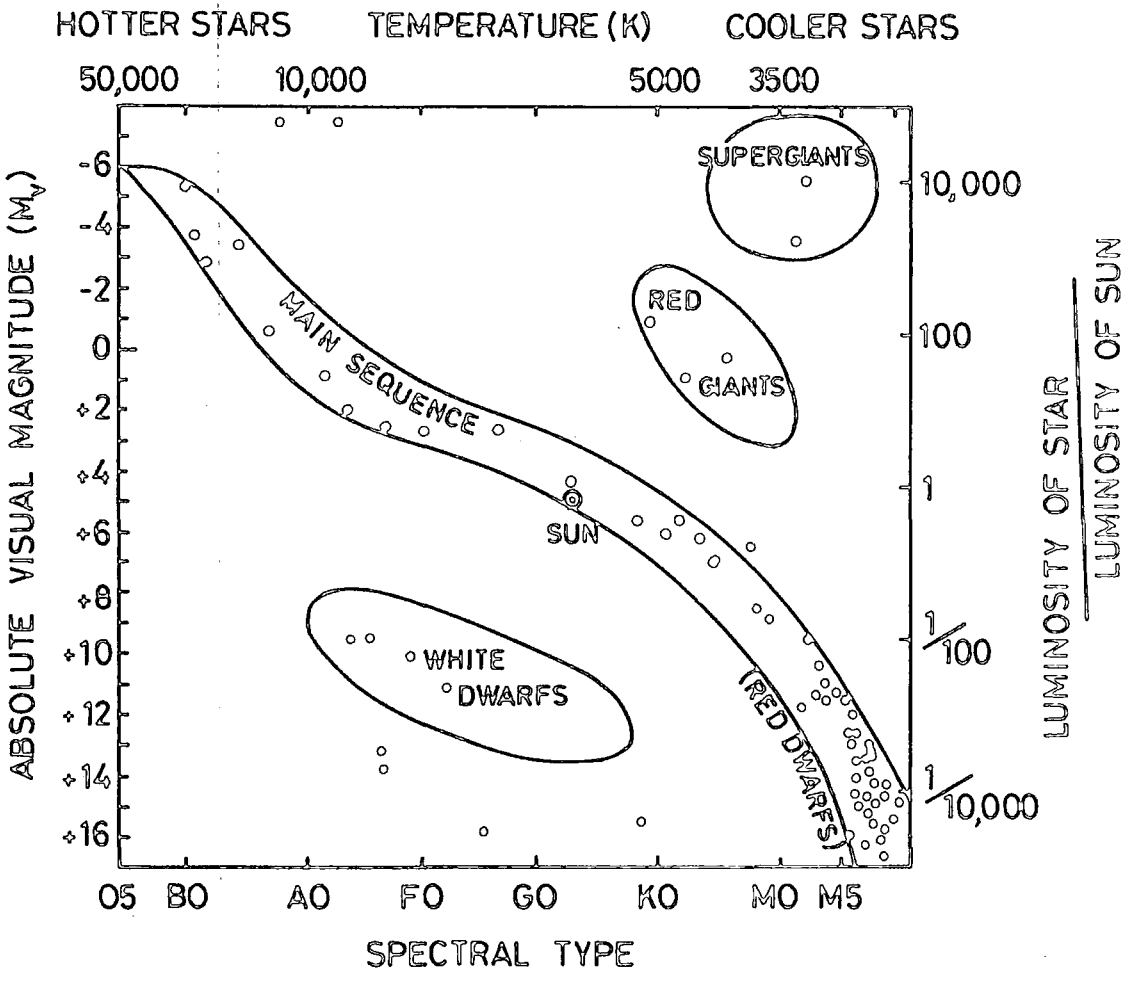

FIG. 5·1 H—R DIAGRAM

(figure 5.1) are called the main sequence in the H-R diagram. These stars are the "normal" stars in the sky (i.e. follow certain relationship between brightness and temperature). The sun belongs to this family of stars. The luminous stars that lie above and to the right of the main sequence in the H-R diagram are called "giants". Even less common are the enormously luminous and distended stars - the "supergiants". The discovery of a group intermediate between giants and main sequence in the H-R diagram, the "subgiants", is due to finer classification of stellar brightness and sizes. The faint stars near the bottom and in the lower-left corner of the H-R diagram are called the white dwarfs. The giants, supergiants, subgiants and white dwarfs appear to be "abnormal" stars, with a completely different connection between brightness and temperature. In figure 5.1 note that since H-R diagrams were sometimes originally plotted by spectral type, from O to M, the hottest stars are on the left side of the graph. Here the temperature of M-type stars ranges from 3500°K down to 2000°K. The evolution of stars, properties, classification, etc. are widely covered in the literature and will not be detailed here.

5.2 The M-Type Stars

As can be seen in the previous section the temperature of these stars ranges from 3500°K down to 2000°K. Therefore, they may be said to be the coolest stars in the standard classification list. However, there are much

cooler stars in existence but their discovery is a relatively recent event in the history of astrophysics, coming as a result of the improvement of detector sensitivity in the infrared region. These very cool stars emit practically no energy at all in the visible region of the spectrum, most of their energy being emitted as infrared radiation, and hence are referred to as "infrared stars".

Since the temperature of M-type stars is so low even the relatively weak bonds holding together the atoms in a molecule can be retained. When molecules are present in a stellar atmosphere, an absorption spectrum quite different from the spectrum produced by a single atom may be formed. This absorption spectrum is characterized by many finely spaced lines crowded together into a band of wavelengths, which is typical of a molecule. This type of spectrum is called a "band spectrum". The bands in a molecular spectrum may be explained as follows. When atoms are held together in a molecule, the electrons of these atoms may absorb photons and be excited to higher orbits, just as electrons do on an individual atom. Such a transition should produce one absorption line at a wavelength characteristic of the molecule involved resembling the absorption line of an atom. The reason that the spectra of molecules contain dense bands of lines is that a molecule, unlike an atom, has a complicated structure consisting of several individual atoms that make up the molecule. This structure can rotate in space and also vibrate in and out. As an electron

in a molecule is excited from one orbit to another, the molecule may change its rate of rotation or rate of vibration at the same time as the electron makes its transition. When the molecule's rotation or vibration changes, its energy also changes by a small amount. The difference in energy from one type of rotation of the molecule to another, or one kind of vibration to another, is quite small in comparison to the difference of energy involved in the jump of an electron from one orbit to another. As a result of these small differences, the energy of the electron's transition is separated into many closely-spaced energies, and the wavelength of the line accordingly is spread out into a large number of finely spaced lines covering a band of wavelengths, and this group of finely spaced lines is the band spectrum of the molecule.

The most intense band spectrum to exist in the spectra of stars is the band spectrum of Titanium oxide (TiO). The two atoms in the TiO molecule - Titanium and Oxygen - are very tightly bound to one another, and therefore this molecule exists in the outer layers of stars before any other type of relatively common molecule can do so. Therefore, the appearance of strong absorption bands of Titanium oxide in the spectrum of a star is the criterion used by astronomers to separate M stars from hotter stars. In cooler M stars, molecular bands of Titanium oxide and Vanadium oxide (VO) are extremely strong, the lines of neutral atoms (e.g. Titanium) are even stronger than at

class K, lines of hydrogen if present being very weak.

5.3 The Requirement of Compilation of Spectral Atlas of M Giant

The appearance and absolute strengths of near infrared Titanium oxide (TiO) and Vanadium oxide (VO) bands obtained from lower dispersion spectra of M stars were used by Nassau (1956) (3) and by Sharples (1956) (4) as criteria for spectral classification. Similarly, Keenan (1963) (5) has made spectral classification criteria based on relative strengths of various TiO and VO bands in moderate dispersion spectra of stars in the blue and visible regions. Finally, for the M sequence of spectral types, Lockwood (1973) (6) has made a classification based on TiO alone from MO to M5, on TiO and VO from M5 to M8, and on VO alone from M8 to M10. However, such classification will depend on the chemical abundances of Ti/V ratio in M stars, because any variation in this ratio could cause serious distortions in the sequence of spectral types. Therefore it would be more appropriate to use the same molecule (e.g. TiO) to define the entire temperature sequence in M stars. The excellent temperature sensitivity of TiO has been effectively used as the basic MK classification criterion for M stars. Wing et al. (1979) (7), has shown the classification of late-type stars by photoelectric measurements of TiO bands to be quite precise, and the recent work of Ridgway et al. (1980) (8) in calibration of the effective temperature spectral class relationship for K and M giants should now allow a

direct determination of effective temperature from TiO band strength measurements.

In the past two decades there has been much spectroscopic work of the relative abundances of the elements in the stellar atmospheres of stars representing major sections of the H-R diagram, but the cool stars of types M and S have seldom been observed for abundance work. The main reason for this lack of activity is the difficulty in finding unblended atomic lines and molecular bands in the spectra of cool stars, e.g. M stars. Recently, with the improvement of infrared detectors, the interest of investigating chromospheres of cool stars (e.g. constructing a realistic model of the atmosphere of cool stars) has been stimulated by astronomers. Currently, infrared spectroscopy may be used to investigate chromospheres of cool stars and is more convenient and far less expensive than for ultraviolet observations. Furthermore, the availability of unblended high-excitation lines of abundant neutral atoms and clear continuum in the infrared spectra of M stars are the key to the partial success of infrared spectroscopy.

The purpose of the present investigation was to compile a spectral atlas of one bright M3 giant in the wavelength region λ 9748Å - λ10153Å, thereby exploiting the useful spectral response of a CCD based detector system. This type of star was chosen since cool stars are brighter in the near infrared and have less line-blending than in the visible. A further objective was to identify the neutral

lines and molecular bands present in the spectra mainly involving the element Titanium (Ti). The wavelengths of interest are of course, well within the "window" in the telluric water absorption which exists between about $\lambda 9800\text{A}^{o}$ and $\lambda 10900\text{A}^{o}$.

The M3 giant star HR5490 was chosen for this work for the following reasons: (i) no spectral atlas of this star existed in the wavelength region around 1 micron; (ii) this star should be bright at 1 micron (i.e. V-I = 2.5 magnitude) and suitable for observation with a CCD camera system at the 30" coude telescope at R.G.O. and (iii) very importantly, there is a hot star close to it differing only by 50 minutes R.A., thus providing a calibration star with almost identical air mass.

Because the grating of the spectrograph at the telescope is blazed at 10000A^{o} for spectra in the first order and has a dispersion of about 8.6A^{o}/mm, the spectra obtained with this spectrograph will be considered as a high dispersion spectra. With such dispersion, the fine atomic and weaker molecular features may be revealed in the spectra without much difficulty. If possible, a signal-to-noise ratio of approximately 100 is ideally required for our measurements, long integration times would normally be necessary using the coude system available, however, it was hoped that the use of a novel pre-binning technique possible with the CCD would reduce the exposure time required to achieve an acceptable signal-to-noise ratio. This technique will be discussed in the next

section. The comparison between our spectral atlas of an M3 giant star HR5490 with other spectral atlases of various spectral types will be given in chapter 6.

5.4 On Chip Prebinning Technique

In the previous chapter, it was mentioned that the CCD readout operates by shunting the signal, line by line, down the array. At the base of the array is an extra line called the readout register. As a line is shunted into it the signal in each pixel is sensed and discharged before the next line comes in. If, however, the readout part of this sequence is stopped for a time, signals in each column will accumulate in the readout register. The advantage of shunting a number of rows of signal charges into the readout register is that this effectively sums the signals in a particular column on-chip before they are read out. Assuming that the final readout charge sensing process contributes a fixed amount of noise, which is independent of signal level, the overall signal to noise ratio may be improved by on-chip summation of columns. Improving the signal-to-noise ratio in this way may in some situations reduce the lower limit to the detectable signal, since at very low light levels the readout noise will dominate the photon shot noise. All that 'pre-binning' loses is some information about the intensity variation of the spectrum in a direction perpendicular to the dispersion. This information is only of interest from an instrumental point of view and the signals in each column must eventually be added together anyway, for analysis purposes, even when rows are read individually.

The seeing at the R.G.O. in May 1982 must be classed as 'poor'. During our observation the seeing varied between 3 to 5 arc sec. which greatly reduced the optimum signal-to-noise ratio obtainable. Using the novel technique of on chip 'pre-binning' when reading out the CCD provided marked improvement of the signal-to-noise ratio.

The effect of the improvement of signal-to-noise ratio on our data could be demonstrated by observing a suitable stellar feature for measured times but because of the lack of reasonable seeing conditions at R.G.O. for even one night and limited telescope observing time this measurement was not carried out. However, theoretical explanation of how the on chip pre-binning method affects the observed data will now be given. Figure 5.2a, b, c, d, e and f illustrates how this work. Figure 5.2(a) shows the pixel mosaic of the CCD. Note that there are no gaps between the pixels where light can be lost. Figure 5.2(b) shows, using a simplified approach, how the image of a stellar absorption feature would fall on the CCD if the seeing was perfect and the slit-width less than 0.1Å. The spatial width of the image is due to instrumental broadening and the spectral width is the inherent line width of the star, typically 0.5Å. Figure 5.2(c) shows how the same stellar feature would appear with a seeing disc of 5 arc sec. Both spatial and spectral resolution are lost. In figure 5.2(d) the graph shows how a plot of the signal collected in line X would look with perfect seeing. Figure 5.2(e) shows the plot of line X for a seeing disc of

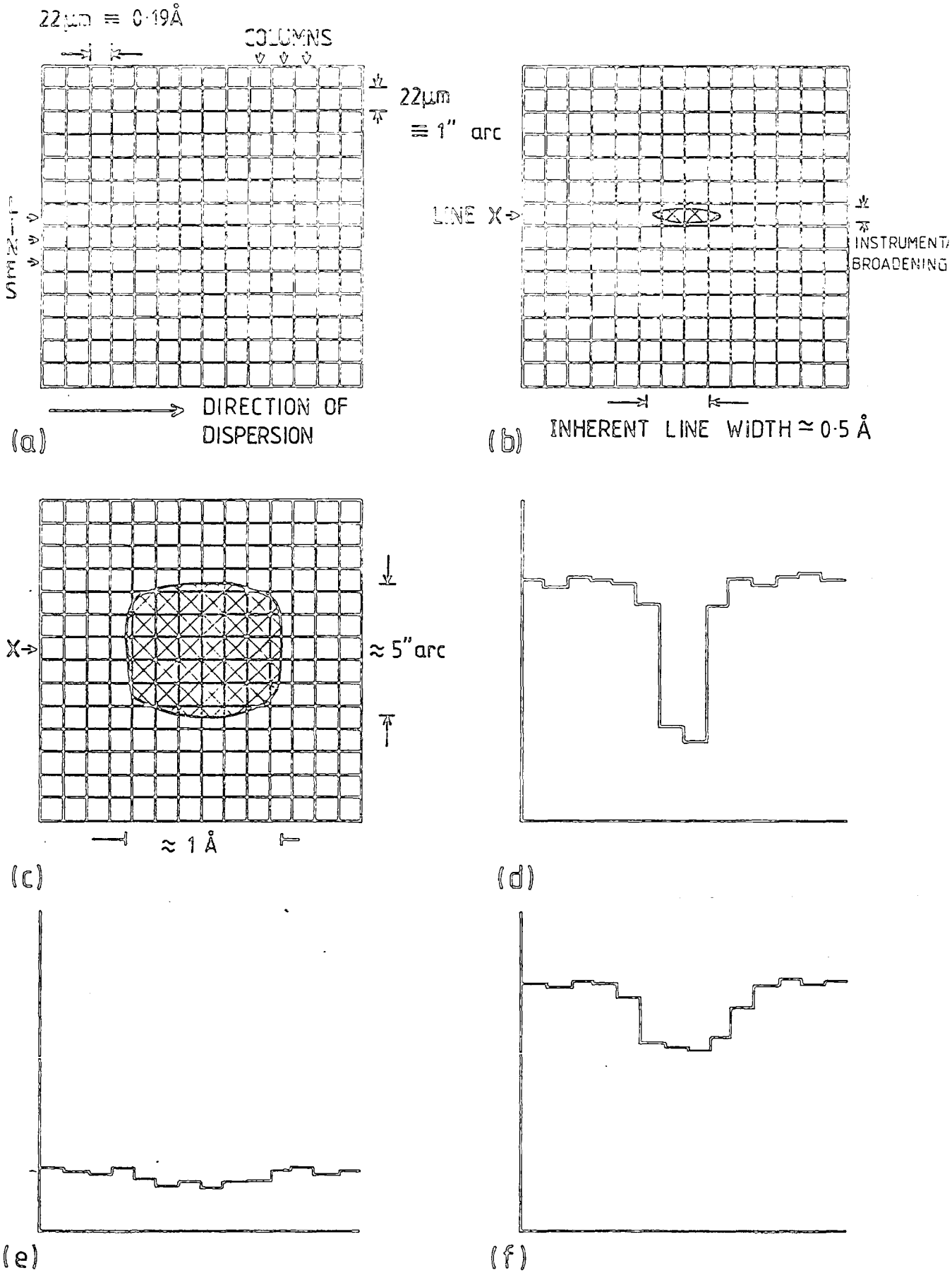

FIG. 5·2 PRE-BINNING WITH A C.C.D.

5 arc sec. In the graph of figure 5.2(f) the signal has been pre-binned from line (X - 5) to line (X + 5). Note that the area associated with the absorption feature is the same in figure 5.2(f) as it is in figure 5.2(d).

No doubt using this technique we tend to lose the system resolution but a high signal-to-noise ratio may be achieved with shorter exposure time. Moreover, our observed data may have less chance of being hit with cosmic rays because of the shorter exposure.

5.5 Noise Consideration of Observational Data

The sources of noise are many and may be classed into one of the three categories: (i) instrument or equipment noise; (ii) photon noise in the starlight; and (iii) photon noise in the sky background. The combined fluctuations in output because of the unavoidable sources of noise in categories (ii) and (iii) represent a theoretical minimum against which we compare our equipment. It is possible that the equipment noise may come within a few percent of the theoretical minimum value under favourable conditions. However, if a system shows 2 or more times the theoretical value then it needs some attention.

Photon noise originates from the random arrival of the photons and is described by Bose-Einstein statistics by the equation (5) given below

$$\Delta n = n^{1/2}\left[1 + \frac{1}{\exp^{h\nu/kT} - 1}\right]^{1/2} \qquad (5.1)$$

where Δn is the mean square fluctuation,

n is the number of photon arrivals,

h is the planck constant,

ν is the frequency of photons,

k is the Boltzmann constant, and

T is the temperature of the source.

Equation (5.1) holds for thermal sources, and for non-thermal sources, a slightly different relation may hold (see Smith et al. 1957(6)). For most cases, generally $h\nu$ (the energy of the source) is considerably greater than kT, thus equation (5.1) reduces to

$$\Delta n = n^{1/2} \tag{5.2}$$

Similarly, the fluctuations in the output due to equipment noise may also be considered to be random events and therefore describable with Poisson statistics as represented in equation (5.2), such that the value of n is equivalent to the number of detected photons that would cause the same noise.

The total signal detected by our system can be expressed by the equation given below,

$$n = (S + B)t \tag{5.3}$$

where S is the rate of photon counts for the starlight,

B is the equipment noise and other background (e.g. sky, cosmic rays, etc.), and

t is the integration time.

From equation (5.3), the signal detected from the star may be given as

$$St = n - Bt \tag{5.4}$$

Defining N = St and b = Bt, substitute in the above equation gives

$$N = n - b \tag{5.5}$$

The statistical uncertainty in the above equation may be given as follows

$$\Delta N = (\Delta n^2 + \Delta b^2)^{\frac{1}{2}} \tag{5.6}$$

where ΔN, Δn and Δb are the standard deviations of N, n, and b respectively. A fractional error of the detected signal may be obtained by first dividing equation (5.6) with N and then substituting equations (5.2) and (5.3) into the equation giving

$$\varepsilon = \frac{\Delta N}{N} = \frac{(n+b)^{1/2}}{N} = \frac{[(S+B)t + Bt]^{1/2}}{St} = \left[\frac{1 + 2B/S}{St}\right]^{1/2} \tag{5.7}$$

Equation (5.7) is fundamental because the fractional error in the detected signal is determined by the background counts, light counts and integration time. For cases where B/S << 1 then $\varepsilon \approx (St)^{-\frac{1}{2}}$, which is pure signal photon noise and the case B/S >> 1, gives $\varepsilon \approx [(2B/S)/St]^{\frac{1}{2}}$. It is clear for the two cases above ε may be reduced if the integration time t is made very long. However, ε can also be reduced in the second case (i.e. B/S >> 1) by using a larger telescope, a detector with high quantum efficiency, cooling the detector or decreasing the non stellar photons from the sky and

elsewhere. In our case, the sky background can be considered negligible for coude slit spectroscopy. Therefore the main background noise in our data must come from the CCD camera system.

5.5.1 Noise Measurement of CCD Camera. Theoretically, the total noise of the CCD detector may be expressed by the equation (7) given below,

$$N_{tot}^2 = \alpha N + \sigma_o^2 + \sigma^2(s) + \sigma^2(I) \qquad (5.8)$$

where N_{tot} is the total noise,

α is the responsive quantum efficiency (RQE),

N is the total number of incident photons,

σ_o is the readout noise, independent of signal,

$\sigma(s)$ is the readout noise dependent on integrated signal, and

$\sigma(I)$ is the readout noise dependent on incident illumination.

However, if these noises may be separated entirely into shot noise and a signal independent readout noise, this gives

$$N_{tot}^2 = \sigma^2 electrons^2 + \alpha N \qquad (5.9)$$

The above equation can also be represented as a noise voltage at the output:

$$V_n^2 = G^2(\alpha N + \sigma^2) \qquad (5.10),$$

where G is the output per detected photon, and

σ is the root-mean-square (RMS) readout noise in electrons. Since GαN is equivalent to the mean signal voltage V_s, equation (5.10) becomes

$$V_n^2 = GV_s + G^2\sigma^2 \qquad (5.11)$$

Therefore measuring the mean square noise voltage as a function of signal should yield an accurate value of G, the output per detected photon. Knowing the value of G and the noise voltage at zero incident signal, the r.m.s. readout noise in electrons may be found from equation (5.11).

A measurement has been made of the mean square noise voltage, Vn^2 as a function of the signal with the same experimental set-up used for obtaining the M star data (i.e. at telescope). Thus, the results obtained from this experiment may be directly applied to the full observing program.

In this measurement a stabilised tungsten light source and a set of neutral density filters are used to provide different light intensities incident on the CCD while the integration time remains fixed. Multiple frames are taken at each light intensity and a variance calculated for each pixel. The variances are plotted against the mean signal detected. Since the variance (measured in output units (ADU)) is proportional to the average number of electrons per pixel, the slope of this curve calibrates the output in

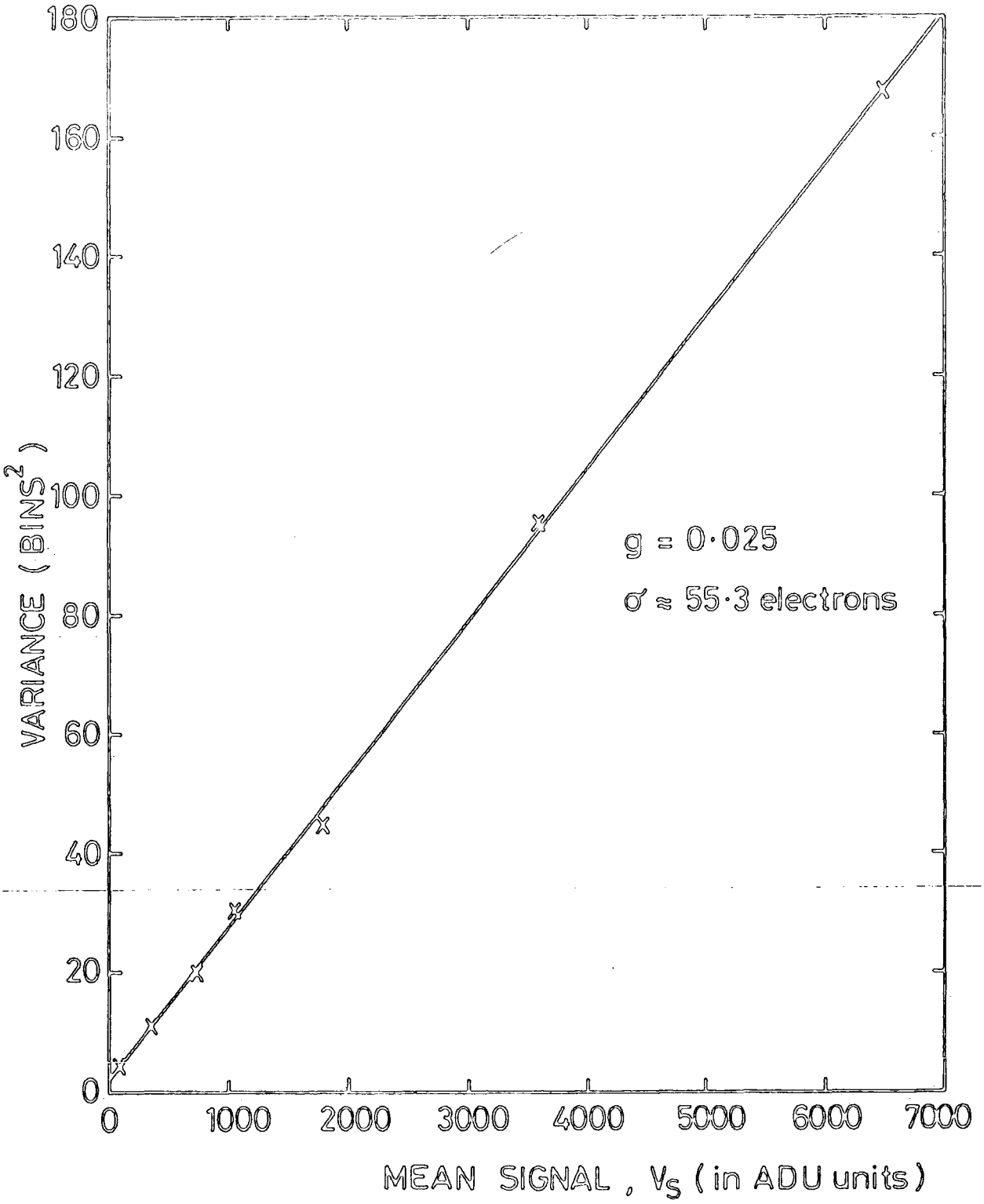
180
160
140
120
100
80
60
40
20
0
VARIANCE (BINS^2)
0
1000
2000
3000
4000
5000
6000
7000
MEAN SIGNAL , V_S (in ADU units)
g = 0·025
σ ≈ 55·3 electrons

FIG. 5·3 (a)

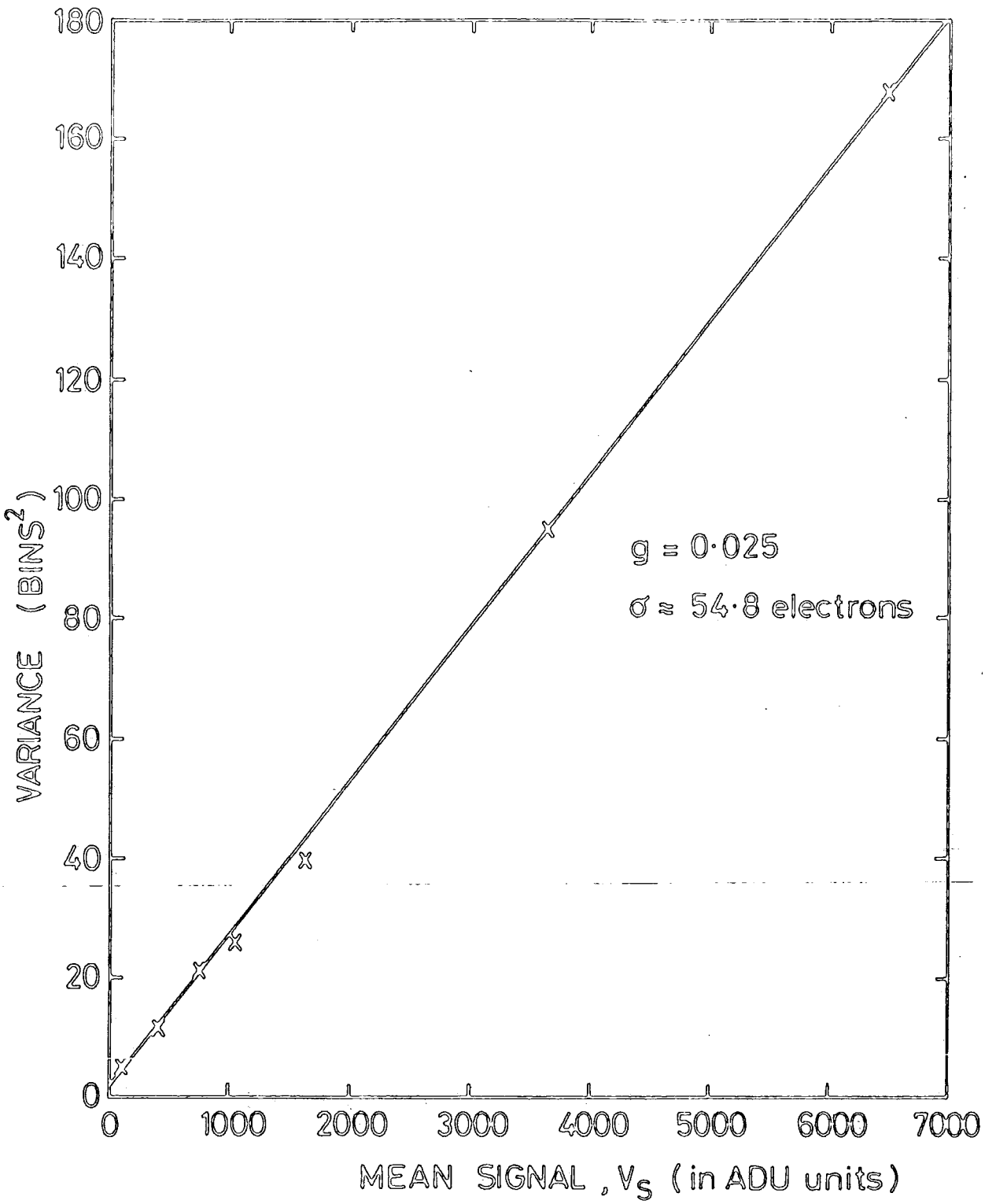
180
160
140
120
100
80
60
40
20
0
VARIANCE (BINS^2)
0
1000
2000
3000
4000
5000
6000
7000
MEAN SIGNAL, V_S (in ADU units)
g = 0·025
σ = 54·8 electrons

FIG. 5·3(b)

"number of electrons". The intercept of the curve gives the readout noise. Typical results for square noise voltage as a function of signal are calculated from Figures 5.3a and b. The slope G is found to be approximately 0.025 and the readout system noise σ is about 55 electrons. This value is used in determining the signal-to-noise ratio of our observed data as given in table 6.1.

REFERENCES

1. Spinrad, H., and Wing, R.F. (1969), "Infrared Spectra of Stars", Annual Review Astronomy and Astrophysics, No. 7, 249-299.

2. King, R., Ph.D. Thesis, University of Durham (in preparation).

3. Nassau, J.J. (1956), "Objective Prism Spectra of Relatively Cool Stars in the near Infrared", Vistas Astronomy vol. 2, 1361 - 1368.

4. Sharples, S. (1956), "The Infrared Spectral Classification of M-type Stars", Astrophysical Journal, 124, 342 - 345.

5. Keenan, P.C. (1963), "In Basic Astronomical Data, 2ed. K.Aa. Strand (Chicago : University of Chicago Press), p.78.

6. Lockwood, G.W. (1973), "Scanner Photometry of Weak TiO Bands Near 1 Micron in Cool M Stars", Astrophysical Journal, 180, 845 - 855.

7. Wing, R.F. (1979), "In Spectral Classifications of the Future", IAU Colloqium No. 47, edited by M.F. McCarthy, A.G. Davis Philip, and G.V. Voyne (Vatican Observatory, Vatican City), p.347.

8. Ridgway, S.T., Joyce, R.R., White, N.M., and Wing, R.F. (1980), "Effective Temperatures of Late-Type Stars : The Field Giants from KO to M6", Astrophysical Journal, 235 : 126 - 137.

9. Felgett, P.B. (1955), Vistas in Astronomy, Vol. 1, A. Bear, Ed. Pergamon, London.

10. Smith, R.A., Jones, F.E., and Chasmar, R.P. (1957), "The Detection and Measurement of Infrared Radiation", Oxford 1968, P.209.

11. Campbell, A.W. (1981), Ph.D. Thesis, University of Durham.

CHAPTER 6

DATA REDUCTION AND ANALYSIS

6. INTRODUCTION

The data obtained during the observational run at the 30 inch reflector telescope at R.G.O., with the CCD camera, was stored on Magnetic tape for the purpose of later reduction and analysis work applicable for astronomical spectroscopy. The main aim of this chapter is to describe in detail the processes employed in reduction and analysis of the observed data, in order to form the spectral atlas of the M star HR 5490 in the wavelength region λ 9748$\AA$ - λ 10153$\AA$. The result is then compared with other spectral atlases of cool stars available at 1 micron and also the solar spectra. The data reduction and analysis work was done using the starlink node (VAX 11/750 computer) at Durham (to be described briefly in the next section).

This chapter comprises a brief account of the starlink node, and the data reduction and analysis work necessary for astronomical spectroscopy.

6.1 The Starlink Node

Starlink is a computing facility for the use of United Kingdom astronomers primarily for the reduction of observational data, with the emphasis on interactive processing. The image and data processing facilities are provided by the Science Engineering Research Council (SERC). At present

Starlink is based on eight computers, six VAX 11/780s and two VAX 11/750s. The VAX 11/780s are located at Rutherford Appleton Laboratory (RAL) at Chilton, University College London, Cambridge University, Manchester University, the Royal Observatory of Edinburgh (ROE) and the Royal Greenwich Observatory (RGO) at Herstmonceux. The VAX 11/750s are located at Durham University and Birmingham University.

The Starlink installed at Durham University in April 1982 is the seventh node to be added to the network in the United Kingdom. The system comprises a VAX 11/750 and an image display unit - the Advanced Raster Graphics System (ARGS) manufactured by Sigma Electronics. At present the Durham system as configured, tentatively includes three disc drives totalling 636 Mbyte storage and one fast (125 ipc) tape drive.

A standard set of astronomical software (the Starlink software collection) is provided by the SERC. The major items of the Starlink software collection available on the Durham System are the following:-

(a) SPICA (system programmable interactive computer analysis) - A Spectral data reduction system or package;

(b) ASPIC (Astronomical Picture Processing) - An image processing package;

(c) GKS/HIGR (Graphic Kernel System) - A standard graphics software package; and

(d) CHART - A program for producing star maps, finding charts etc. (1).

From the above items SPICA has been extensively used for reduction and analysis work on our observational data. Therefore, a few points about SPICA are worth mentioning here. SPICA is a complete data reduction and analysis system designed for the spectroscopist with either 1-dimensional (1D) or 2-dimensional (2D) spectra. It has its own data structure, programmable command language and set of 'functions'. This enables the user to run a batch job as well as working interactively with the machine. As a simple example, suppose a user has a file 'CLEAN FOR' in directory (MZZ. SPICA) containing a set of SPICA commands 'cleaning' the raw data as follows:

```
PROC CLEAN
STAR IN M STAR DATA       ; Data is put on the 2D stack,
EXTRACT 4, 4              ; Data on 2D stack at cross-section
                            4 is put on 1D stack,
1ST 1                     ; stored the extract data in memory
                            record 1,
1 BPL SC = 16             ; Plot the data with maximum scale
                            (y-axis) 16000 counts,
ERASE                     ; Clear the screen, i.e. the graphic
                            plot memory is erased,
STAR IN FLAT FIELD DATA   ; Data is put on the 2D stack,
EXTRACT 4, 4              ;
1ST 2                     ; Stored the extract data in memory
                            record 2,
```

```
1BPL SC = 16          ;
1 RCL 1               ; Recall the memory content in record 1
                        to the top of 1D stack,
1 SW                  ; Swop the M star data with the flat
                        field data,
1 DIV                 ; Divide M star data with flat field data,
1 BPL SC = 16         ; Plot the result.
END PROC.
```

The above command procedure will be executed as a batch job when the command 'BATCH CLEAN' is issued by the user. This allows long jobs to be initiated and frees the terminal for further input while the job is being executed, thus saving terminal time.

The programs in SPICA may be easily altered to serve the requirements of the user. Furthermore, at the end of every session with SPICA a file called 'LOG TXT' will appear in the user directory. This file contains a complete log of the session. The SPICA system runs best with the dual graphics/alpha screen of the SIGMA terminal particularly for displaying 1D spectra, and to display 2D spectra effectively makes use of the ARGS. The disadvantage of SPICA is that it has an integer data format, thus all arithmatic operations are performed in integer mode.

6.2 Data Reduction

The astronomical data collected in May 1982 at the 30 inch reflector telescope and stored on magnetic tape

comprises seven frames each of the M star, HR 5490, the hot star, αCrB, the calibration source - Argon/Iron arc and the flat field source tungsten. The seven overlapping frames of the M star, HR 5490, and the hot star, α CrB are listed in Table 6.1. Each frame, taken in the first spectral order, covered approximately 69Å of the spectrum and there was about 10 per cent overlap between each frame (i.e. between M star frame). The 10 per cent overlap between each frame is necessary in order to certify that the collected or recorded data is in the correct frame. Thus the seven frames included a region of approximately 400Å. Each frame was exposed for 3000 seconds and colour filters were used to cut out the 2nd order spectrum in the region of 5000Å. This was especially important for the hot star α CrB which is relatively bright at 5000Å.

The signal-to-noise ratio of the data collected varies from about 50 to 100. There are two factors which cause the variation, firstly the seeing conditions at RGO are not constant, and secondly, the quantum efficiency of the CCD decreases significantly beyond 1 micron. Because of the newly installed Starlink node in Durham an immediate reduction procedure could be applied to the data using the SPICA reduction package. The reduction procedure is outlined in the following. The seven frames of the calibration source Argon/Iron arc are processed using the "ARC" wavelength calibration routine in the SPICA reduction package. This routine enables the user to interact with the computer i.e. to select an arc line with the cursor

TABLE 6.1

SUMMARY OF OBSERVATION

Exposure time = 50 minutes

Mean Wavelength Å	S/N of Continuum for HR 5490	S/N of Continuum for α CrB	No. of Stellar features in HR 5490
9783.3	75	40	7
9839.5	47	36	2
9897.4	98	81	1
9958.6	76	46	4
10005.1	80	74	5
10065.0	71	52	7
10118.4	49	41	4
			Total = 30

and provide a wavelength value for the selected line (the frame of arc lines is displayed on the terminal screen). The selection of lines can be made manually or automatically, but in our case the manual mode is preferred. When the selection process is complete, a third order polynomial fit to the arc lines is made. This order of polynomial gives a good relation between wavelength and pixel, or channel number, with no systematic error in the residuals. This relationship is displayed on the terminal screen with the information such as the dispersion, start of wavelength, central wavelength and end of wavelength for the frame of arc lines. The list of arc lines may be stored in a file called 'CFILE' (coefficient file). However, this list may be edited if the user wishes to include a few more identified arc lines within the frame by using the 'ARCEDIT' command.

Finally, the seven frames of the calibration source - Argon/Iron arc have been wavelength calibrated based on the known comparison lines (from the table of Argon/Iron source taken with photographic plate on the 30 inch coude by RGO) and stored in a file. The average departure of the comparison lines from the cubic fit varies in the range between 0.2 to 0.3Å.

For each star frame taken, the raw data was 'cleaned' by dividing it with the flat field frame of the tungsten lamp which removes the pixel to pixel sensitivity variations of the CCD. Matching M star, HR 5490 and hot star, αCrB

frames are then brought to the same continuum level and divided to leave just the true stellar features of the M star. In order to restore the continuum level of the M star, HR 5490 during division, the continuum of the hot star is first normalised by using the curve fit (CFIT) routine in SPICA. This is essential as can be seen from the Plank black body radiation equation and the Wien's law below (2).

$$I_\lambda(T) = \frac{2hc^2}{\lambda^5}\left[\frac{1}{e^{hc/\lambda kT} - 1}\right] \qquad (6.1)$$

and

$$T = \frac{2{\cdot}89 \times 10^7}{\lambda_{max}} \qquad (6.2)$$

where $I_\lambda(T)$ is the intensity of the continuum of a black body source,

h is the planck constant,

c is the velocity of light,

k is the Boltzmann constant,

λ is the wavelength, and

T is the temperature.

The above shows that the continuum is found to depend only on wavelength and the temperature of the black body. Furthermore, the intensity of a black body spectrum has its peak at a certain wavelength, i.e. maximum wavelength, λ_{max}. Thus the spectral shapes of the M star, HR 5490 and the hot star, α CrB can be represented typically as

in Figures 6.1a and b by using equations (6.1) and (6.2), i.e. assuming they behave as a black body source. Comparison of the two spectral shapes shows that the hot star frame must be normalized in order to restore the continuum level of the M star.

Figures 6.2a, b, and c show the raw data of the M star, HR 5490, the hot star, α CrB and the final spectra respectively of the first of the seven frames taken. Close inspection of the above figures show how weak stellar lines hidden in the original frame have appeared. The processed spectral frame was then associated with the corresponding wavelength calibrated frame so that the position of stellar features may be identified in terms of wavelength. The positions of stellar features may be identified to about 0.2Å, and this is our optimum accuracy for the M star. However, since each feature is due to several instrumentally broadened (mainly due to slit-width) overlapping stellar lines, the final agreement between stellar and laboratory wavelengths is no better than the resolution of the instrument.

Estimates of the equivalent widths of the stellar absorption features have also been made using the equivalent width 'EW' routine in SPICA. This routine integrates the area of the absorption feature between the two chosen continuum points estimated by eye and therefore is to be regarded only as an approximate guide to the real or true equivalent width. If the observed spectral feature was usually sharp, broad, or blended, this fact will be noted

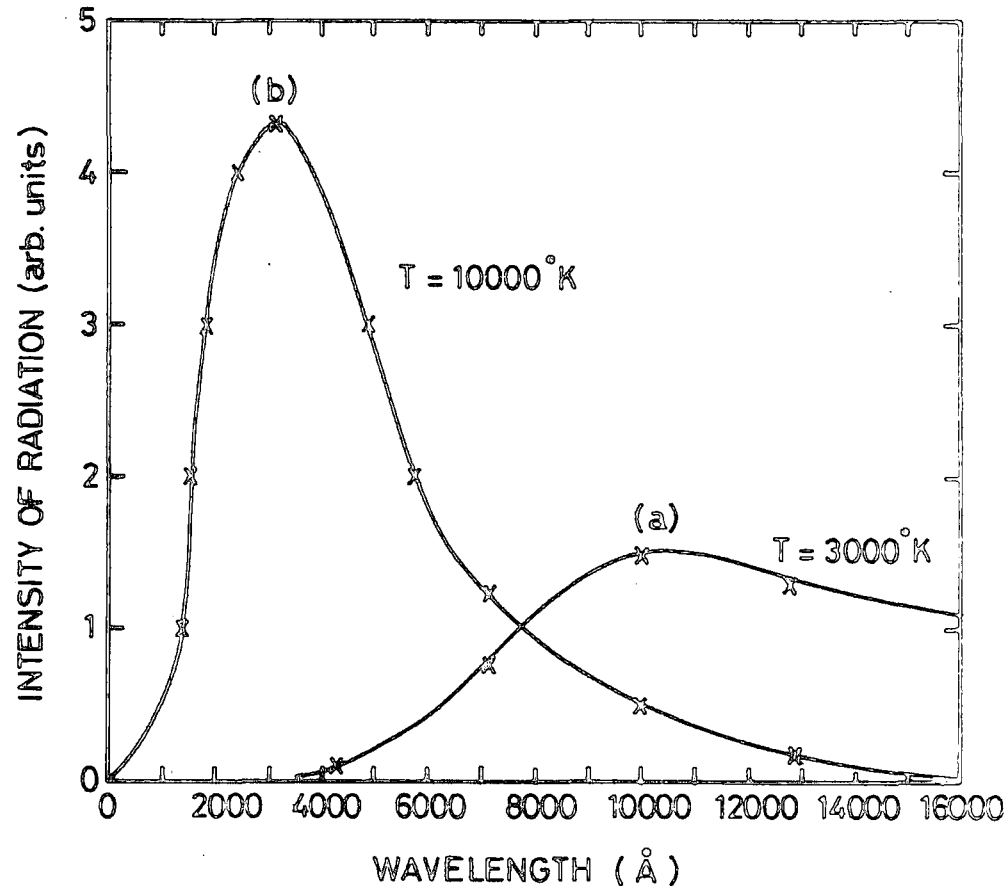
INTENSITY OF RADIATION (arb. units)
WAVELENGTH (Å)
(b)
T = 10000°K
(a)
T = 3000°K
0
1
2
3
4
5
0
2000
4000
6000
8000
10000
12000
14000
16000

FIG.6·1 a,b

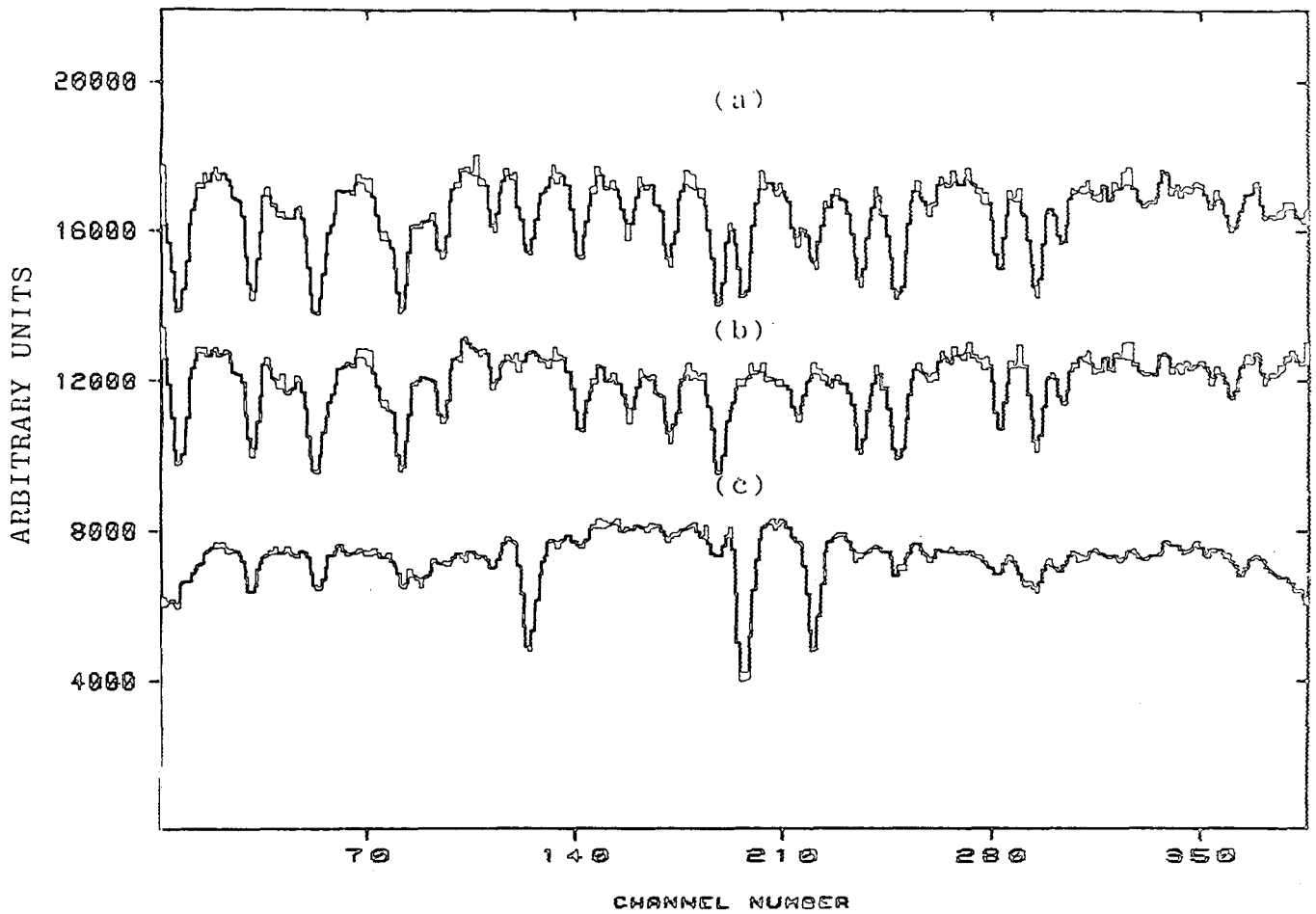
20000
16000
12000
8000
4000
ARBITRARY UNITS
(a)
(b)
(c)
70
140
210
280
350
CHANNEL NUMBER

FIGURE 6.2

as well. Figures 6.3 - 6.9 shows the complete spectrum of the raw data of the M star, HR 5490, the hot star, α CrB and the divided 'clean' data from the wavelength interval λ 9748A to λ 10153A.

6.3 Atomic Line Identifications

The atomic line identifications are made with the aid of the table of Swensson (3) et al. (The solar spectrum from λ 7498A to λ 12016A), the Revised Multiplet table (RMT) by Moore (4) et al., and the table of Babcock and Moore (5). (The solar spectrum λ 6600A to λ 13495A). Finally, the identified lines were compared with data from published papers in the 1 micron spectral region of stars cooler than the sun (Sanford et al. (6), McKellar et al. (7), Miller et al. (8), Fredrick et al. (9), Griffin et al. (10), Wyller et al. (11) and Fay et al. (12)).

Comparison of the two tables of the solar spectrum above in the wavelength interval of λ 7498A to λ 12016A revealed that Swensson et al. lists twice as many lines than Babcock et al. This is mainly because in the infra red numerous lines produced by constituents of the earth's atmosphere masked significant parts of the real solar spectrum. However, since the solar spectrum of Swensson et al. was taken with a high resolution system and favourable observing conditions (i.e. at high altitude), particularly the low water vapour content of the atmosphere, the telluric absorption is markedly reduced, thus revealing many up to now unobserved solar lines that had not been found in solar spectrum taken by Babcock et al. at low dispersion. For

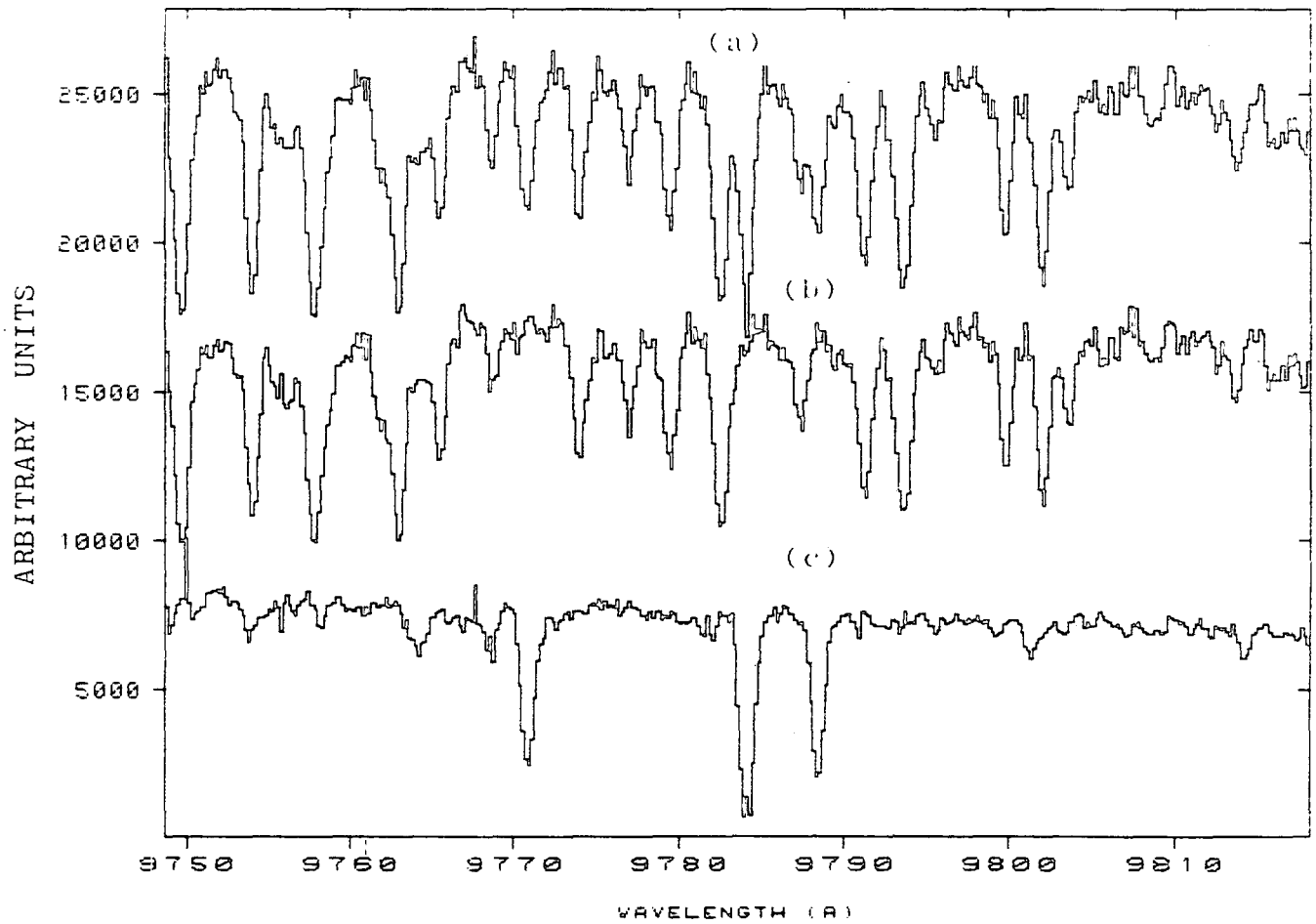
(a)
(b)
(c)
25000
20000
15000
10000
5000
ARBITRARY UNITS
9750
9760
9770
9780
9790
9800
9810
WAVELENGTH (A)

FIGURE 6.3

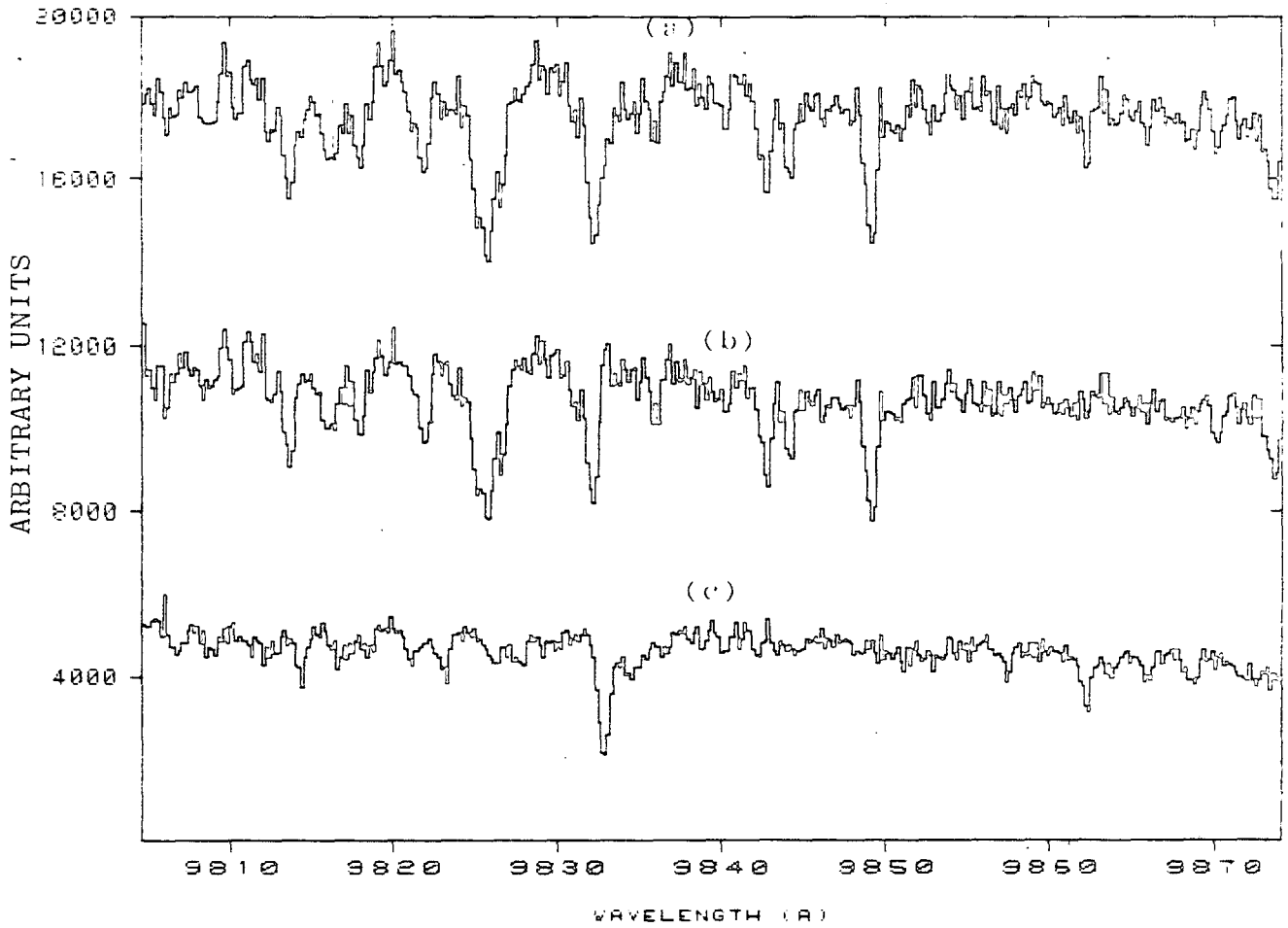
20000
16000
12000
8000
4000
ARBITRARY UNITS
(a)
(b)
(c)
9810
9820
9830
9840
9850
9860
9870
WAVELENGTH (A)

FIGURE 6.4

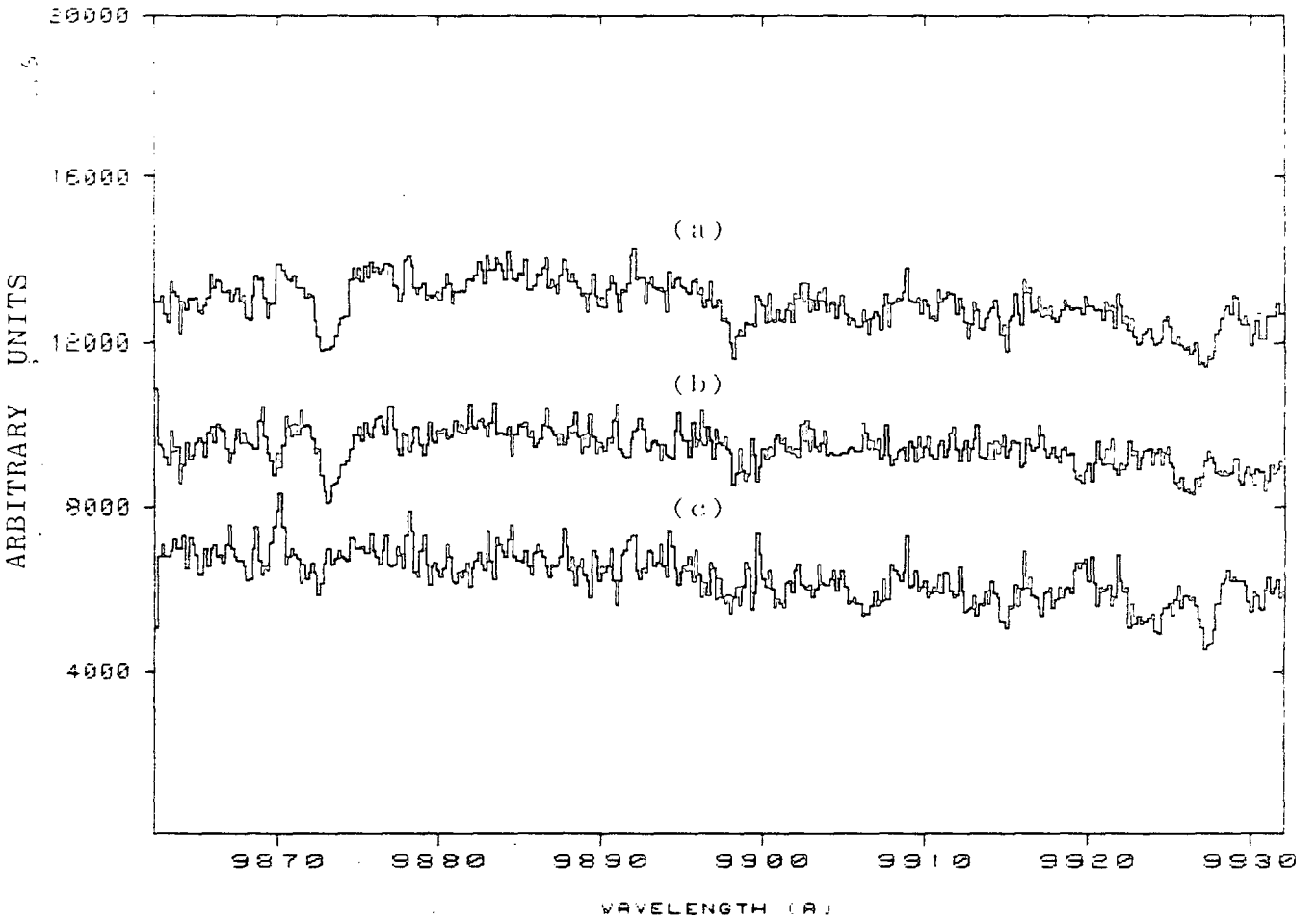
20000
16000
12000
8000
4000
ARBITRARY UNITS
(a)
(b)
(c)
9870
9880
9890
9900
9910
9920
9930
WAVELENGTH (A)

FIGURE 6.5

ARBITRARY UNITS
0.004
0.003
0.002
0.001
0.000
0550
0600
0650
0700
0750
0800
0850
0900
0950
WAVELENGTH (nm)
(c)
(b)
(a)

FIGURE 6.6

ARBITRARY UNITS
40000
30000
20000
10000
00000
WAVELENGTH (Å)
9750
9500
9250
9000
8750
8500
8250
8000
7750
7500
(c)
(b)
(a)

FIGURE 6.7

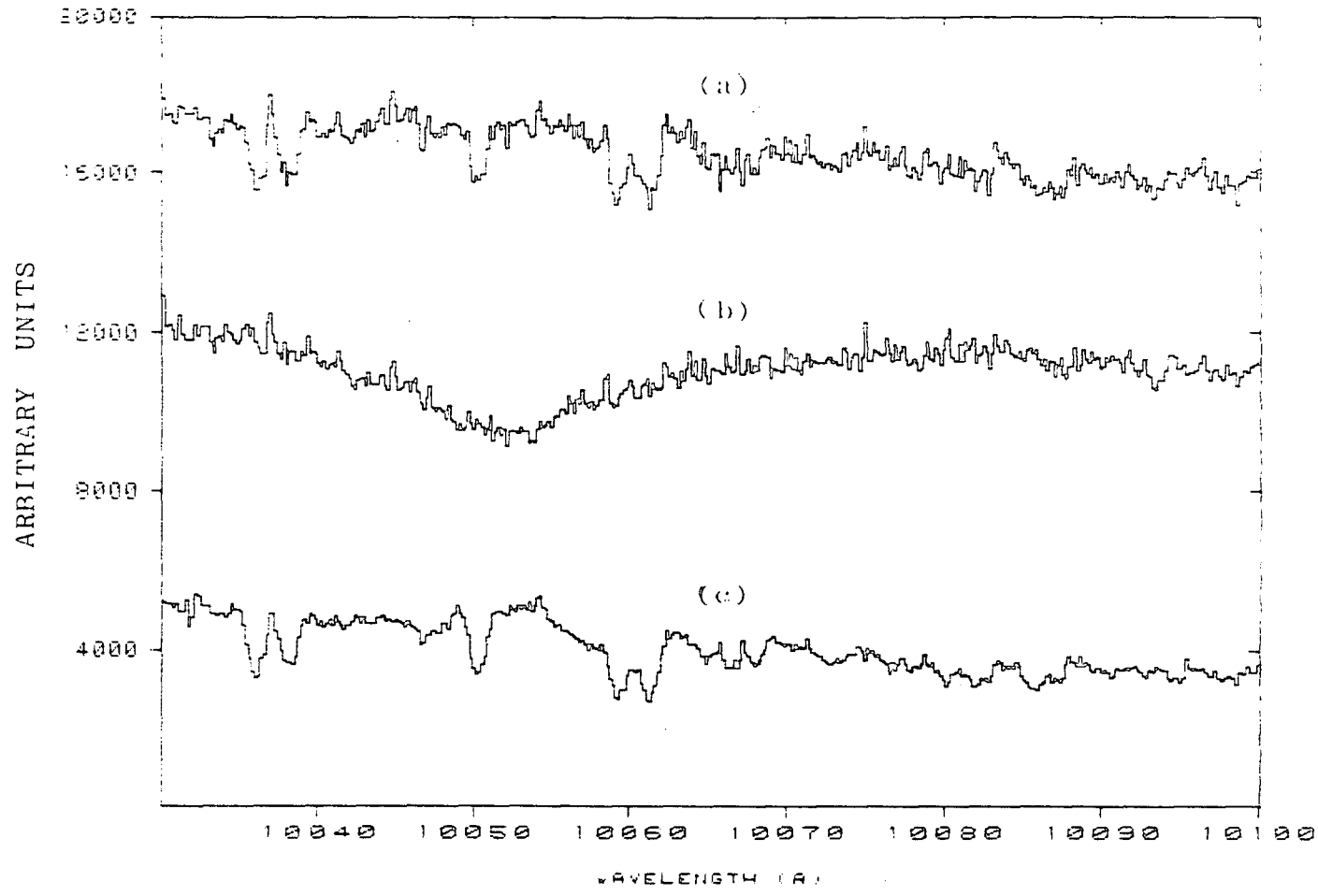
ARBITRARY UNITS
15000
9000
4000
(a)
(b)
(c)
10040
10050
10060
10070
10080
10090
10100
WAVELENGTH (A)

FIGURE 6.8

ARBITRARY UNITS
4000
8000
12000
16000
20000
(c)
(b)
(a)
WAVELENGTH (A)

FIGURE 6.9

this reason, our preliminary list of atomic line identifications was first compared for any given stellar wavelength ($\lambda_{observed}$) that coincides with the solar wavelength ($\lambda_{compared}$) of the table of Swensson's et al. which provides information on possible atomic, molecular, and terrestrial lines in the spectral region under study. However, the identifications were anchored on the clearly identifiable component of the TiI(32) multiplets which dominate the spectrum of the M star HR 5490.

The procedure of identification for the wavelength interval λ 9748A - λ 10153A was first to identify the components of the TiI (32) multiplet freed from O_2 blends at λ 9770.28A, of TiI (149) at λ 9927.35A, of TiI (193) at λ 10003.02 and FeI (264) at λ 10113.86. All the above mentioned lines showed well defined profiles in the spectrum of the M star, HR 5490 as illustrated in Figures 6.3 -6.9. These features provided the reference wavelength from which other identifications were made.

The continuum in the spectra of the M star, HR 5490 in the region λ 9748A - λ 10153A when plotted appears to the eye to be cut up by line absorptions mostly of atmospheric origin, (i.e. telluric lines) before dividing with the hot star αCrB. After the removal of most of the water vapour absorption lines from the M star spectrum, its continuum is now free of telluric line absorptions apart from the stellar line absorptions, thus making it easier to locate a continuum and detect faint diffuse lines. The procedure adopted for the establishment of the continuum level is by

eye estimation, selecting several continuum points throughout the region as representations of the true continuum.

Table 6.2 lists all of the resulting atomic line identifications together with their equivalent widths instead of intensities. Each of the seven columns of Table 6.2 may be summarised in the following paragraphs. Column I : $\lambda_{observed}$, Column 2 : λ_R and Column 4 : $\lambda_{compared}$.

Stellar lines observed in the spectrum of the M star, HR 5490 in the spectral region $\lambda 9748\text{Å} - \lambda 10153\text{Å}$ are listed in Column 1. The observed wavelength, $\lambda_{observed}$ of each line has not been corrected for radial velocity. Column 2 lists the stellar wavelengths corrected to zero radial velocity. The correction for radial velocity is made using the Doppler shift equation (13) given below.

$$\frac{\Delta\lambda}{\lambda} = \frac{V}{C} \qquad (6.3)$$

where $\Delta\lambda$ is the change in wavelength,

λ is the centered wavelength,

V is the radial velocity of the star, and

C is the speed of light.

Taking V = 6km/sec (value quoted in Hoffleit (14) for HR 5490) and C = 300,000 km/sec, equation (5.14) gives

$$\frac{\Delta\lambda}{\lambda} = 2 \times 10^{-5}, \text{ at } \lambda = 1\mu m, \Delta\lambda \approx 0{\cdot}2\text{Å} \qquad (6.4)$$

Therefore, the stellar lines are shifted about 20 micron i.e. approximately a pixel shift. Since the radial velocity of the star is positive, the star is receding from us and

TABLE 6.2

$\lambda_{OBSERVED}$ (Å)	λ_{R} (Å)	EQUIVALENT WIDTH mÅ	$\lambda_{COMPARED}$ (Å)	ORIGIN	TRANSITION	MULTIPLET NUMBER
9753.9	9753.7	90 (bp)	9753.82	H_2O	121 3_O-4_1	
9764.1	9763.9	140 (br)	9764.11	H_2O	121 5_3-6_2	
9770.8	9770.6	400 (br)	9770.32	TiI	$a^5F_4-2^5F_4^o$	32
9784.1	9783.9	580 (bv)	9783.56	TiI	$a^5F_u-2^5F_3^o$	32
9788.4	9788.2	420 (fb)	9787.72	TiI	$a^5F_u-2^5F_2^o$	32
9801.4	9801.2	110	9801.12	⊕		
9814.9	9814.7	90	9814.82	⊕		
9832.8	9832.6	210 (br)	9832.15	TiI	$a^3G_5-y^3F_u^o$	149
9868.0	9867.8	60	9867.20	H_2O	201 5_2-6_5	
9927.4	9927.2	170 (bv)	9927.38	TiI	$a^3G_4-y^3F_3^o$	149
9941.6	9941.4	120 (fb)	9941.33	TiI	$a^3D_2-x^3D_3^o$	193
9949.2	9949.0	130 (br)	9948.98	TiI	$a^3D_1-x^3D_2^o$	193
9961.7	9961.5	140 (bp)	9961.39	⊕		
9965.0	9964.8	90	9964.69	⊕		
9984.3	9984.1	100	9984.15	H_2O	041 $6_{-4}-5_{-3}$	
9998.5	9998.3	90 (br)	9998.04	TiI	$a^3G_3-y^3F_2^o$	149
10003.6	10003.4	140 (fb)	10003.12	TiI	$a^3D_2-x^3D_1^o$	193
10006.3	10006.1	80	10006.81	H_2O	041 $8_{-8}-7_{-7}$	
10012.2	10012.0	150 (fb)	10011.64	TiI	$a^3D_1-x^3D_1^o$	193
10032.5	10032.3	90	10032.24	⊕		
10034.7	10034.5	140 (br)	10034.55	TiI	$b^3F_u-2^3G_{5_2}^0$	95
10036.8	10036.6	170 (bv)	10036.65	SrII	$4d^2D_{3/2}-5p^2P_{3/2}$	2
10048.9	10048.7	180 (fb)	10048.77	TiI	$b^3F_3-2^3G_4^o$	95
10057.8	10057.6	90 (br)	10057.69	TiI	$a^3D_3-x^3D_3^o$	193
10060.0	10059.8	110 (bv)	10059.87	TiI	$b^3F_2-2^3G_3^o$	95
10066.9	10066.7	70 (bv)	10066.57	TiI	$a^3D_2-x^3D_1^o$	193
10105.5	10105.3	70	10105.77	⊕		
10113.9	10113.7	90 (bv)	10113.08	FeI	$a^3G_3-2^3F_2^o$	264
10129.9	10120.7	60 (fb)	10120.6	TiI	$a^3D_3-x^3D_2^o$	193
10145.6	10145.4	140 (bv)	10145.10	FeI	$y^3D_2^o-e^3F_3$	1247

PLEASE TURN OVER

hence the observed wavelength of each stellar line is shifted toward the red end of the spectrum. Each stellar wavelength is subtracted by 0.2A° for zero radial velocity. The wavelengths, $\lambda_{\text{compared}}$ listed in column 4 are obtained from the tables of solar spectra of Swensson et al. and also Babcock et al.

Column 3 : Equivalent width.

Column 3 contains the estimated equivalent widths generated by the SPICA reduction package. The residual error in the equivalent width estimate is about 10 milli-angstrom. The equivalent widths column contains various letters and symbols having the following meaning:

br - blend toward red side or shaded to longer wavelength,

bp - broad profile,

bv - blend toward violet side or shaded to shorter wavelength, and

fb - free from atmospheric lines blending.

Column 5 : Origin.

The classification of lines into those of stellar and those of terrestrial origin has been based on the works of Sanford et al., McKellar et al., Griffin et al., Wyller et al., and Fay et al., as well as the two tables of the solar spectrum. For lines of unknown chemical origin the symbol ⊕ has been used.

Column 6 : Transitions, and Column 7 : Multiplet number.

For the classified stellar lines column 6 gives the transitions producing the observed absorption features. The complete spectroscopic designations for the identified atomic lines are given as they appear in Moore's Revised Multiplet table. Similarly, the multiplet number in column 7 is derived from Moore's Revised Multiplet table.

6.4 Discussion of the Stellar Data

Table 6.2 gives the results of the identification of atomic lines and may be water molecules found in the spectrum of the M star, HR 5490, λ 9748A^{o} - λ 10153A^{o}. The spectral line identification is made by taking the central wavelength of the stellar line and comparing it with the list of atomic wavelength tables mentioned in the previous section. To date the only high resolution infra red spectrum available known to the author is the Solar Spectrum from λ 7498A^{o} to λ 12016A^{o} compiled by Swensson et al. Therefore, there still remains the task of examining all the lines coincident with stellar lines to determine the most likely identification. The lack of information about the infra red spectra of many common atoms and molecules obtained from laboratory work and theoretical studies makes our identification far from complete.

The results show that thirty absorption lines were observed between the wavelengths λ 9748A^{o} and λ 10153A^{o}, several of them blended in wide absorption features. Of these identifications 19 are components of known multiplets,

7 correspond to solar lines of unknown origin and 4 features are believed to be water molecules (Swensson et al. (1970). Only the most conspicuous features have been selected for identification and it is believed that no spurious features are listed in table 6.2.

The multiplet TiI (32) observed by McKellar et al., Griffin et al. and Wyller et al. is positively identified in the spectrum of the M star, HR5490. Those lines belonging to the multiplets of TiI (95) and (193) found by Sanford et al. are also present in the spectra. The multiplets of TiI (149) surmised by Wyller et al. are identified without difficulty in the spectrum. The multiplets FeI (264) and FeI (1247) discovered by Griffin et al. are also observed in our spectra. A strong Strontium line belonging to multiplet SrII (2) is observed with a clear, clean profile at λ 10036.6A. The 4 features, believed to be water molecules, have wavelengths which match quite well with the water molecule wavelengths identified in the solar spectrum by Swensson et al. The possibility of these water molecule features originating in the stellar atmosphere cannot be ignored because Spinrad and Vardya (1966) (15) have shown stellar water vapour abundances on several infrared spectrograms of non-variable M giants and Mira variables at λ 10000A.

Although very little work has been done on molecules in the 1-micron region of M stars, some information is available for a few of the molecules expected to be important.

From the work of Nassau et al. (16), Sharples et al. (17), and Wing et al. (18) on spectral classification of infrared stars (e.g. M stars), there may be a number of weak molecular bands of TiO molecules present in the wavelengths of interest. Later Lockwood et al. (19) discovered three TiO bands in this region from the spectra of Mira variable star. The three TiO bands identified by Lockwood are located at wavelengths λ9814A, λ9899A and λ9986A. We tried to observe these features in our spectra of the M star, HR 5490 but no indications of depression regions or bandheads have been identified in the spectra. The absence of TiO bands in our spectra can be said to be in agreement with the work of Lockwood who showed that the TiO bands begin to appear only after the M5 spectral class.

A remarkable feature of the 1 micron region spectrum of the M star, HR 5490 is the weakness of the Paschen line Pδ (λ 10049.38A) which does not appear on the spectra. This makes it unlikely for any metal having a similar excitation potential or higher than that of the Paschen line Pδ to appear in the spectrum. A stellar feature observed near λ10049.38A, with a 180 mA equivalent width, is more likely to be due to a line of TiI (95) with whose wavelength it agrees more closely than that of Pδ. The errors of equivalent widths in table 6.2 may be expected to be around 10-20 per cent or typically 20 mA. Our estimation of equivalent widths show reasonable agreement with some of those calculated by Griffin et al. with our values perhaps slightly higher. This may be due to unrecognised blending of the absorption features with atmospheric lines

and the instrumental broadening caused by the Coude spectrograph, particularly the entrance slit. The on-chip prebinning method may also cause some broadening.

The main differences between the 1 micron region spectra of the M star, HR 5490 and the sun are the great strength of the Titanium (TiI) lines in the M star, together with the expected paucity of spectral features owing to its low temperature and therefore lack of lines of high excitation as present in the sun. Comparisons of the spectrum of HR 5490 (M3) with that observed for α Her (M5) and α Boo (K2) by Wyller et al. and Griffin et al. respectively, in our wavelength interval of interest, show our results to be in good agreement, i.e. the spectra contain many common features in this region. The spectra of the three stars are dominated in the 1 micron region by TiI together with one strong multiplet of SrII. There are two iron lines FeI (264) and FeI (1247) present in our spectrum as well as in Griffin but Wyller only detected the FeI (1247). The Titanium and the Iron lines appear to be in general somewhat stronger in our spectrum than observed by Griffin.

6.5 Confirmation of Results

In November 1982, a spectral atlas of a M2 giant star (β Peg) was compiled in the same wavelength interval as before with the same CCD camera system at the 30 inch reflector telescope at the RGO. Because this M2 giant is much brighter than the M3 giant (HR 5490), a signal-to-noise ratio of 100 was easily achieved with an exposure length

of under half an hour. This work was carried out by King et al. (20). Comparisons of these spectra with the other spectra reveal that all the absorption features identified in the M3 giant star (HR 5490) are also present in the M2 giant star (β Peg) but with a slight shift in wavelength values. This difference is to be expected because of the difference in the radial velocities of these stars and also errors in the calibration of the arc source frames. Unfortunately the comparisons of equivalent widths of the absorption features in the two spectra cannot be made at present because there are still a few problems outstanding in the reduction of the data from β Peg. Table 6.3 shows the wavelengths of the identified absorption lines of the two M giant stars. From this work done on identifying the absorption features present in the spectra obtained from the M3 giant star, HR 5490, it may be said that, the resulting wavelength values correlate very closely with those given in the table of the solar spectrum published by Swensson et al. (1970).

TABLE 6.3

COMPARISON OF THE TWO M GIANT STARS SPECTRA

WAVELENGTH HR 5490 $\lambda_{OBSERVED}$ (Å)	WAVELENGTH β PEG $\lambda_{OBSERVED}$ (Å)	ORIGIN AND MULTIPLET NUMBER
9753.9	9754.2	H_2O
9764.1	9765.5	H_2O
9770.8	9771.6	TiI (32)
9784.1	9785.2	TiI (32)
9788.4	9789.1	TiI (32)
9801.4	9802.0	+
9814.9	9815.7	+
9832.8	9833.2	TiI (149)
9868.0	9868.9	H_2O
9927.4	9927.9	TiI (149)
9941.6	9942.4	TiI (193)
9949.2	9949.9	TiI (193)
9961.7	9962.5	+
9965.0	9965.8	+
9984.3	9984.9	H_2O
9998.5	9999.3	TiI (149)
10003.6	10004.2	TiI (193)
10006.3	10007.1	H_2O
10012.2	10012.9	TiI (193)
10032.5	10033.3	+
10034.7	10035.2	TiI (95)
10036.8	10037.2	SrII (2)
10048.9	10049.4	TiI (95)
10057.8	10058.4	TiI (193)
10060.0	10060.8	TiI (95)
10066.9	10067.5	TiI (193)
10105.5	10106.2	+
10113.9	10114.6	FeI (264)
10120.9	10121.8	TiI (193)
10145.6	10146.3	FeI(1247)

REFERENCES

1. Starlink User Guide (SUG) and Starlink User Notes (SUN), prepared by Science and Engineering Research Council, Rutherford Appleton Laboratory, Computing Division, at Chilton, U.K.

2. Born, M. (1957), Atomic Physics, 6th ed., Hafner, New York.

3. Swensson, J.W., Benedict, W.S., Delbouille, L., and Roland, G. (1970), "The Solar Spectrum From λ7498 to λ12016"., Memoire Societe Royale Science Liege.

4. Moore, C.E. (1945), A Multiplet Table of Astrophysical Interest (N.B.S. Note 17 [Washington, D.C. : National Bureau of Standard]).

5. Babcock, H.D., and Moore, C.E., (1947), "The Solar Spectrum, λ6600 to λ13495", Carnegie Institution of Washington, Washington.

6. Sanford, R.F. (1947), "The Spectrum of α Orionis Between λ10,000 and λ10,915", Publication of Astronomical Society of the Pacific, 59, 136-138.

7. McKellar, A. (1954), "Spectra of the Cool Carbon Stars in the λ9000 - λ11000 Wavelength Region", Publication of Astronomical Society of the Pacific, 66, 312-320.

8. Miller, F.D. (1954), "Wolf-Rayet and Other Spectra of Early Type in The 1μ Region", Astrophysical Journal, Volume 120, 265 - 270.

9. Fredrick, L.W. (1961), "Spectra at 1 Micron of Planetary Nebulae and Stars Obtained with a Mica-Window Image Tube", Lowell Observatory Bulletin No. 114, Vol. V, No. 9, 149 - 152.

10. Griffin, R.F. (1964), "The Spectrum of Arcturus in The Far Infrared", Monthly Notices of The Royal Astronomical Society, Vol. 128, No. 3, 187-193.

11. Wyller, A.A. (1964), "Medium Dispersion Spectra of Two Carbon Stars and One Oxygen Star in The 1 Micron Region", Memoire Societe Royale Science Liege, 5th Ser. 9, 479-496.

12. Fay, T.D., Fredrick, L.W., and Johnson, M.R. (1968), "Comparison of Selected Carbon Stars and M Stars at 1 Micron", Astrophysical Journal, Vol. 152, 151-167.

13. Campbell, W.W. (1913), Stellar Motions (New Havan: Yale University Press; London : Henry Frowde; Oxford : University Press).

14. Hoffleit, D. (1982), "The Bright Star Catalogue", 4th Ed. Yale University Observatory, New Haven Connecticut, U.S.A.

15. Spinrad, H., and Vardya, M.S. (1966), "Approximate Abundances of The Light Elements from The Molecular Spectra of M and S stars", Astrophyscal Journal, 146, 399-410.

16. Nassau, J.J. (1956), "Objective Prism Spectra of Relatively Cool Stars in the Near Infrared", Vistas Astronomy, Vol. 2, 1361-1368.

17. Sharples, S., (1956), "The Infrared Spectral Classification of M-type Stars", Astrophysical Journal, 124, 342-345.

18. Wing, R.F. (1979), "In Spectral Classifications of the future", IAU Colloquium No. 47, edited by M.F. McCarthy, A.G. Davis Philip, and G.V. Coyne (Vatican Observatory, Vatican City), P.347.

19. Lockwood, G.W. (1973), "Scanner Photometry of Weak TiO Bands Near 1 Micron in Cool M stars", Astrophysical Journal, 180, 845-855.

20. King, R., Ph.D. Thesis, University of Durham (in preparation).

CHAPTER 7

CONCLUSION

7. INTRODUCTION

The preceding chapters describe how the GEC CCD P8600, a 385 x 576 element area array has been successfully interfaced, via CAMAC, to an LS1 11/23 minicomputer, and also the basic operation of the necessary system software to provide exposure control, data acquisition and some simple analysis. Additionally, a rack of purpose built front-end electronics was required to generate timing signals and perform analog to digital conversion of the output signal from the array (1). The detector device itself was chosen because of its high quantum efficiency, good linearity, large dynamic range and potentially low readout noise which together with the obvious geometrical stability of solid state devices makes it a useful instrument for a number of astronomical projects.

The effectiveness of the total system, CCD detector and computer controlled acquisition system, was demonstrated by undertaking the compilation of a spectral atlas of a M3 giant star (HR 5490) in the Northern Hemisphere, using the 30 inch Coude telescope and spectrograph at the R.G.O. This spectral atlas, covering the wavelength range λ 9748Å - λ 10153Å, was then compared with results obtained for a M2 giant star (β Peg), in the same wavelength interval and obtained with the same equipment (2). This comparison reveals that all the absorption features identified in the

M3 giant star are also present in the M2 giant star but with a slight shift in wavelength values. This difference is to be expected because of the difference in the radial velocities of these stars and also errors in the calibration of the arc source frames. From this work it may be said that the CCD camera system offers a high degree of reproducibility and is capable of yielding astronomical data of high quality. However, the CCD still has a number of drawbacks, including the necessity to correct for non uniformity of response across the array, the high rate of detection of cosmic rays and the limited physical size of devices.

7.1 Design Considerations and Operation of area array of CCDs.

The GEC CCD type P8600, a 385 x 576 elements area image sensor is a front-face illuminated device. The possible disadvantages of the front-face illuminated detectors are that the sensitivity is reduced especially in the blue by absorption in the polysilicon and oxide layers; interference ripples may appear in the spectral response; and the modulation transfer function is degraded in the near infrared but less so in the blue. An alternative approach is to illuminate the device, through the substrate, from the back. In this case, however, to avoid a considerable loss in sensitivity the substrate must be made very thin otherwise most carriers would be generated too far away from the

depletion regions to be collected. The substrate must therefore be thinned down by some etching technique (3) to provide adequate sensitivity. For ideal blue response the substrate should be the same thickness as the depth of the depletion region so that all carriers are collected without relying on diffusion. Improvement of the blue response by this means will, however, result in loss of sensitivity of the chip toward the red and near infrared because of the restriction imposed on the substrate thickness.

For Frame transfer arrays the problem of dead areas does not exist, but the serial shifting of charge from image to readout sections with larger arrays could cause drive problems because of the high clocking rates necessary and degradation of image quality due to smear. In other words, this kind of array is not perfect and the various trade-offs need to be carefully considered for given applications. The usefulness of a charge coupled device for low light level detection (particularly faint object of 20th magnitude or more) depends very largely on the magnitude of the dark current non-uniformities which introduce fixed pattern noise. In practice this spatial noise is the major factor in determining the sensitivity and dynamic range of the CCD.

The on-chip pre-binning technique which may be implemented as the array is readout offers an improvement in signal-to-noise ratio with short exposure duration. Employing this technique may result in a loss of the spatial

resolution of the CCD camera system but because of the poor "seeing" condition at R.G.O., the spatial resolution is in practice usually less than the optimum obtainable with the array, since the entrance slit of the spectrograph has to be opened to let through a reasonable amount of light.

It is also possible that the readout noise figure of the existing device may be further reduced for certain applications with careful attention to the design of front-end electronics and adjustment of chip bias levels. In particular, the value of the capacitance of the final readout diode may be reduced thereby, in theory, lowering the "reset" noise, which is generally considered to be the limiting factor affecting device performance at very low signal levels. This would have the obvious disadvantage of reducing the maximum signal charge which the system could handle, but at low light levels this would not be an important consideration, however, further laboratory work is required to evaluate such fine tuning of CCD performance.

7.2 Future work

Further work on processing the data of the M3 giant star (HR 5490) need to be done particularly to correct for the instrumental effects present in data. When the instrumental effects have been removed, the equivalent widths of moderately strong absorption lines present in the spectra will be measured more accurately, depending upon the local complexity of the spectrum. Knowing the equivalent widths of these lines will help in deriving the stellar chemical abundances. Since the chemical abundances are

dependent on the luminosity and temperature of the stellar atmosphere, therefore the luminosity and temperature of the M3 giant star can also be determined (see reference 2).

High quantum efficiency in the far red and low read out noise make the silicon CCD an attractive panoramic detector for very faint, redshifted galaxies. In conjunction with a large, fast telescope it will be used to extend the distance to which galaxies may be studied.

The CCD camera system will be used with the faint object spectrograph (F.O.S.) when it is in commission at La Palma to explore its potential further. At present a software package for the Durham CCD camera system is being developed by G.P. Martin in order to run the CCD camera system interfacing to a Perkin Elmer machine which has its own software called "ADAM". The "ADAM" package is being prepared by the Royal Greenwich Observatory, and will provide facilities for control of the telescope operation, spectrograph, camera function and on-line data reduction and analysis work. All the above developments are part of a major (SERC) project to build a faint object spectrograph, F.O.S., which is currently nearing completion and involves workers at the R.G.O. in collaboration with Dr. J.M. Breare and his research group at Durham University.

REFERENCES

1. Waltham, N.R., Ph.D. Thesis, University of Durham, in preparation.

2. King, R., Ph.D. Thesis, University of Durham in preparation.

3. Shortes, S.R., Chan, W.W., Rhines, W.C., Barton, J.B., and Collins, D.R. (1974), "Characteristics of Thinned Backside - Illuminated Charge Coupled Device Imagers", Applied Physics Letter, 24, 565-567.